Department of Precision and Microsystems Engineering

NONLINEAR DAMPING IN GRAPHENE NANODRUM RESONATORS

J.A. Smid

Report no : 2019.006
Coach : Dr. F. Alijani
Professor : Prof. Dr. P.G. Steeneken
Specialisation : Dynamics of Micro- and Nanosystems
Type of report : Master of Science Thesis
Date : 15 February 2019

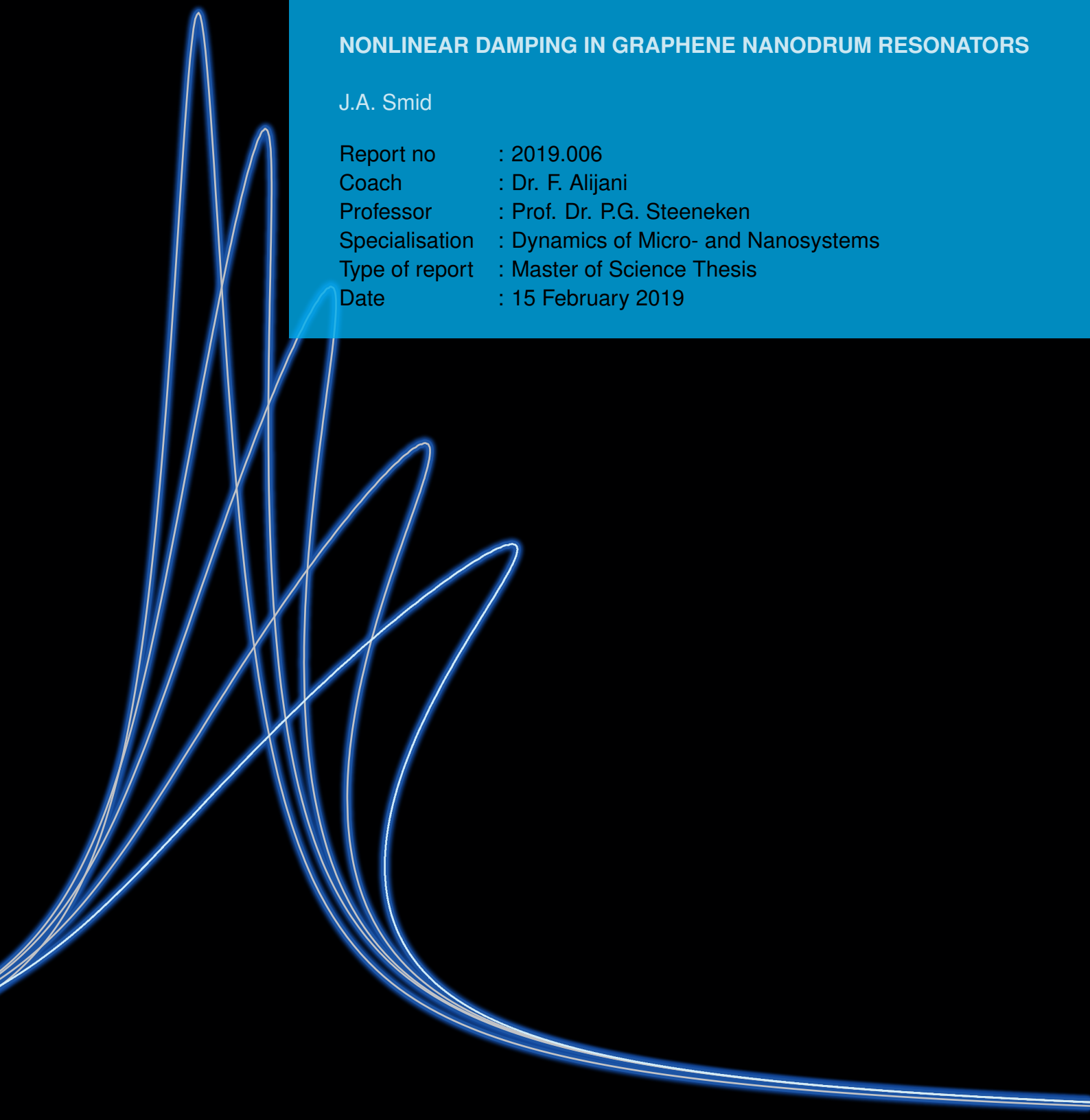

TU Delft Delft University of Technology

Challenge the future

Nonlinear damping in graphene nanodrum resonators

by

J.A. Smid

to obtain the degree of Master of Science
at the Delft University of Technology,
to be defended publicly on Friday February 15, 2019 at 01:00 PM.

Student number:	4001559	
Thesis committee:	Prof. dr. P.G. Steeneken,	TU Delft, chair
	Dr. F. Alijani,	TU Delft, supervisor
	Dr. ir. R.J. Dolleman,	TU Delft, supervisor
	Dr. ir. W.T. van Horssen,	TU Delft

Faculty of Mechanical, Maritime and Materials Engineering (3mE)
Delft University of Technology

Abstract

Nanomechanical resonators made from graphene are widely researched for their potential applications due to their high sensitivity. Their atomic scale thickness makes it that these resonators exhibit amplitude-dependent damping at relatively small driving forces. To further increase the performance of these devices, it is essential to understand the dissipation process. Although many physical mechanisms that lead to linear damping have been investigated, the origin of nonlinear damping remains largely unknown. Nonlinear damping in nanomechanical resonators is typically studied using phenomenological models. In this thesis, a multilayer graphene resonator is studied that is electrostatically actuated. The graphene resonator is modeled as a viscoelastic membrane operating in the geometrically nonlinear regime. The amplitude-dependent damping term used in phenomenological models arises naturally in the equation of motion. The experimentally obtained nonlinear frequency responses are then fitted using a fully automated algorithm. Based on these fits, the viscoelastic properties of graphene and its loss tangent are found. When the same analysis is done for a single-layer graphene resonator coupled to an optical cavity, negative nonlinear damping is observed which turns positive with increasing laser power. The effect of the optical field on the nonlinear damping is then modeled. It is found that the change in equilibrium position of the graphene membrane due to laser illumination as well as geometric imperfections can lie at the root of the negative nonlinear damping behavior.

Table of Contents

Acknowledgements

Before you lies the product of one-and-a-half years of work. During this time, many people supported me and without them it would have been substantially more difficult, if not impossible, to reach this milestone in my life. Therefore I would like to take this opportunity to thank them.

First of all, I want to thank my daily supervisor, Farbod, for his guidance during this process. His calm yet enthusiastic way of explaining makes him into a great teacher. Second, I would like to thank my co-supervisor, Robin, who always came with fresh suggestions for my project.

Then there are Richard, Gijs, Ad en Marc, with whom I spent a full year in the same office with, organising lunch lectures, excursions, and bitterballenborrels for all PME students. I could not have wished for better people on the Taylor board. My gratitude also goes to Koen, Ata, Savio and many other fellow students. Discussing my project with them always lead to new insights.

However, my biggest thanks goes to my parents. Their unconditional support has brought me all this way, and I am sure it will bring me even further still. They raised four children, and three of them have already obtained their Master's degree at Delft University of Technology. Hopefully, the fourth one will be added to it very soon.

Chapter 1

Introduction

Mechanical resonators are systems that show resonant behavior. Such systems have the natural tendency to vibrate at a certain specific frequency called the resonance frequency. When a resonator vibrates at its resonance frequency, the oscillations occur at a higher amplitude. Mechanical resonators are not only common at the macroscopic scale, but also at the micro and nano level. For example, nanomechanical resonators are used to measure single cells and nanoscopic particles [1, 2], or to detect gravitational waves [3]. However, miniaturizing a mechanical resonator typically leads to an increased energy loss, or dissipation, and thus to an increased dampening of the amplitude of vibration [4, 5]. This is often a problem, since the increased dissipation deteriorates the sensitivity and responsivity of the device. It is therefore important to study dissipation in nanomechanical resonators, in order to ultimately increase the performance of these devices.

1-1 Dissipation in nanomechanical resonators

1-1-1 Definition of dissipation

In general, the dynamic behavior of mechanical resonators can be characterized by two fundamental properties: the resonance frequency (f_0) and dissipation (energy loss). A certain degree of energy loss is always present in a mechanical system. Dissipation is commonly expressed as the inverse of the quality factor Q, or Q-factor:

$$Q^{-1} = \frac{\Delta W}{2\pi W_0} \tag{1-1}$$

The Q-factor expresses the ratio between the total mechanical energy W_0 that is stored in the system and the energy that is lost during one cycle of oscillation, ΔW. A high Q-factor corresponds to low dissipation and less damping of the vibrational amplitude of the resonator. There are various physical mechanisms that contribute to the overall energy loss. These can be roughly divided into two categories. Intrinsic dissipation refers to all energy

loss mechanisms that happen within the resonator material. An example is energy loss due to the motion of defects in the material. Extrinsic dissipation includes all mechanisms where energy is lost to the environment of the resonator, like clamping losses and liquid damping. The total dissipation is a summation of all these individual mechanisms:

$$Q^{-1} = Q^{-1}_{defects} + Q^{-1}_{clamping} + Q^{-1}_{liquid} + ... \tag{1-2}$$

The most dominant dissipation mechanism will thus dictate the total Q-factor of the system.

Before summing up the various physical mechanisms that describe small dissipative processes, the so-called standard linear solid model will be presented. This model provides a framework for dissipation that describes many of the intrinsic dissipation mechanisms.

1-1-2 The standard linear solid model

The various intrinsic dissipation mechanisms are most conveniently explained by using the Standard Linear Solid model (SLS), also known as the Zener model [6]. The SLS describes anelastic behavior of the material, which is a deviation from Hooke's law for ideal elastic materials. Like ideal elastic solids, anelastic solids have a linear stress-strain relationship and recover completely when an applied load is lifted. However, the response is not instantaneous, making the stress-strain relationship time dependent. Anelastic solids are a subset of linear viscoelastic materials, which do not recover completely. The SLS consists of purely elastic springs with Young's Modulus E_i and a viscous dashpot with viscosity η, and is capable of describing both stress relaxation and creep behavior in a simple manner. Figure 1-1 shows a representation of this model. The relationship between stress σ and strain ϵ can be derived easily, and is given by [7]

$$\sigma + \tau\dot{\sigma} = E_2\epsilon + \tau(E_1 + E_2)\dot{\epsilon} \tag{1-3}$$

where $\tau = \frac{\eta}{E_1}$ is the relaxation time at constant strain.

Now suppose a harmonic load is applied to this model. Since the response will not be instantaneous, the strain will lag behind the stress:

$$\epsilon = \epsilon_0 e^{i(\omega t)} \tag{1-4a}$$

$$\sigma = \sigma_0 e^{i(\omega t+\delta)} \tag{1-4b}$$

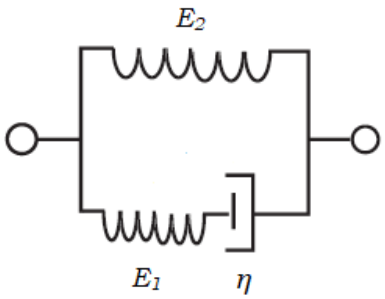

Figure 1-1: The Standard Linear Solid model, consisting of an elastic spring in parallel with a spring-dashpot combination.

Here, δ is called the loss angle. By filling in equation 1-4 into equation 1-3 and introducing a complex Young's Modulus $E^*(\omega)$, the stress-strain relationship can be rewritten to:

$$\sigma = \left(E'(\omega) + iE''(\omega)\right)\epsilon \tag{1-5}$$

with

$$E'(\omega) = E_2 + \frac{E_1\omega^2\tau^2}{1+\omega^2\tau^2} \tag{1-6a}$$

$$E''(\omega) = \frac{E_1\omega\tau}{1+\omega^2\tau^2} \tag{1-6b}$$

The storage modulus $E'(\omega)$ is the real part of $E^*(\omega)$, and this part of the stress-strain relationship is in phase with the strain. The loss modulus $E''(\omega)$ is the imaginary part of $E^*(\omega)$, and is $\pi/2$ out of phase with the strain. These quantities are used to calculate the amount of energy stored and lost in one loading cycle. The amount of energy lost and the maximum energy stored in the system are:

$$\Delta W = \oint \sigma d\epsilon = \int_0^{\frac{2\pi}{\omega}} \sigma \frac{d\epsilon}{dt} dt = \pi E''\epsilon_0^2 \tag{1-7a}$$

$$W_0 = \frac{1}{2}E'\epsilon_0^2 \tag{1-7b}$$

Therefore, using equation 1-1, the dissipation is simply:

$$Q^{-1} = \frac{E''}{E'} \tag{1-8}$$

Dissipation can also be related to the loss angle δ:

$$Q^{-1} = \tan\delta = \frac{(E_u - E_r)\omega\tau}{E_r + E_u\omega^2\tau^2} \tag{1-9}$$

where $E_u = E_1 + E_2$ is defined as the unrelaxed Young's Modulus and $E_r = E_2$ is the relaxed Young's Modulus. The loss angle δ is therefore a measure of energy loss per cycle, i.e. viscoelastic damping. For this reason, $\tan\delta$ is often referred to as the internal friction of the material.

The expressions for E', E'' and $\tan\delta$ are all frequency dependent. A plot of the complex Young's Modulus versus frequency is shown in figure 1-2. The shape of the loss tangent $\tan\delta$ is similar to that of E'', and is known as a Debye peak. Clearly, the dissipation has a maximum at $\omega\tau = 1$. From the plot, it also becomes clear what the SLS represents: it describes a single frequency-dependent dissipation mechanism with a relaxation time τ. When the resonance frequency of the resonator is close to τ^{-1}, dissipation will be large. In reality, a material will possess multiple relaxation times, and there will be multiple Debye peaks, possibly overlapping each other. However, when $\omega \ll \tau^{-1}$ or $\omega \gg \tau^{-1}$, dissipation will be small.

1-1-3 Intrinsic dissipation mechanisms

Defects

In reality, any material has a certain degree of defects or disorder. Crystal defects in the resonator can significantly influence the dissipation [8]. The defect-related dissipation mechanisms are due to atomic and defect motion, as they reconfigure between equilibrium and

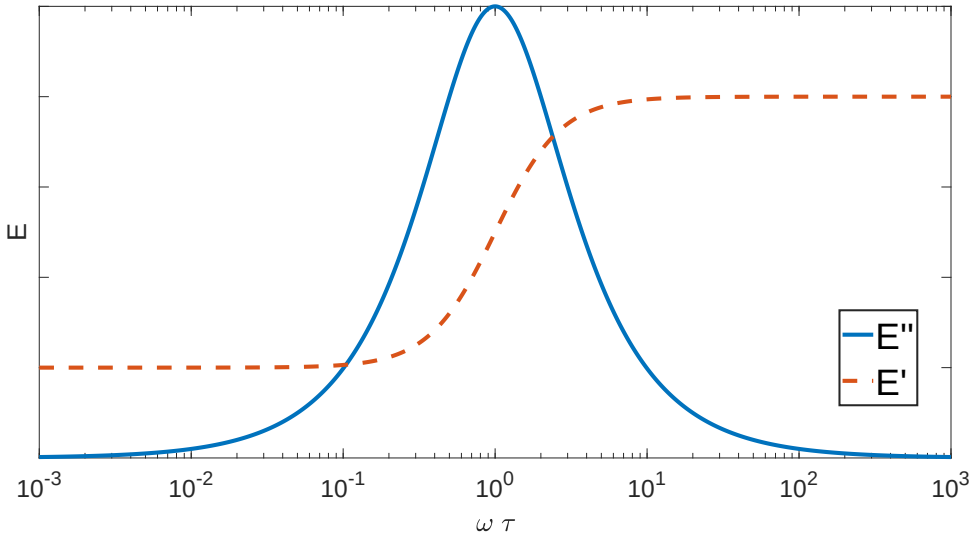

Figure 1-2: Plot of the storage modulus E' and the loss modulus E''. E' transitions from the relaxed modulus E_r to the unrelaxed modulus E_u with increasing $\omega\tau$. E'' has a maximum at $\omega\tau = 1$.

metastable states under application of a time-varying strain field. There can be numerous physical origins that cause reconfiguration, like the motion of vacancies, substitutinal impurities or dislocations. These processes take a finite amount of time relax to a new equilibrium value, a feature that is characteristic for anelastic solids and the SLS. A detailed overview of many processes is given in Ref. [9]. The dissipation due to defects takes the same form as equation 1-9:

$$Q^{-1} = A\frac{\omega\tau}{1+(\omega\tau)^2} \tag{1-10}$$

where A is a constant related to the concentration and nature of a specific defect. Most processes are thermally activated [10] and can be described by atomic motion, for which the relaxation rate (or: 'frequency jump') τ^{-1} follows the Arrhenius relation. These defects are characterized by an activation energy E_A that is required to overcome an energy barrier in order to switch to another stable state. Consequently, for a specific thermally activated defect, equation 1-10 can be rewritten to [11]:

$$Q^{-1} = A\frac{\omega\tau_0 \exp\left(\frac{E_A}{k_B}\left(\frac{1}{T}-\frac{1}{T_0}\right)\right)}{1+\left(\omega\tau_0 \exp\left(\frac{E_A}{k_B}\left(\frac{1}{T}-\frac{1}{T_0}\right)\right)\right)^2} \tag{1-11}$$

where τ_0 is the characteristic atomic vibration period, k_B is the Boltzmann constant, T is the temperature and T_0 a reference temperature. Dissipation due to thermally activated defect motion is therefore frequency as well as temperature dependent. By measuring peak temperatures at different frequencies, E_A can be extracted. Knowledge of E_A helps to identify a particular relaxation process.

Surface losses

As the dimensions of a resonator become smaller, the surface-to-volume ratio increases, and surface effects can start to dominate the dissipation. Due to the abrupt termination of the crystal lattice and surface contamination, the surface can contain defects as well. To model the losses related to these surface defects, a separate complex Young's Modulus $E^S = E'_S + iE''_S$ can be introduced that describe the material up to a certain surface layer depth δ_s. For microcantilevers with width w and thickness t, the surface dissipation is then given by [12]

$$Q^{-1} = \frac{2\delta_s(3w+t)}{wt}\frac{E''_S}{E'} \tag{1-12}$$

For very thin beam, dissipation should become proportional to t^{-1} if surface effects dominate. This behavior has indeed been observed in thin single-crystal silicon and silicon-nitride cantilevers [12,13], silicon-nitride membranes [14] and diamond cantilevers [15]. Surface treatments also highly influenced the Q-factor in these resonators, further confirming the importance of surface losses in thin nanomechanical resonators. A high surface roughness results in higher losses because of the increased surface area.

Thermoelastic damping

Thermoelastic damping (TED) is a dissipation mechanism that arises due to the interaction between acoustic and thermal phonons. Phonons are quanta of vibrational energy of a lattice of atoms. Specifically, thermal phonons are generated by the temperature of the lattice (random lattice vibrations), whereas acoustic phonons refer to the coherent movement of atoms from their equilibrium position. The thermal expansion coefficient α of a material captures the coupling between the acoustic and thermal phonons. TED occurs even in a perfect, defect-free crystal, setting a lower limit to dissipation.

Zener was the first to describe TED as a dominant source of dissipation for beam resonators under flexural vibration by using the anelastic framework [16, 17]. The vibrations induce a strain field, which in turn causes temperature difference across the beam. For $\alpha > 0$, the compressed side increases in temperature while the stretched side decreases. Consequently, an irreversible heat flow is generated, causing thermalization at a finite rate and losing mechanical energy to the thermal phonon bath. Once again, dissipation takes the form of a Debye peak:

$$Q^{-1} = \frac{ET\alpha^2}{\rho C_p}\frac{\omega\tau_{th}}{1+(\omega\tau_{th})^2} \tag{1-13}$$

where C_p is the specific heat capacity at constant pressure and $\tau_{th} = \frac{\rho C_p t^2}{\pi^2\kappa}$ is the thermal relaxation time, with κ as the thermal conductivity. Only little energy is lost if $\omega \ll \tau_{th}^{-1}$ (the system stays in thermal equilibrium) or $\omega \gg \tau_{th}^{-1}$ (the heat has no time to relax). TED can be significant for micro resonators as well [18, 19].

Many improvements or extensions to Zener's model have been made, the most notable one being an exact expression for TED in thin rectangular beams [20]. Other extensions include TED for circular micro-plates [21], and introducing 2-D heat conduction [22] and ballistic (non-diffusive) heat conduction [23, 24]. In general, TED can be the dominant mechanism only for relatively thick resonators.

Akhiezer damping

Like TED, Akhiezer damping [25–27] is a phonon-mediated loss that is present even in a perfect crystal. In thermal equilibrium, the vibrational modes of the crystal lattice are occupied by thermal phonons according to the Bose-Einstein distribution. Now consider a suddenly applied uniform strain field. Due to anharmonicity, the strain changes the elastic constant and thus the frequencies of the various modes. Crucially, frequencies change differently for each mode. The original phonon distribution is then disturbed, and scattering among the phonons redistributes the populations to a new equilibrium [9]. The frequency changes are accompanied by temperature changes. Thus, different modes will have different temperatures, which will relax to the mean temperature value at a finite rate. The generated intramode heat flow removes energy from the strain field. This behavior can be described as an anelastic relaxation process, and dissipation is given by [28]

$$Q^{-1} = \frac{CT\gamma_G^2}{\rho v^2} \frac{\omega\tau_{ph}}{1+(\omega\tau_{ph})^2} \tag{1-14}$$

where C is the heat capacity per unit volume, γ_G is the Grüneisen constant which relates the strain field to the frequency changes, and v is the sound velocity. Furthermore, the phonon relaxation time $\tau_{ph} = \frac{3\kappa}{Cv_D^2}$, where v_D is the mean Debye sound velocity. The value of τ_{ph} is generally a few picoseconds, making Akhiezer damping relevant only in the GHz regime or above [24]. Akhiezer damping has been investigated for NEMS in doubly clamped Euler-Bernoulli flexural nanobeams [23], in longitudinally loaded nickel nanowires using molecular dynamics simulations [24] and for single-crystal resonators [29].

Phonon-electron interactions

Phonons do not only interact with other phonons, but also with free electrons. For nanomechanical resonators made of metals or highly doped semi-conducting materials, this leads to an additional dissipation mechanism that is often overlooked. An incoming strain wave results in ion oscillations, and this in turn generates a varying electric (and magnetic) field, forcing the “electron gas” to move. Due to electrical resistivity, energy is dissipated by Joule heating of the material [30]. For thin film resonators made of piezoelectric material, it was found that phonon-electron interactions can be significant [31].

Two level systems

Two-level systems (TLSs) are used to give a quantum-mechanical description of the transition of an atom or defect from one state to another [32]. At sub-Kelvin temperatures, atoms and defects are only active in their quantum-mechanical ground state or nearly degenerate ground states. Even though the energy barrier between two possible states is too high for thermal activation of the defect, it can "tunnel" through this barrier. This is depicted in figure 1-3, where two states of a particle are described as an asymmetric double well potential. Because of energy conservation, a phonon must be either absorbed or emitted. At low temperatures, TLSs couple to acoustic phonons resonantly, absorbing phonons. At higher temperatures, the phonons modulate the asymmetry energy Δ: a strain field disturbs the thermal equilibrium

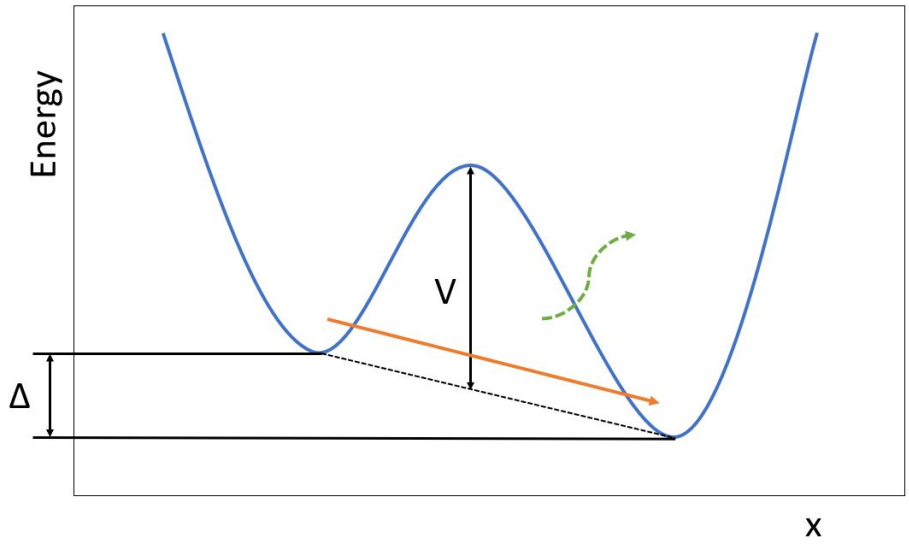

Figure 1-3: The asymmetric double-well potential of a two-level system. A particle can tunnel through the energy barrier V from one state to the other, indicated by the orange arrow. During this process, a phonon is either emitted (green dashed arrow) or absorbed, depending on the direction of the transition.

of the the TLSs, which then have to relax back to a new equilibrium at a finite relaxation rate [33]. This quantum-mechanical type of dissipation depends on temperature through a power law [34]. At very low temperatures, coupling to TLSs has to be included in any analysis.

1-1-4 Extrinsic dissipation mechanisms

Viscous damping

Some NEM resonators have to operate in fluidic environments. Fluid damping is often the most dominant loss mechanism in nanomechanical resonator. Depending on the fluid pressure and resonator dimensions, fluid flow and dissipation are treated in the viscous or the molecular regime. This is determined by the Knudsen number Kn, which is the ratio between the pressure-dependent mean free path of the fluid molecules and the characteristic length of the resonator. Liquids and gases with $\mathrm{Kn} < 0.01$ can be treated as a continuum, and the viscous flow results in a dissipative effect due to a drag force. Simple analytical models show that for resonating beams immersed in a viscous fluid, the Q-factor scales linearly with resonance frequency ω_0 [35]. Experiments on silicon nitride strings vibrating in air at atmospheric pressure confirmed this dependence, and showed that there is an optimal width for which the Q is maximized [36]. Furthermore, dissipation is shown to scale as $Q^{-1} \propto \sqrt{p}$ [37]. At sufficiently high pressure, dissipation can become pressure independent [38].

Considerable effort on studying viscous damping of fully immersed microcantilevers has been done as well. In a detailed derivation, it was shown that the Q-factor is a function of fluid viscosity and density, and increases monotonically with increasing Reynolds number (decreasing viscosity) [39]. The model was extended to include arbitrary flexural and torsional modes [40,41] and verified experimentally [42–44]. Suspended micro-channel resonators

(SMRs), which are used as mass and density sensors [1, 2], features fluid flow inside the resonator. Since they can be operated in vacuum, the Q-factor increases significantly with typical values of 10^3-10^4 [45]. The dissipation in this case comes from the boundary layers of the flow inside the resonators. A detailed study on the dissipation can be found in Refs. [46–48].

Gas damping: molecular regime

When the pressure is lowered, the free molecular path of gas molecules increases. At sufficiently low pressure and/or small dimensions of the resonator such that Kn > 0.5, energy dissipation follows from the momentum transfer between the individual gas molecules and the resonator [49]. During vibration, the number of collisions on one side is greater than on the other side. According to Boltzmann statistics, this then results in a net energy loss. Gas damping in the molecular regime can still be dominant, as was shown for cantilever microbeams where a Q-factor of just 18 was obtained [50]. For plates and beams in the molecular regime, $Q^{-1} \propto p$. When the pressure is reduced even further, dissipation become pressure independent since clamping losses and/or intrinsic losses start to dominate.

Squeeze-film damping

When the NEM resonator vibrates near another surface, like the substrate, the air between both surfaces has to be squeezed out of the created gap. The viscous flow of the air is responsible for a viscous damping force. Squeeze-film damping can be modeled for different geometries in both the viscous and molecular regime. For a long, oscillating beam, Q $\propto g^3$, where g is the gap distance [35]. Because of the strong dependence on gap distance, squeeze-film damping can quickly become a significant damping mechanism, especially for relatively wide beams. For the molecular regime holds Q $\propto g$ [5]. An excellent overview of squeeze-film damping for different geometries is given in Ref. [51].

Clamping losses

Vibrational energy of a nanomechanical resonator can radiate through the clamps into the support structure. At the point(s) where the resonator is clamped, varying shear forces and moments exist, which act as sources from which elastic energy is transmitted. The amount of energy dissipation is highly dependent on the design and geometry of the support. Clamping losses can be determined by using finite element analysis, but a few analytical models for specific geometries exist as well. These 2-D models are based on calculating a transmission coefficient which expresses how well the energy of a resonator mode is transmitted at the nodes into the supports. For thin cantilever beams attached to a thick base, the dissipation was found to be strongly dependent on both resonator thickness t and support thickness t_b [52]:

$$Q^{-1} \approx 0.95 \frac{w}{L} \frac{t^2}{t_b^2} \tag{1-15}$$

This analytic models have been verified experimentally [53].

1-1-5 Dissipation in graphene resonators

Due to its unique mechanical, electrical, thermal and optical properties, graphene has gained tremendous interest from the academic community for its potential applications. Graphene resonators are highly sensitive and can for instance be used as mass sensors [54], pressure sensors [55] or gas sensors [56]. Graphene resonators can be made from graphene sheets [57] or carbon nanotubes (CNTs) [58]. The Q-factors measured at room temperature are typically in the order of 10^1-10^2, and can become even lower due to squeeze-film damping [59]. Among the first to study dissipation in graphene resonators was Seoánez [60, 61], who considered electrically driven graphene sheets on a Si/SiO_2 substrate. It was found that energy dissipation is mainly due to phonon-electron interactions. When the oscillating graphene layer is charged, these charges experience a time-dependent Coulomb potential created by the charges in the doped Si backgate. Consequently, electron-hole pairs in the graphene layer are created and excited by absorbing the mechanical energy. Likewise, the charges in the Si gate experience a time-dependent Coulomb potential from the charges in the oscillating graphene layer, creating electron-hole pairs in the Si gate as well. The creation of electron-hole pairs implies ohmic losses. When a optical actuation is used, the effect is still present but less pronounced.

Other mechanisms that contribute in a lesser extent to the total dissipation were also investigated. Trapped charges in the Si-SiO_2 interface and the bulk of the SiO_2 create electron-hole pairs in the graphene layer as well, resulting in additional ohmic losses. Another mechanism is the Velcro effect, which is the repeated breaking and healing of the hydrogen bonds between the graphene and the SiO_2 substrate. This type of dissipation is expected to be negligible for small amplitude vibrations, since the energy of the bond is much larger than the stored energy available in a typical graphene resonator. Coupling of the resonator to TLSs provides another dissipation channel. Considering that the graphene shows a high degree of crystallinity, it can be assumed that TLSs only exist in the rest of the structure. Charge impurities in the substrate can switch between metastable trapping sites, and can interact electrostatically with the electrons in the graphene. At $5 < T < 300$, damping due to TLSs is relatively unimportant. However, the temperature dependence of the Q-factor in the sub-Kelvin regime can be explained by TLSs [62].

Clamping losses, which are independent of temperature, were found to dominate at lower temperatures. For fully clamped membranes, the elimination of edge effects is likely to be responsible for increase in Q-factor [63]. Thermoelastic damping is generally not important for resonators based on graphene and other 2-D materials. The small dimensions result in extremely short thermal relaxation times. In order to be significant, the resonance frequency has to be very large, usually in the order of 1 THz at room temperature.

Classical molecular dynamics have been used to study the temperature dependence of clamping losses and friction between multiple graphene layers [64]. The strength of the van der Waals bond between the graphene and the substrate has a major influence on the total dissipation. A reduced attachment strength increases the dissipation. In double-layer graphene resonators, one layer can slide relatively easily over the other because of the weak van der Waals bonds between both layers. This further increases the dissipation. Both effects are enhanced at higher temperatures.

1-2 Nonlinear dissipation

1-2-1 Nonlinear dynamics of mechanical resonators

Because of their small dimensions, nanomechanical resonators are easily driven into the nonlinear dynamic regime with just very small forces. The most evident nonlinear effect often encountered is a nonlinear restoring force, which enters the equation of motion of a mechanical resonator through the Duffing term αx^3:

$$m\frac{d^2x}{dt^2} + \Gamma\frac{dx}{dt} + kx + \alpha x^3 = F\cos(\omega t) \tag{1-16}$$

where m is the mass, Γ is the dissipation rate, k is the linear stiffness and $F\cos(\omega t)$ the harmonic force. Depending on the sign of α, the resonator becomes stiffer or softer, resulting in an amplitude dependent resonance frequency as shown in figure 1-4. All resonance frequencies at different driving forces form the back-bone curve. For sufficiently high force values, two saddle-node bifurcation points exist, making the amplitude a multivalued function of ω in certain ranges. Two periodic solutions are stable whilst one is unstable. This leads to the jump phenomena as the frequency is swept up- or downwards. The Duffing term can originate from nonlinear effects of external potentials or geometric effects [65], which are especially important for graphene resonators since the amplitude of vibration quickly exceeds the resonator thickness.

Another type of nonlinearity to be considered is nonlinear damping, which has been shown

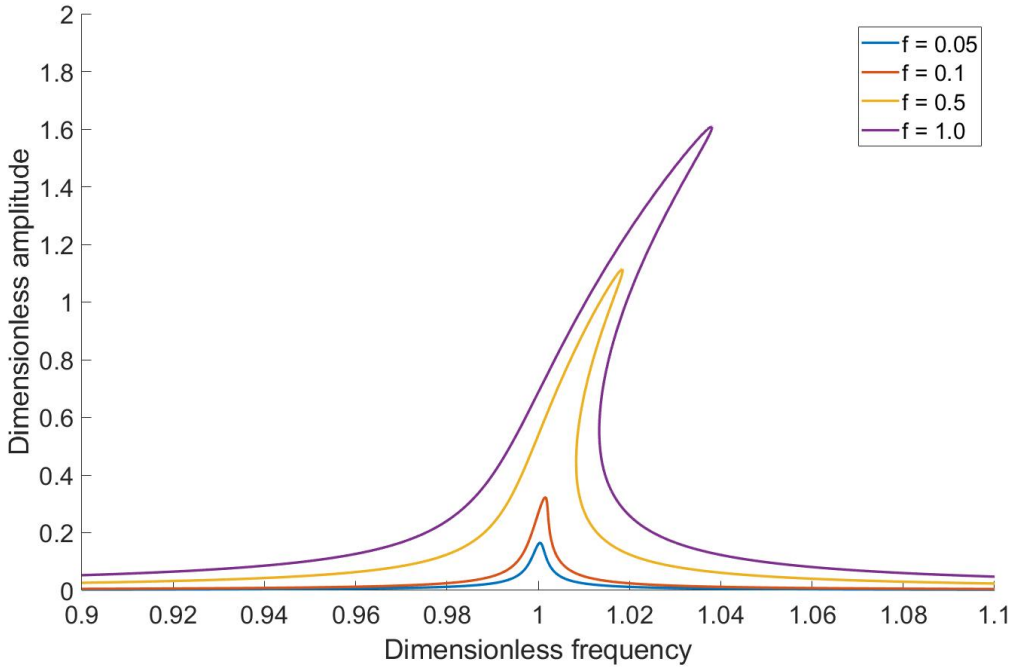

Figure 1-4: The frequency response of a mechanical oscillator with a nonlinear restoring force for different force levels f. Here, $\alpha > 0$, and the resonator becomes stiffer as the driving force is increased.

to be relevant for nanomechanical resonators [66]. The effects of nonlinear damping on the dynamic behavior can be demonstrated by adding an amplitude-dependent damping term $\nu x^2 \dot{x}$ to the equation:

$$m\frac{d^2x}{dt^2} + \Gamma\frac{dx}{dt} + kx + \alpha x^3 + \nu x^2\dot{x} = F\cos(\omega t) \tag{1-17}$$

Secular perturbation theory can be used to find an approximate solution to this equation. Following Lifshitz and Cross in Ref. [67], the amplitude is given by:

$$|a|^2 = \frac{g^2}{\left(2\Omega - \frac{3}{4}|a|^2\right)^2 + \left(1 + \frac{1}{4}\eta|a|^2\right)^2} \tag{1-18}$$

where a, λ, Ω and η are dimensionless expressions for the amplitude, force, frequency and the nonlinear damping coefficient respectively. The nonlinear damping coefficient is expressed as $\eta = \frac{\nu\omega_0}{\alpha}$. For $0 < \eta < \sqrt{3}$, the critical value of the force that is required for bi-stability increases with η, whereas for $\eta > \sqrt{3}$, bifurcation no longer occurs. Without nonlinear damping, bifurcation will always occur above a certain critical force value.

For high driving amplitudes, nonlinear damping will significantly reduce the magnitude of the response. The effective damping rate can be deduced from equation 1-18 and is given by $1 + \frac{1}{4}\eta|a|^2$. The effect of nonlinear damping on the frequency response curve is therefore the same as the effect of linear damping: it determines the position of the resonance peak. However, since the resonance peaks will always lie on the back-bone curve, it is hard to distinguish between linear and nonlinear damping. This problem can be dealt with by looking at the normalized response, i.e. the amplitude divided by the force. This is also called the responsivity of the resonator. When $\eta = 0$, the normalized response is constant for increasing driving force. For $\eta > 0$, responsivity decreases with increasing drive fore because of the additional damping. This behavior is shown in figure 1-5.

Finally, it is worth to investigate what happens to the analysis when other forms of nonlinear damping are chosen, like $\dot{x}^3$ or $x\dot{x}^2$. Interestingly, this does not alter the analysis in any fundamental way, and only leads to different effective expressions for the nonlinear damping. It is often unclear which expression to use, since the underlying physical mechanisms for nonlinear damping remain largely unknown.

1-2-2 Nonlinear damping at the nanoscale

Nonlinear damping can play an important role in micro- and nanomechanical resonators. This has for instance been shown for a micromechanical beam oscillator, where nonlinear damping was necessary to describe the dynamics of the beam, as well as the behavior of the system near the bifurcation points [66]. To explain the source of this nonlinearity, a linear viscoelastic material model (the Kelvin-Voigt model) operating within the geometrically nonlinear regime was proposed. However, this could not fully account for the nonlinear dissipation parameter obtained from the experiments, suggesting that other effects are at play. Nonlinear dissipation was also found in piezoresistive diamond nanomechanical resonators at cryogenic temperatures [68]. At room temperature, the Duffing equation (1-16) could fully explain the dynamic behvior. At temperatures of 77 K and below, linear dissipation

remained roughly the same, whereas nonlinear dissipation comes into play. Again, the source of nonlinear dissipation remains unclear, although coupling to two-level systems and nonlinear clamping losses are suggested. In addition to these findings, a "nonlinear dissipation back-bone curve" was proposed to characterize the strength of nonlinear dissipation. This back-bone curve can be created by starting from equation 1-18, setting $\Omega = 0$, and looking at the limit where the linear dissipation $Q^{-1} \to 0$. This is depicted in figure 1-6, and shows the dominance of nonlinear dissipation at high driving forces.

Resonators made from graphene sheets and carbon nanotubes also exhibit nonlinear damping [69]. The observed resonance broadening and the break-down of hysteresis in the nanotube

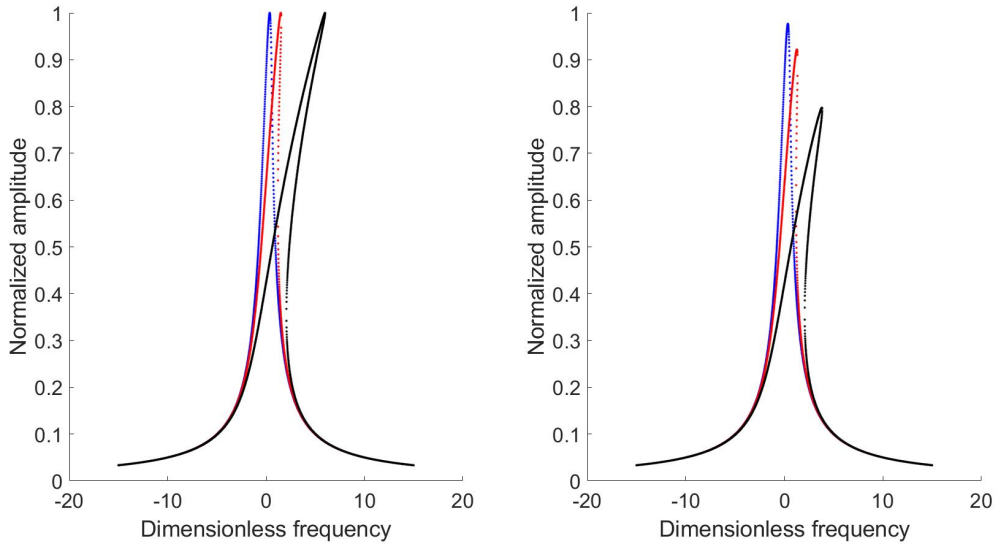

Figure 1-5: The responsivity of a nonlinear mechanical oscillator without (left) and with (right) nonlinear damping for different values of the driving force. Without nonlinear damping, the responsivity stays constant. With nonlinear damping, the responsivity decreases with increasing driving force.

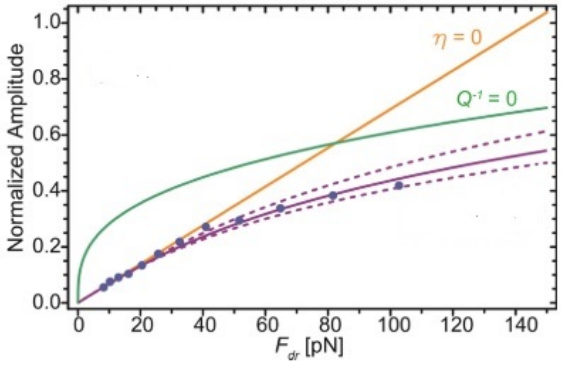

Figure 1-6: Dissipation back-bone curves for the limit where nonlinear dissipation is zero (yellow line), the linear dissipation is zero (green line), and a combination of linear and nonlinear dissipation, fitted to experimental data (purple line and dots respectively). F_{dr} is the driving force. Source: [68].

resonators is explained by adding an amplitude-dependent damping term to the equation of motion, similar to equation 1-18. The experiments were performed at a temperature of 90 mK. The physical origin is not investigated, but it is suggested that a linear dissipation mechanism, such as clamping losses, in combination with geometrical nonlinearity could be responsible, as well nonlinearities in the phonon-phonon interactions and the sliding between graphene and metal electrodes. Coupling between flexural vibrations and in-plane displacements has also been proposed as a microscopic mechanism for both linear and nonlinear damping in graphene resonators [70]. The cross-over between both regimes could be managed by varying the bias and ac voltages.

In a more recent effort, negative nonlinear damping was observed experimentally in a multilayer graphene resonator [71]. When driven at larger amplitudes, the resonator showed a reduction of the mechanical damping rate, with the total damping remaining positive. The extracted effective linear damping did not follow a quadratic dependence on the resonator amplitude, suggesting a nonlinear damping term in the form of $\nu|x|\dot{x}$, with $\nu < 0$. Furthermore, the negative nonlinear damping was believed to be intrinsic to the resonator, and not a result of optomechanical effects. As a possible source, saturation of TLSs coupled to the resonator was proposed. The TLSs absorb vibrational energy at low drive forces, resulting in an increased damping rate. When the drive is increased, the absorption is saturated, and the damping rate goes down. Negative nonlinear damping has also been reported in a nanomechanical plate resonator supported by two beams [72], where it was induced by nonlinear coupling of the resonator modes. The negative nonlinear damping could be made strong enough to overcome the positive linear damping in a certain range of vibration amplitude, leading to self-sustained oscillations.

1-3 Research objective

As discussed in the previous sections, nanomechanical resonators exhibit nonlinear damping. Because of their small dimensions, only very small forces on the order of nanoNewtons or even below are required drive the system into the nonlinear regime [65]. Nonlinear damping has then to be taken into account. Graphene resonators are especially prone to nonlinear damping, because of their atomic scale thickness. Although there are various mechanisms known that lead to linear dissipation, the origin of nonlinear dissipation is not well understood. Usually, nonlinear damping is introduced phenomenologically by simply adding an amplitude-dependent dissipation term to the Duffing equation, as shown in equation 1-17. However, most studies do not explain where this term comes from, or how it is obtained.

In this thesis, two possible sources for amplitude-dependent nonlinear damping in graphene resonators are explored. The first source is related to an intrinsic dissipation mechanism. From the previous sections, it became clear that dissipation can be understood in the viscoelastic framework. By introducing a viscoelastic material model, this source for dissipation is further investigated. The second source is related to an extrinsic dissipation mechanism. Many graphene resonator systems use optical techniques to detect the motion or for actuation. We show that the optical field leads to an optomechanically induced nonlinear damping.

1-4 Thesis outline

In this introductory chapter, various physical mechanisms for linear dissipation in nanomechanical resonators were investigated. Nonlinear damping was briefly introduced, and research objectives were formulated. In Chapter 2, nonlinear damping in a multilayer graphene nanodrum is investigated by modeling graphene as a viscoelastic material. This allows for the internal friction of graphene to be obtained, which is a measure of intrinsic damping. Chapter 3 is written in a paper format and deals with the influence of the optical field on the nonlinear parameters of the resonator. The paper is followed by a dedicated Supporting Information.

Chapter 2

Viscoelastic properties of multilayer graphene resonators

In this chapter, a viscoelastic material model is used to describe dissipation in an electrostatically actuated multilayer graphene resonator. The combination of this model and geometric nonlinearities results in an equation of motion with the same nonlinear damping term that is used to phenomenologically describe nonlinear dissipative behavior in nanomechanical resonators. Moreover, an automated fitting algorithm is developed from which the coefficients of the equation can be obtained. These coefficients can then be linked to the loss tangent. The following steps are followed in this chapter:

- The equation of motion of the graphene membrane is derived.
- This equation is used to fit the experimentally obtained frequency response curves.
- From the coefficients, the viscoelastic properties are determined.
- The loss tangent can then be calculated.

2-1 Modeling the graphene membrane

To model the graphene resonator, nonlinear membrane theory will be used. The equation of motion can be obtained with a Lagrangian approach, which allows for the coefficients of the equation to be related to viscoelastic properties. Eventually, a fit to experimental data obtained from the dynamic response of the resonator will then tell what the values of these properties are.

Consider a circular membrane element with radius a and thickness h, representing a graphene nanodrum, shown in figure 2-1. To conveniently describe the kinematics, the polar coordinates (r, θ, z) are used, where r is the radial coordinate, θ is the angular coordinate, and z is the transverse coordinate that goes through the thickness of the membrane. The membrane is

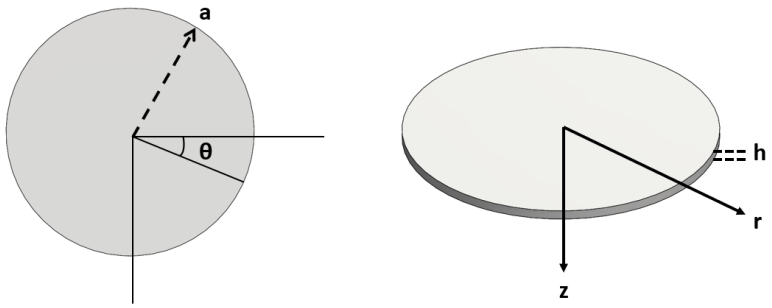

Figure 2-1: Membrane element representing the graphene nanodrum. The radial, tangential and transverse coordinates are indicted with r, θ and z respectively. The membrane has a radius a and thickness h.

fixed at the edges, such that the displacements are zero, but rotations are allowed. Throughout the analysis, only axisymmetric vibrations are assumed. After the kinematic and constitutive relations are established, the energies of the system will be calculated, resulting in the equation of motion.

2-1-1 Kinematic relation

The displacement vector $\mathbf{u}$, which denotes the displacement of a point on the membrane at a distance z from the middle surface, can be found by adopting Kirchhoff's hypotheses for circular plates [73]. It is therefore assumed that the lines orthogonal to the membrane's middle surface remain straight after bending. The components of $\mathbf{u}$ are then

$$u_1(r,\theta) = u(r,\theta) - z\frac{\partial w}{\partial r} \tag{2-1}$$

$$u_2(r,\theta) = v(r,\theta) - z\frac{\partial w}{r\partial \theta} \tag{2-2}$$

$$u_3(r,\theta) = w(r,\theta) \tag{2-3}$$

where u, v and w are the radial, tangential and transverse displacements of the middle surface respectively. To obtain the relation between strain and displacements, the Green-Lagrange strain tensor is used. Assuming a negligible bending rigidity of the membrane, it can be shown that the strain components ε_{rr}, $\varepsilon_{\theta\theta}$ and $\gamma_{r\theta}$ are given by

$$\varepsilon_{rr} = \frac{\partial u}{\partial r} + \frac{1}{2}\left(\frac{\partial w}{\partial r}\right)^2 \tag{2-4}$$

$$\varepsilon_{\theta\theta} = \frac{u}{r} + \frac{\partial v}{r\partial \theta} + \frac{1}{2}\left(\frac{\partial w}{r\partial \theta}\right)^2 \tag{2-5}$$

$$\gamma_{r\theta} = \frac{\partial u}{r\partial \theta} + \frac{\partial v}{\partial r} - \frac{v}{r} + \frac{\partial w}{\partial r}\frac{\partial w}{r\partial \theta} \tag{2-6}$$

Note that at this point, geometric nonlinearities have been introduced. However, only the nonlinear terms that depend on w are retained. This is the von Kármán hypothesis, which takes into account moderate rotations.

Since it is assumed that the membrane is subjected to axisymmetric vibrations only, $v = 0$ and $\partial/\partial\theta = 0$. Subsequently, the strains reduce to:

$$\varepsilon_{rr} = \frac{\partial u}{\partial r} + \frac{1}{2}\left(\frac{\partial w}{\partial r}\right)^2 \tag{2-7}$$

$$\varepsilon_{\theta\theta} = \frac{u}{r} \tag{2-8}$$

$$\gamma_{r\theta} = 0 \tag{2-9}$$

Furthermore, the edges of the membranes are fixed, so that $u|_{r=a} = 0$ and $w|_{r=a} = 0$. Moreover, continuity and symmetry dictate that $u|_{r=0} = 0$. The radial and tangential displacements that satisfy these boundary conditions are [74]:

$$w = \tilde{x}(t) J_0\left(\alpha_0 \frac{r}{a}\right) \tag{2-10}$$

$$u = u_0 r + r(a - r)\sum_{k=1}^{\bar{N}} q_k(t) r^{k-1} \tag{2-11}$$

where $\tilde{x}(t)$ is the generalized coordinate associated with the transverse motion of the fundamental axisymmetric mode, J_0 is the Bessel function of order zero, $\alpha = 2.40483$ and $q_k(t)$ are the generalized coordinates associated with radial motion. Furthermore, $\bar{N}$ is the number of terms used in the expansion of the radial displacement and u_0 is the initial displacement associated with the pre-tension n_0 of the membrane.

2-1-2 Constitutive relation: introducing viscoelasticity

To calculate the energies of the system, the relation between stress σ and strain ε has to be known as well. The simplest relation is known as Hooke's law:

$$\sigma = E\varepsilon \tag{2-12}$$

where E is the Young's Modulus. It assumes linear elastic material behavior and does not take into account any dissipative effects. In reality, materials deviate from this simple relation. Viscoelasticity describes such a deviation, and assumes that the material exhibits both viscous and elastic behavior when it is deformed. For viscous materials, stress depends on the rate of deformation rather than the strain itself. The stress-strain relationship of viscoelastic materials therefore depends on time, or, in the frequency domain, on frequency. It is due to this time dependence that three important effects in linear viscoelastic materials can be observed:

1. When a constant stress σ_0 is applied, the strain increases with time. This is called creep, and the creep response function is described as $J(t) = \frac{\varepsilon(t)}{\sigma_0}$.
2. When a constant strain ε_0 is applied, the stress decreases with time. This is called stress relaxation, and the relaxation response function is described as $E(t) = \frac{\sigma(t)}{\varepsilon_0}$.
3. When cyclic loading is applied, the stress and strain are out of phase. This hysteresis phenomenon leads to dissipation of mechanical energy. See also section 1-1-2.

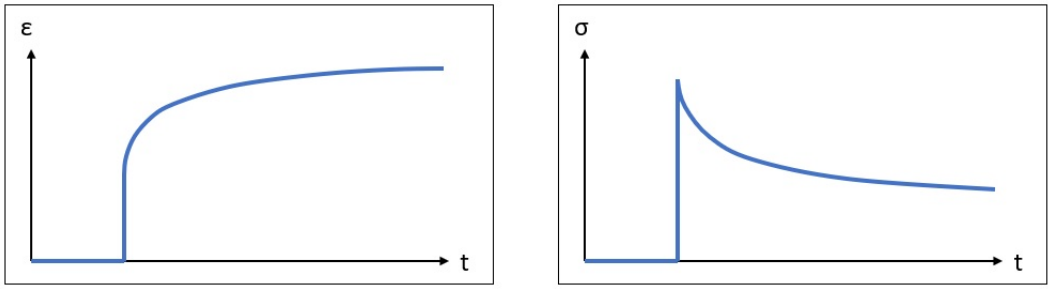

Figure 2-2: Response functions. Left: creep, which is the increase of strain with time after a step stress is applied. Right: stress relaxation, which is the decrease of stress with time after a step strain is applied.

The typical creep and relaxation responses are shown in figure 2-2. They are most easily approximated with exponential functions, which arise from mechanical models involving purely elastic springs ($\sigma_s = E\varepsilon_s$) and purely viscous dashpots ($\sigma_d = \eta\dot{\epsilon}_d$, where η is the viscosity). Two mechanical models will be further explored: the Kelvin-Voigt model, and the standard linear solid model, which has already been introduced in section 1-1-2.

Kelvin-Voigt

The Kelvin-Voigt model consists of a spring and a dashpot in parallel, as depicted in figure 2-3. The deformation in both elements is the same, and the total stress is the sum of the stresses in each element: $\sigma = \sigma_s + \sigma_d$. The relation between stress and strain when using this model can therefore be obtained easily and is given by:

$$\sigma = E\varepsilon + E\tau\dot{\varepsilon} \tag{2-13}$$

where $\tau \equiv \frac{\eta}{E}$ is a time constant called the retardation time or creep time. Applying a constant stress results in the following expression for the creep function:

$$J(t) = \frac{1}{E}\left(1 - e^{-t/\tau}\right) \tag{2-14}$$

Since the function is a decaying exponential, the creep behavior shown in figure 2-3 can be captured well. According to the Kelvin-Voigt model however, the stress relaxation function is a constant plus a delta function, which is clearly not correct.

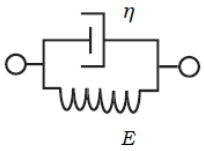

Figure 2-3: The Kelvin-Voigt model.

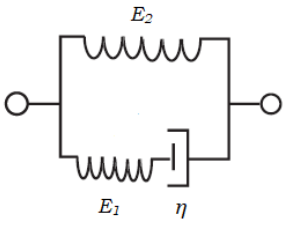

Figure 2-4: The SLS model.

Equation 2-13 can also be written in terms of the three polar coordinates (r, θ, z). Assuming that the material is homogeneous and isotropic, the constitutive relation becomes:

$$\begin{pmatrix} \sigma_{rr} \\ \sigma_{\theta\theta} \\ \tau_{r\theta} \end{pmatrix} = \frac{E}{1-\nu^2} \begin{bmatrix} 1 & \nu & 0 \\ \nu & 1 & 0 \\ 0 & 0 & \frac{1-\nu}{2} \end{bmatrix} \begin{pmatrix} \varepsilon_{rr} \\ \varepsilon_{\theta\theta} \\ \gamma_{r\theta} \end{pmatrix} + \frac{\tau E}{1-\nu^2} \begin{bmatrix} 1 & \nu & 0 \\ \nu & 1 & 0 \\ 0 & 0 & \frac{1-\nu}{2} \end{bmatrix} \begin{pmatrix} \dot{\varepsilon}_{rr} \\ \dot{\varepsilon}_{\theta\theta} \\ \dot{\gamma}_{r\theta} \end{pmatrix} \tag{2-15}$$

where ν is Poisson's ratio. Note that due to the axisymmetric vibrations considered here, $\gamma_{r\theta} = 0$. Therefore, $\tau_{r\theta} = 0$ as well.

Standard linear solid

The standard linear solid (SLS) model has already been introduced in section 1-1-2. This model, depicted again in figure 2-4, is an improvement on the Kelvin-Voigt model, since it gives exponential functions for both the creep and stress relaxation. Therefore, the standard linear solid is the simplest model to accurately describe linear viscoelastic behavior. The differential equation governing the stress-strain relationship is (see section 1-1-2):

$$\sigma + \tau\dot{\sigma} = E_2\varepsilon + \tau(E_1 + E_2)\dot{\varepsilon} \tag{2-16}$$

In this case, τ refers to the relaxation time. The fundamental difference between this differential equation and equation 2-13 is that first order derivatives appear for both σ and ε. Equation 2-16 may be solved for σ in terms of ε and $\dot{\varepsilon}$ by using the harmonic balance method [75]. The harmonic balance method allows to obtain an analytical approximation of the solution, by expressing it as a truncated Fourier series. Thus, in general, a solution $x(t)$ is expressed as

$$x(t) = x_0 + \sum_{m=1}^{M} x_{mc}\cos(m\omega t) + x_{ms}\sin(m\omega t) \tag{2-17}$$

where x_0, x_{mc} and x_{ms} are coefficients to be determined. In this particular case, the strain is expressed as a constant plus the first harmonic term

$$\varepsilon(t) = \varepsilon_0 + \varepsilon_1\sin(\omega t) \tag{2-18}$$

in which case the solution to equation 2-16 is expressed as

$$\sigma(t) = \sigma_0 + \sigma_{1c}\cos(\omega t) + \sigma_{1s}\sin(\omega t) \tag{2-19}$$

The coefficients ε_0, ε_1, σ_0, σ_{1c} and σ_{1s} are to be determined. They can be found by filling in equations 2-18 and 2-19 into equation 2-16 and equating the constant, cosine and sine terms respectively. Doing so gives:

$$\sigma_0 = E_2\varepsilon_0 \tag{2-20}$$

$$\sigma_{1c} + \tau\omega\sigma_{1s} = \tau\omega(E_1 + E_2)\varepsilon_1 \tag{2-21}$$

$$\sigma_{1s} - \tau\omega\sigma_{1c} = E_2\varepsilon_1 \tag{2-22}$$

The coefficients of the first order terms, σ_{1c} and σ_{1s}, can be rewritten as:

$$\sigma_{1c} = \frac{\tau\omega}{1+\tau^2\omega^2}E_1\varepsilon_1 \tag{2-23}$$

$$\sigma_{1s} = E_2\varepsilon_1 + \frac{\tau^2\omega^2}{1+\tau^2\omega^2}E_1\varepsilon_1 \tag{2-24}$$

Further combining and rewriting of the above equations leads to an expression for the stress of which one part is in phase with the strain, and another part that is out of phase with the strain. The first part is obtained by combining equations 2-20 and 2-24:

$$\sigma_0 + \sigma_{1s}\sin(\omega t) = E_2\varepsilon + \frac{\tau^2\omega^2}{1+\tau^2\omega^2}E_1(\varepsilon - \varepsilon_0) \tag{2-25}$$

Since this equation represents the in-phase part, it can be considered the elastic contribution to the stress-strain relationship of a material under harmonic loading. The second part is obtained by combining equations 2-20 and 2-23:

$$\sigma_{1c}\cos(\omega t) = \frac{\tau}{1+\tau^2\omega^2}E_1\dot{\varepsilon} \tag{2-26}$$

This part of the stress-strain relationship is the viscoelastic contribution, and depends on the strain rate rather than the strain itself. It is therefore $\frac{\pi}{2}$ out of phase with the strain, and will lead to damping of the system under consideration.

As was done for the Kelvin-Voigt element, the stress-strain relationship of the standard linear solid can be written in polar coordinates (r, θ, z). Assuming again a state of plane stress and that the material is isotropic and homogeneous, this leads to:

$$\sigma_{r,E} = \frac{E_2}{1-\nu^2}\left(\varepsilon_{rr} + \nu\varepsilon_{\theta\theta}\right) + \frac{\tau^2\omega^2}{1+\tau^2\omega^2}\frac{E_1}{1-\nu^2}\left(\varepsilon_{rr} + \nu\varepsilon_{\theta\theta}\right) \tag{2-27}$$

$$\sigma_{\theta,E} = \frac{E_2}{1-\nu^2}\left(\nu\varepsilon_{rr} + \varepsilon_{\theta\theta}\right) + \frac{\tau^2\omega^2}{1+\tau^2\omega^2}\frac{E_1}{1-\nu^2}\left(\nu\varepsilon_{rr} + \varepsilon_{\theta\theta}\right) \tag{2-28}$$

where $\sigma_{r,E}$ and $\sigma_{\theta,E}$ are the elastic contributions for the radial and tangential directions respectively. Note that the terms for initial tension have been left out. Similarly, the viscous contributions (denoted by the subscript $_V$) for both directions are:

$$\sigma_{r,V} = \frac{\tau}{1+\tau^2\omega^2}\frac{E_1}{1-\nu^2}\left(\dot{\varepsilon}_{rr} + \nu\dot{\varepsilon}_{\theta\theta}\right) \tag{2-29}$$

$$\sigma_{\theta,V} = \frac{\tau}{1+\tau^2\omega^2}\frac{E_1}{1-\nu^2}\left(\nu\dot{\varepsilon}_{rr} + \dot{\varepsilon}_{\theta\theta}\right) \tag{2-30}$$

2-1-3 Equation of motion

The equation of motion of the membrane is derived with a Lagrangian approach. In this approach, a function called the Lagrangian is formulated which depends on generalized coordinates $\mathbf{q}$, their time derivatives $\dot{\mathbf{q}}$ and time t. It contains information about the trajectory of the system of particles that forms the dynamic system under consideration. The Lagrangian is defined as:

$$L(\mathbf{q}, \dot{\mathbf{q}}, t) = T(\mathbf{q}, \dot{\mathbf{q}}, t) - U(\mathbf{q}, t) \tag{2-31}$$

where T is the kinetic energy, and U is the potential energy of the system. The Lagrange equation of motion can now be obtained with:

$$\frac{d}{dt}\left(\frac{\partial T}{\partial \dot{\mathbf{q}}}\right) - \frac{\partial T}{\partial \mathbf{q}} + \frac{\partial U}{\partial \mathbf{q}} = \frac{\partial W}{\partial \mathbf{q}} \tag{2-32}$$

where W is the virtual work done on the membrane by externally applied loads.

This Lagrangian approach has been used before to account for the viscoelastic behavior of square plates under large amplitude vibrations [76, 77]. It can also be applied to the circular graphene membrane. Using Kirchhoff's hypotheses, the potential energy of the membrane is [73]

$$U = \frac{1}{2}\int_0^a \int_0^{2\pi} \int_{-h/2}^{h/2} \left(\sigma_{rr}\varepsilon_{rr} + \sigma_{\theta\theta}\varepsilon_{\theta\theta} + \tau_{r\theta}\gamma_{r\theta}\right)\, r dr\, d\theta\, dz \tag{2-33}$$

Only axisymmetric vibrations are assumed, which means that the contribution of the term $\tau_{r\theta}\gamma_{r\theta}$ to the potential energy is zero. Since the constitutive relations for both the Kelvin-Voigt model and the standard linear solid are written as a function of ε and $\dot{\varepsilon}$, the potential energy of the membrane can be written as a summation of elastic (U_E) and viscous (U_V) parts. Using equations 2-15 and 2-33 and the fact that the displacement fields u and w are functions only of spatial coordinate r and time t, the following expression is obtained for the Kelvin-Voigt model:

$$U = U_E + U_V \tag{2-34}$$

with

$$U_E = \pi h \frac{E}{1-\nu^2}\int_0^a \left(\varepsilon_{rr}^2 + \varepsilon_{\theta\theta}^2 + 2\nu\varepsilon_{rr}\varepsilon_{\theta\theta}\right)\, r dr \tag{2-35}$$

$$U_V = \pi h \frac{\tau E}{1-\nu^2}\int_0^a \left(\varepsilon_{rr}\dot{\varepsilon}_{rr} + \varepsilon_{\theta\theta}\dot{\varepsilon}_{\theta\theta} + \nu\varepsilon_{rr}\dot{\varepsilon}_{\theta\theta} + \nu\varepsilon_{\theta\theta}\dot{\varepsilon}_{rr}\right)\, r dr \tag{2-36}$$

Next, the kinetic energy T of the membrane is obtained. The membrane is driven in its fundamental mode. It is therefore reasonable to assume that the in-plane inertia is much smaller than the out-of-plane inertia. This assumption then leads to the following expression:

$$T = \frac{1}{2}\rho\int_0^a \int_0^{2\pi} \int_{-h/2}^{h/2} \dot{w}^2\, r dr\, d\theta\, dz \tag{2-37}$$

$$= \pi\rho h \int_0^a \dot{w}^2\, r dr \tag{2-38}$$

where ρ is the mass density of the membrane.

Finally, in the presence of any externally applied load or pressure, the work done on the membrane by this load or pressure will appear as a generalized force on the right side of equation 2-32. In the case of a distributed harmonic pressure $p = \frac{F}{\pi a^2}\cos(\omega t)$ in the z-direction of the membrane, the virtual work done on the membrane is

$$W = 2\pi \int_0^a pw\, r dr \tag{2-39}$$

$$= \frac{2F}{a^2}\cos(\omega t)\int_0^a w\, r dr \tag{2-40}$$

where F is the amplitude of the force and ω is the frequency of excitation.

Equations 2-34 to 2-36, 2-38 and 2-40 can now be filled in into equation 2-32. Since the vector $\mathbf{q}$ contains the generalized coordinates $x(t)$ (associated with the transverse motion of the fundamental mode of the membrane) and $q_k(t)$ (associated with the radial motion), the result will be a system of one differential equation and $\bar{N}$ algebraic equations. The differential equation is related to $x(t)$, whereas the algebraic equations are related to $q_k(t)$. The algebraic

equations can be solved for $q_k(t)$ in terms of $x(t)$ by realizing that the total energy of the membrane for a position of equilibrium is minimum [74]:

$$\frac{\partial U_E}{\partial q_k} = 0 \qquad \text{for } k = 1, \ldots, \bar{N} \tag{2-41}$$

Consequently, a single nonlinear differential equation remains which is the equation of motion of the membrane:

$$m_{\text{eff}}\ddot{\tilde{x}} + c_1\dot{\tilde{x}} + k_1\tilde{x} + k_3\tilde{x}^3 + c_3\tilde{x}^2\dot{\tilde{x}} = \xi F\cos(\omega t) \tag{2-42}$$

where m_{eff} is the effective mass of the membrane, ξ is a correction factor that accounts for the fundamental mode shape, k_1 and k_3 are the linear and cubic stiffness coefficients respectively, and c_1 and c_3 are the linear (viscous) and nonlinear damping terms respectively. Equation 2-42 represents a forced Duffing oscillator, with a nonlinear damping term added to it. The nonlinear damping term is a consequence of the viscoelastic material model operating in a geometrically nonlinear regime. This equation is obtained for both the Kelvin-Voigt and the standard linear solid model. Each of the coefficients k_1, k_3, c_1 and c_3 are linked to certain material properties. The expressions for each of the coefficients depends on the material model used and the number of terms $\bar{N}$ in the radial displacement that are included. It is found that the values of the coefficients converge for $\bar{N} \geq 4$. Table 2-1 shows the results for both material models. A Poisson's ratio of $\nu = 0.16$ was used to obtain these results.

The equation of motion will be used to fit the experimentally obtained amplitude-frequency response of a graphene drumhead resonator. The parameters that are found through fitting can then be related to the viscoelastic properties. For the Kelvin-Voigt model, they can be related to the Young's Modulus E and the creep time τ. For the standard linear solid, they can be related to the dynamic modulus E^* and relaxation time τ.

Table 2-1: Expressions for the coefficients shown in equation 2-42 when the Kelvin-Voigt and the standard linear solid (SLS) models are used for the constitutive relation. The coefficients are functions of material and structural properties of the membrane. A Poisson's ratio of $\nu = 0.16$ was used to obtain these results.

Expressions of the coefficients in eq. 2-42.		
Coefficient	Kelvin-Voigt	SLS
m_{eff}	$0.847\rho h a^2$	$0.847\rho h a^2$
c_1	$2.448 n_0 \tau$	$2.448 n_0 \frac{E_1}{E_2} \frac{\tau}{1+\tau^2\omega^2}$
k_1	$4.897 n_0$	$4.897 n_0 + 2.448 n_0 \frac{E_1}{E_2} \frac{\tau^2\omega^2}{1+\tau^2\omega^2}$
k_3	$2.840 Eh/a^2$	$2.840 E_2 h/a^2 + 2.840 E_1 h/a^2 \frac{\tau^2\omega^2}{1+\tau^2\omega^2}$
c_3	$4.260 Eh\tau/a^2$	$4.260 E_1 h/a^2 \frac{\tau}{1+\tau^2\omega^2}$
ξ	0.432	0.432

2-2 Measuring the motion of the graphene membrane

2-2-1 Measurement setup

Graphene nanodrums were fabricated from an oxidized silicon wafer using lithographic and metal deposition techniques. The SiO_2 layer on top of the silicon layer is 285 nm thick. Circular holes were etched into the SiO_2. A gold-palladium layer with a thickness of 100 nm was used as a mask, and also serves as an electrical contact for actuation of the graphene membrane. Flakes of graphene were then transferred onto the sample with a dry transfer technique. See figure 2-5 for a schematic overview. The samples were then placed in a vacuum chamber at 2×10^{-6} mbar to significantly reduce the effects of air damping. Experiments were performed at room temperature. The readout of the motion is done with an interferometric setup [78]. The reflected intensity is directed with a beamsplitter (BS) to a photodiode (PD), which converts the signal to an electric current. A Vector Network Analyzer (VNA) measures this current. Its output is an AC-voltage which, together with a superimposed DC-voltage, is used to actuate the membrane. A schematic drawing of the setup is shown in figure 2-6. The applied electrostatic driving force is determined accurately: calculations were based on the geometry and applied voltage, and on the measured amplitudes at resonance [65]. This accounts for uncertainties in gap size, the DC-voltage experienced by the drum and the device capacitance. Finally, using a calibration procedure based on the thermal motion of the membrane, the measured VNA signal is converted to a root-mean-squared motion amplitude.

The graphene membrane presented here in the main text is 8 nm thick (approximately 24 layers), and has a radius of $a = 2\,\mu$m.

2-2-2 Experimental results

Measurements of the membrane's motion were all done using upward frequency sweeps near the fundamental resonance frequency, which allows one to obtain the frequency response data. The frequency sweeps were performed at different driving forces. At low driving forces the

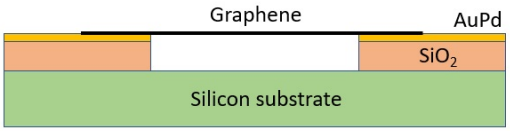

Figure 2-5: Schematic drawing of the sample.

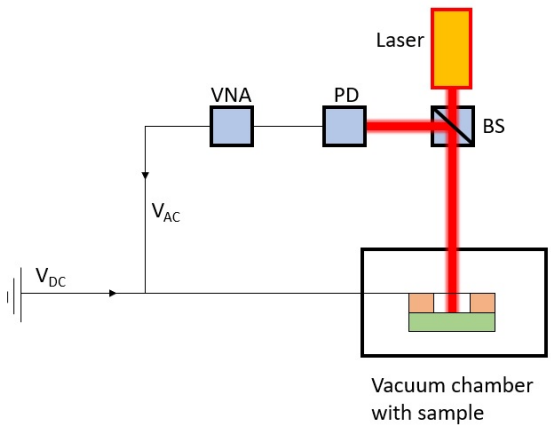

Figure 2-6: Schematic drawing of the measurement setup.

frequency response is linear, while at sufficiently high driving forces, the response becomes nonlinear. This nonlinear response is mainly characterized by a stiffening effect: the resonance frequency becomes a function of amplitude. The frequency response for all driving forces is shown in figure 2-7.

The responsivity of the graphene membrane can also be plotted, since the driving forces are

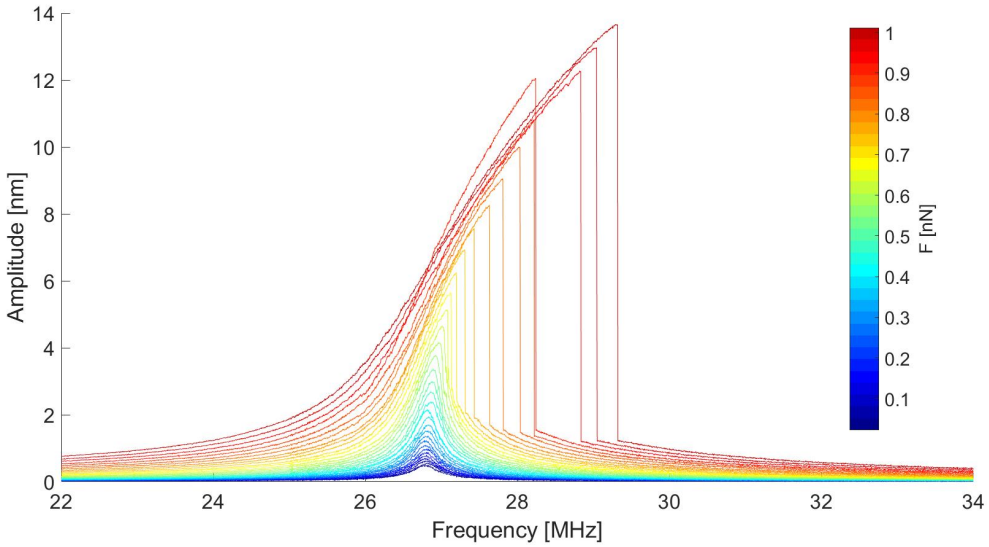

Figure 2-7: Frequency response curves for different driving forces. At low driving forces, the response is essentially linear. As the driving force increases, the response goes from linear to nonlinear, and the membrane shows a stiffening effect where the resonance frequency becomes amplitude dependent.

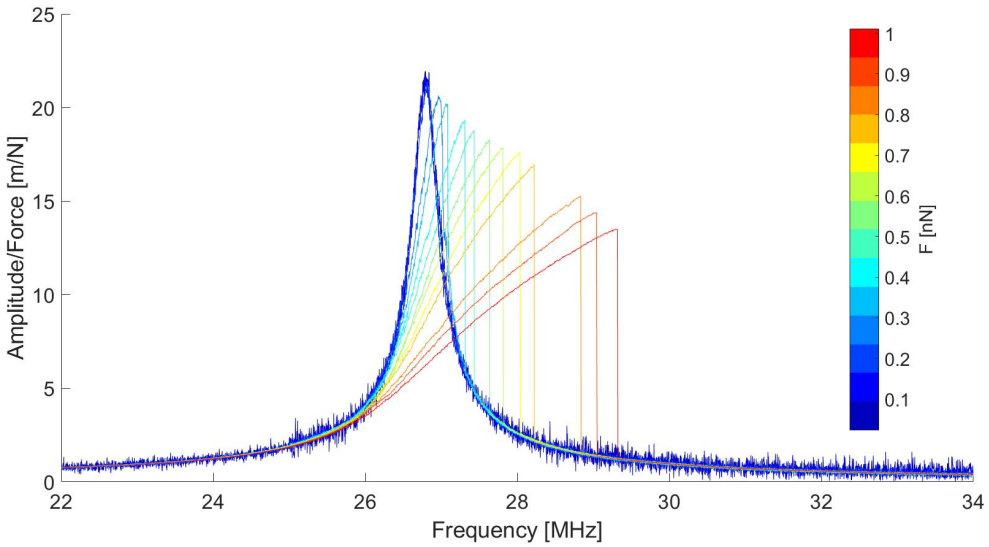

Figure 2-8: Responsivity plot for different driving forces. A strong decrease of responsivity with increasing driving force indicates the importance of nonlinear dissipation.

Table 2-2: Known properties of the graphene membrane.

m_{eff} [kg]	ρ [kgm^{-3}]	h [nm]	a [μm]	f_0 [MHz]
6.313×10^{-17}	2330	8.0	2.0	26.787

known. Figure 2-8 clearly shows that the responsivity decreases with increasing drive force. This is a strong indication that a nonlinear dissipation plays an important role. Therefore, besides the Duffing nonlinearity, a positive nonlinear damping term should be included in the equation of motion of the membrane when forces are sufficiently high.

Other properties of the membrane, like its mass and thickness, were also measured. These properties are listed in table 2-2.

2-3 Fitting the response

2-3-1 Fitting strategy

From the previous section, it is clear that the membrane shows a Duffing type of nonlinearity and positive nonlinear dissipation. Therefore, equation 2-42 is a prime candidate to fit the nonlinear frequency response of this resonator. However, at low driving forces, both types of nonlinearities are not yet significant, and the simple harmonic oscillator model can be used to fit the linear response. The mathematical expression for a forced simple harmonic oscillator is:

$$m\ddot{\tilde{x}} + c\dot{\tilde{x}} + k\tilde{x} = F\cos(\omega\tilde{t}) \tag{2-43}$$

By expressing the natural frequency of the system as $\omega_n = \sqrt{k/m}$ and introducing new variables $t = \omega_n\tilde{t}$ and $x = \tilde{x}/h$, this equation is rewritten to:

$$\ddot{x} + Q^{-1}\dot{x} + x = \lambda\cos(\Omega t) \tag{2-44}$$

where Q is the mechanical Q-factor, $\lambda = \frac{F}{m\omega_n^2 h}$ and $\Omega = \omega/\omega_n$. Equation 2-44 can be used to fit the non-dimensionalized linear frequency response curves. Since the driving forces are known and ω_n is extracted easily from the curves, the Q-factor can be obtained in a straightforward manner.

At high driving forces, equation 2-42 is used to fit the nonlinear response. In this nonlinear regime, it is assumed that the nonlinear dissipation dominates the linear dissipation. The value for the Q-factor obtained from the linear fits is therefore fixed during the nonlinear fit process. This is an important assumption, as it effectively allows for the linear and nonlinear dissipation to be decoupled. Using this assumption, nonlinear dissipation can be quantified.

2-3-2 Nonlinear parameter identification

One way to obtain the fit parameters for the nonlinear stiffness and dissipation would be to use a brute force method. However, this is not very elegant, as it can become rather time-consuming to find the values for a proper fit. Another way is to follow an identification method

based on harmonic balancing by Delannoy [79], which has been used to find the parameters of the equations of motion of plates and shells under large amplitude vibrations [80,81]. In this thesis, the same method is followed and extended to include a nonlinear dissipation term. The method is only briefly explained here. A more detailed derivation can be found in Appendix A.

The equation of motion for which the parameters need to be identified is:

$$m_{\text{eff}}\ddot{\tilde{x}} + c_1\dot{\tilde{x}} + k_1\tilde{x} + k_3\tilde{x}^3 + c_3\tilde{x}^2\dot{\tilde{x}} = \xi F\cos(\omega\tilde{t}) \tag{2-45}$$

Normalizing the equation and scaling time with ω, this is rewritten to:

$$\Omega^2\ddot{x} + Q^{-1}\Omega\dot{x} + x + \alpha x^3 + \nu\Omega x^2\dot{x} = \lambda\cos(t) \tag{2-46}$$

with:

$$\Omega = \frac{\omega}{\omega_n} \tag{2-47}$$

$$Q^{-1} = \frac{c_1}{m_{\text{eff}}\omega_n} \tag{2-48}$$

$$\alpha = \frac{k_3h^2}{m_{\text{eff}}\omega_n^2} \tag{2-49}$$

$$\nu = \frac{c_3h^2}{m_{\text{eff}}\omega_n} \tag{2-50}$$

$$\lambda = \frac{\xi F}{m_{\text{eff}}\omega_n^2 h} \tag{2-51}$$

The steady-state solution to equation 2-46 is assumed to be of the form:

$$x = x_1\sin(t) + x_2\cos(t) \tag{2-52}$$

Filling the solution in into equation 2-46 and grouping the $\sin(t)$ and $\cos(t)$ terms gives two equations for each frequency step Ω. Since Ω consists of $\bar{M}$ frequency steps, this results in a system of equations that can be written as:

$$\mathbf{Ax} = \mathbf{b} \tag{2-53}$$

where $\mathbf{A}$ is a $2\bar{M}\times 2$ matrix, $\mathbf{x}$ is a 2×1 vector that contains α and ν, and $\mathbf{b}$ is a $2\bar{M}\times 1$ vector with known terms. This system is overdetermined, and the best possible solution for $\mathbf{x}$ is found by minimizing the least squares error:

$$\mathbf{x} = (\mathbf{A}^{\mathrm{T}}\mathbf{A})^{-1}\mathbf{A}^{\mathrm{T}}\mathbf{B} \tag{2-54}$$

If necessary, the value found for ν is corrected by forcing it to be such that the the maximum amplitude as obtained from the frequency response function is the same as the maximum amplitude as obtained from the data.

2-3-3 Result

The results from the fitting procedure are presented in this section. The first ten curves in figure 2-7 correspond to the ten lowest drive forces ($F \leq 0.064\,\text{nN}$). All fits are excellent,

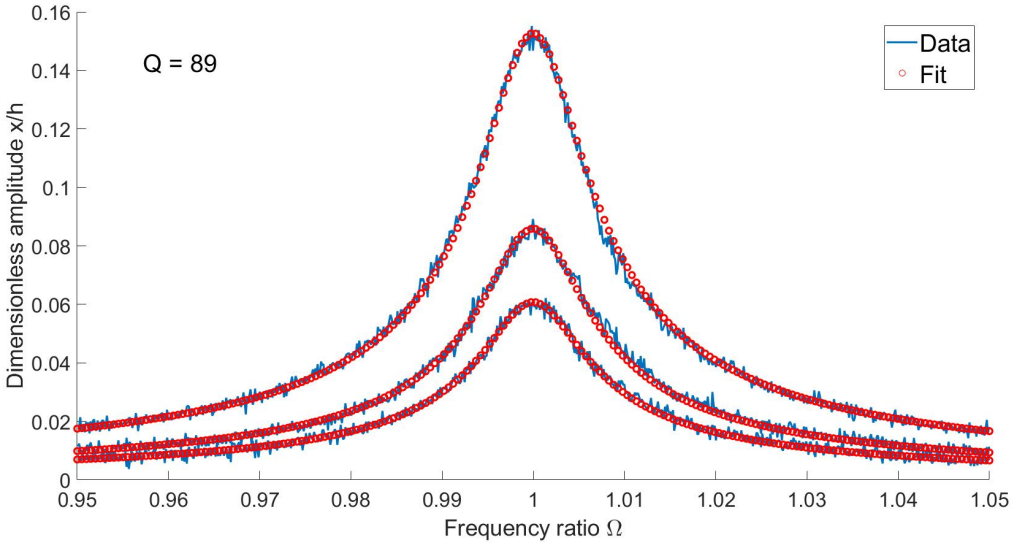

Figure 2-9: Three linear response curves and their fits. All curves with $F \leq 0.064\,\mathrm{nN}$ could be fitted using the model of a simple harmonic oscillator with $Q = 89$.

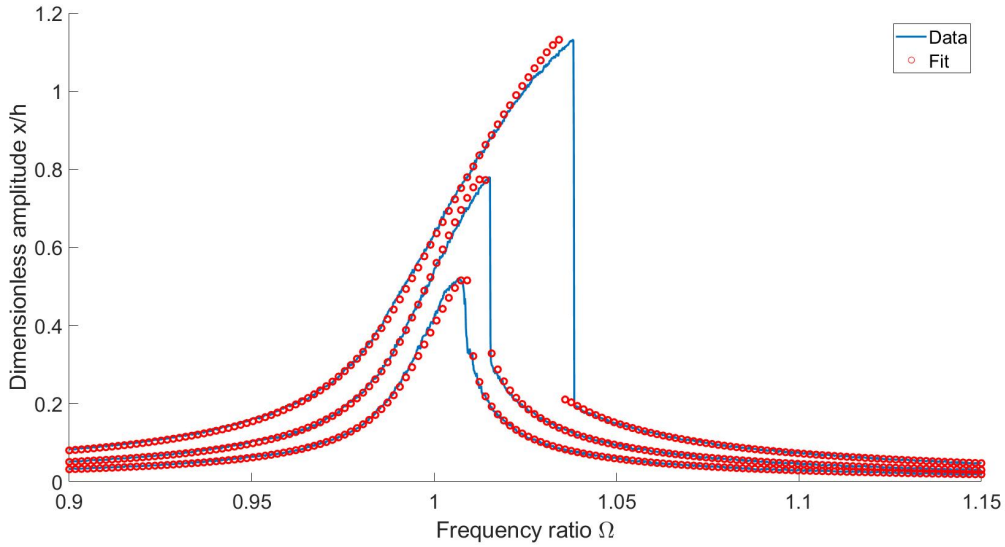

Figure 2-10: Three nonlinear response curves and their fits. The drive forces belonging to these curves are, from low to high, $F = 0.20\,\mathrm{nN}$, $F = 0.32\,\mathrm{nN}$ and $F = 0.51\,\mathrm{nN}$.

using the same Q-factor $Q = 89$ for every curve. This is shown in figure 2-9 for three of the ten linear curves. The response was calculated by numerically integrating the equation of motion using the ODE45 solver in Matlab. From this analysis, it can be concluded that at low drive forces, dissipation does not increase with amplitude, and can be described with the linear dissipation term only. For curves where the driving force $F > 0.064\,\mathrm{nN}$, the response starts to become nonlinear.

To fit the nonlinear frequency response curves, linear dissipation was fixed at $Q = 89$. For

Table 2-3: Results from the nonlinear fitting process. At each curve, a certain value for both α and ν is found.

F [nN]	0.20	0.23	0.25	0.29	0.32	0.36	0.40
α	0.083	0.076	0.067	0.060	0.059	0.062	0.065
ν	0.0054	0.0046	0.0057	0.0066	0.0064	0.0056	0.0060
F [nN]	0.45	0.51	0.57	0.64	0.80	0.90	1.0
α	0.073	0.074	0.076	0.076	0.086	0.085	0.086
ν	0.0059	0.0057	0.0049	0.0051	0.0059	0.0065	0.0071

three nonlinear curves, the result is plotted in figure 2-10. Eleven other fits (14 in total) belonging to the highest drive forces are shown in Appendix B-1. The fits seem very reasonable, but are not perfect. The method of finding the nonlinear fit parameters is fully automated, and it only takes about a second to find the values for all curves. Therefore, this method is preferred over the brute force method. Table 2-3 shows the values of α and ν that were obtained by fitting each of the 14 nonlinear curves individually.

2-4 Determining material properties

From section 2-1, it became clear that material properties are associated with the coefficients of the equation of motion of the membrane. The coefficients were then related to the fit parameters in section 2-3. Thus, the material properties listed in table 2-1 can now be determined for both the Kelvin-Voigt and standard linear solid models.

2-4-1 Kelvin-Voigt

There are three properties that can be determined from the fits: the pre-tension n_0, the Young's Modulus E and creep time τ_c. However, for membranes the pre-tension is also directly linked to the fundamental resonance frequency ω_n. The fundamental frequency can easily be extracted from the frequency response curves. The relation, which follows from the wave equation, is:

$$n_0 = \rho h \left(\frac{a\omega_n}{2.405} \right)^2 \tag{2-55}$$

Filling in all the values gives $n_0 = 0.365\,\mathrm{N/m}$. This still leaves the Young's Modulus and the creep time to be determined from the fits.

1. The Young's Modulus is directly related to the nonlinear spring stiffness. By using equation 2-49, the Young's Modulus is found with

$$E = \frac{\alpha a^2 m_{\text{eff}} \omega_n^2}{2.840 h^3} \tag{2-56}$$

2. The creep time is directly related to the nonlinear dissipation. By using equation 2-50 and the Young's Modulus, the creep time is found with

$$\tau_c = \frac{\nu a^2 m_{\text{eff}} \omega_n}{4.260 h^2 E} \tag{2-57}$$

Using the data from tables 2-2 and 2-3, E and τ_c are determined at all drive forces where a fit was done. The results are shown in figure 2-11. Except for the first few points, the Young's Modulus shows an approximately linear behavior, although it does seem to flatten out for the highest drive forces. Unfortunately, there were no higher forces available to confirm this. The behavior of τ_c is more random, showing no clear trend. Since E and τ_c are known now, the creep function for graphene can be found (see equation 2-14).

It would be interesting to see if reasonable fits can still be obtained using just one value for α and ν. This would then lead to a single value for E and τ_c as well. At higher amplitudes, the nonlinear effects will be bigger. Therefore, a weighted average of the fit parameters corresponding to the six highest drive forces is taken. The average values for α and ν are then:

$$\alpha_{\text{av}} = \frac{\sum_{i=1}^{6}(c_i - 1)\alpha_i}{\sum_{i=1}^{6}(c_i - 1)} \tag{2-58}$$

$$\nu_{\text{av}} = \frac{\sum_{i=1}^{6}(c_i - 1)\nu_i}{\sum_{i=1}^{6}(c_i - 1)} \tag{2-59}$$

Here, $c_i = F_i/F_{\text{lin}}$ is an added weight based on the drive force, where F_{lin} is one of the drive forces in the linear regime. The corresponding averaged values of the nonlinear coefficients

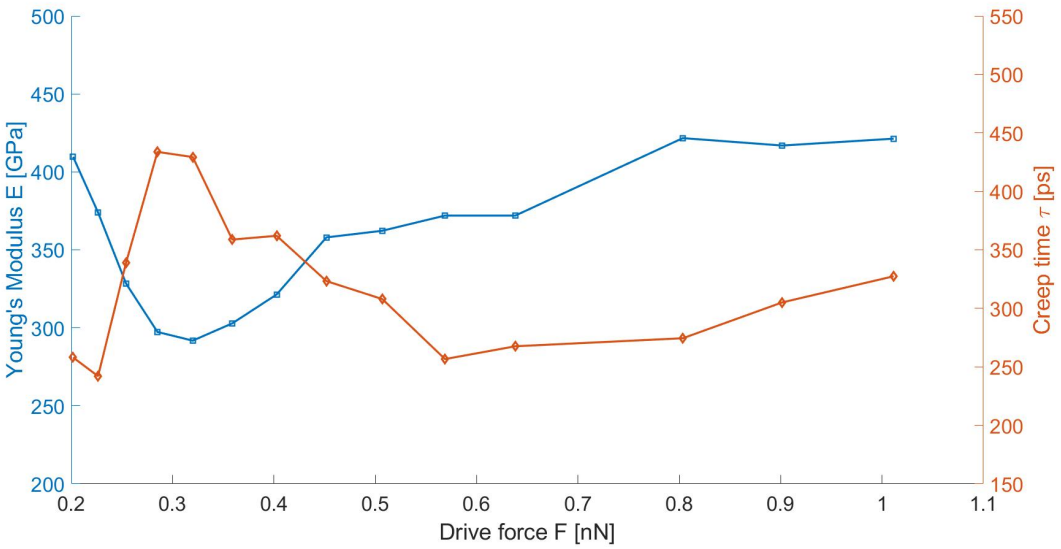

Figure 2-11: Results for the Young's Modulus E and creep time τ using the Kelvin-Voigt material model. E and τ are directly related to the fit parameters, and are determined here for every curve individually.

are then:

$$E_{\text{av}} = 400.58\,\text{GPa} \tag{2-60}$$

$$\tau_{\text{c,av}} = 294.29\,\text{ps} \tag{2-61}$$

The fits using these values for all 14 nonlinear curves are shown in Appendix B-2. Typically, the values for E found with AFM indentation techniques are 430-1200 GPa [82].

2-4-2 Standard linear solid

When using the the standard linear solid model, the are three unknowns to be determined are E_1, E_2, and relaxation time τ_r. These properties are related to the dimensionless nonlinear stiffness coefficient α and the dimensionless nonlinear dissipation coefficient ν in the following way:

$$\alpha = \frac{2.840h^3}{m\omega_n^2 a^2}E_2 + \frac{2.840h^3}{m\omega_n^2 a^2}\frac{\tau_r^2\omega^2}{1+\tau_r^2\omega^2}E_1 \tag{2-62}$$

$$\nu = \frac{4.260h^3}{m\omega_n a^2}\frac{\tau_r}{1+\tau_r^2\omega_n^2}E_1 \tag{2-63}$$

To disentangle the material properties from one another, α is first written in terms of ν. Furthermore, close the the resonance frequency, $\omega \approx \omega_n$. Equation 2-62 then becomes:

$$\alpha = b_1 E_2 + b_2 \nu \tau_r \tag{2-64}$$

with

$$b_1 = \frac{2.840h^3}{m\omega_n^2 a^2} \tag{2-65}$$

$$b_2 = \frac{2.840\omega_n}{4.260} \tag{2-66}$$

Since α and ν were determined for 14 curves in total, equation 2-64 leads to a system of 14 equations. Initially, another least squares optimization of the error was tried to find the best solution for E_2 and τ_r. However, this leads to a negative value for τ_r. Therefore, a brute force method was applied to minimize the error and obtain E_2 and τ_r. Next, E_1 is found by using equation 2-63 and the average value of ν as obtained from equation 2-59. This results in:

$$E_1 = 153.82\,\text{GPa} \tag{2-67}$$

$$E_2 = 244.34\,\text{GPa} \tag{2-68}$$

$$\tau_r = 45.28\,\text{ns} \tag{2-69}$$

Moreover, the creep time is related to the retardation time and is given by [7]:

$$\tau_c = \tau_r \frac{E_1 + E_2}{E_2} = 73.79\,\text{ns} \tag{2-70}$$

These four properties are all that is necessary to determine the relaxation and creep response functions, and the storage and loss moduli (see equation 1-5). For the standard linear solid

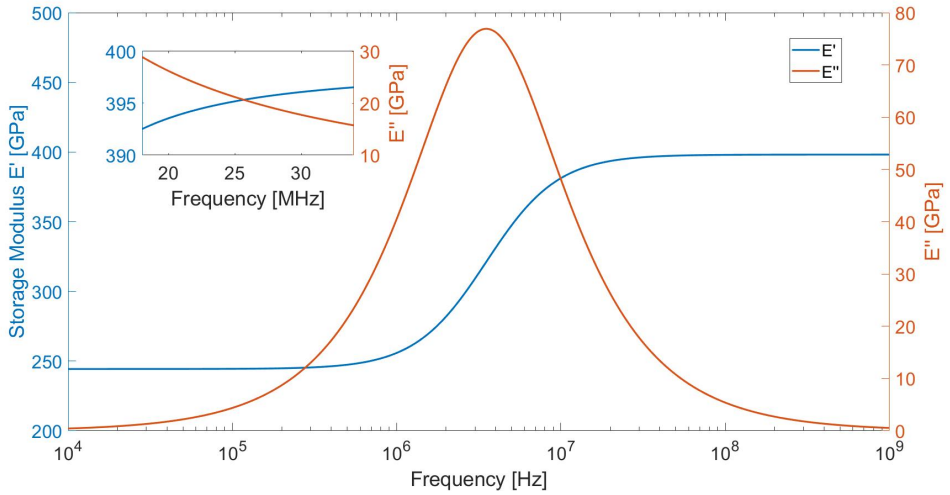

Figure 2-12: Logarithmic plot for storage modulus E' and loss modulus E'' as a function of frequency. Inset: E' and E'' for a selected frequency range around resonance.

model these are, respectively:

$$E(t) = E_2 + E_1 e^{-t/\tau_r} \tag{2-71}$$

$$J(t) = \frac{1}{E_2} - \frac{E_1}{E_2(E_1 + E_2)} e^{-t/\tau_c} \tag{2-72}$$

$$E'(\omega) = E_2 + E_1 \frac{\omega^2 \tau_r^2}{1 + \omega^2 \tau_r^2} \tag{2-73}$$

$$E''(\omega) = E_1 \frac{\omega \tau_r}{1 + \omega^2 \tau_r^2} \tag{2-74}$$

A plot of the storage and loss modulus as a function of frequency is shown in figure 2-12.

2-4-3 The loss tangent

The loss tangent is a measure of the internal friction of the material, and therefore the dissipation. It can be obtained in three different ways based on the results derived in the previous sections.

1. Method 1 makes use of the expressions found for E' and E'', see equations 2-73 and 2-74. The loss tangent is defined as $\tan\delta = E''/E'$ (see equations 1-8 and 1-9). Figure 2-13 shows the loss tangent as a function of frequency. Near the resonance frequency, the loss tangent decreases as the excitation frequency increases. At resonance, $\tan\delta = 0.050$.

2. Method 2 relies on the introduction of a complex Young's Modulus $E^* = E' + iE''$ in the Duffing equation [83]. The Duffing term is proportional to the Young's Modulus: $k_3 = CE$, where C is a constant [65]. Near the resonance frequency and for harmonic motion $x = x_0 e^{-i\omega_n t}$, this becomes:

$$CEx^3 = CE'x^3 + \frac{CE''}{\omega_n} x^2\dot{x} = \alpha x^3 + \nu x^2 \dot{x} \tag{2-75}$$

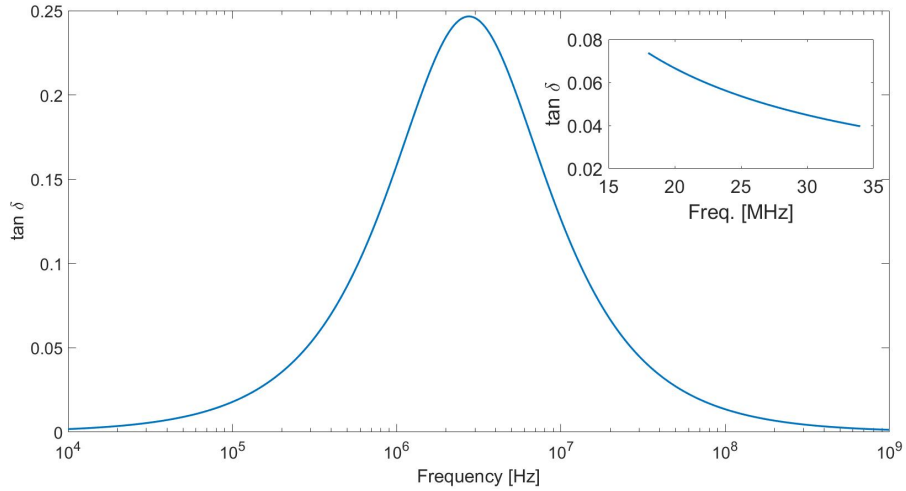

Figure 2-13: Loss tangent determined from the storage and loss modulus. Inset: $\tan\delta$ for a selected frequency range around resonance.

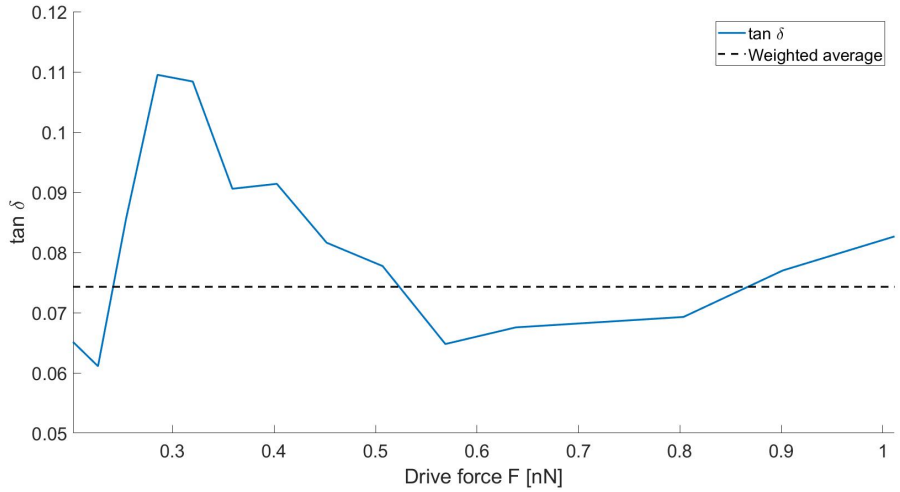

Figure 2-14: Loss tangent determined from equation 2-76 for different drive forces. The dotted line indicates the value of the loss tangent when the weighted averages of α and ν (equations 2-58 and 2-59) are used.

Therefore, the loss tangent is directly related to the nonlinear fit parameters as

$$\tan\delta = \frac{\nu}{\alpha} \tag{2-76}$$

Using equation 2-76, the loss tangent can be calculated for each drive force. This is shown in figure 2-14. Alternatively, the averaged values of α and ν can be used to find one value for the loss tangent. This result in a loss tangent of $\tan\delta = 0.0743$. In Ref. [83], $\tan\delta = 0.15$ was found for a single layer graphene resonator. The lower loss tangent seen in this work could be due to the fact that more strain energy can be stored in a system with multiple graphene layers.

3. Method 3 is to determine the loss tangent from the force-displacement loops. The loss tangent is a ratio between energy lost and energy stored in the system. Both energies can be calculated from the force displacement loop, as indicated in figure 2-15 for a certain frequency of excitation. Note that, for nonlinear systems, the loop does not have to be symmetric. Moreover, as the excitation frequency is increased, the loop will rotate due to the phase change between force and displacement. The storage energy W_s is given by [84]:

$$W_{s1} = \frac{1}{2}x_{\max}^2 + \frac{1}{4}\alpha x_{\max}^4 \tag{2-77}$$

$$W_{s2} = \frac{1}{2}x_{\min}^2 + \frac{1}{4}\alpha x_{\min}^4 \tag{2-78}$$

$$W_s = W_{s1} + W_{s2} \tag{2-79}$$

where $x_{\max}$ and $x_{\min}$ are the maximum and minimum displacement. The dissipated energy is represented by the area enclosed by the loop. A force-displacement curve can be made for every excitation frequency. Therefore, a loss tangent dependent on frequency is obtained. Figure 2-16 shows the loss tangent for three different drive forces around the resonance frequency. The loss tangent is highest at resonance, and reaches up to 0.046 for the highest drive force.

2-5 Conclusion

In this chapter, the equation of motion of a graphene membrane was derived using an energy approach. By introducing a viscoelastic material model that operates in the geometrically nonlinear regime, an amplitude-dependent damping term was obtained. This form of nonlinear damping is widely used in phenemonoligcal approaches as well. Therefore, nonlinear damping in graphene resonators could be induced by geometric nonlinearities.

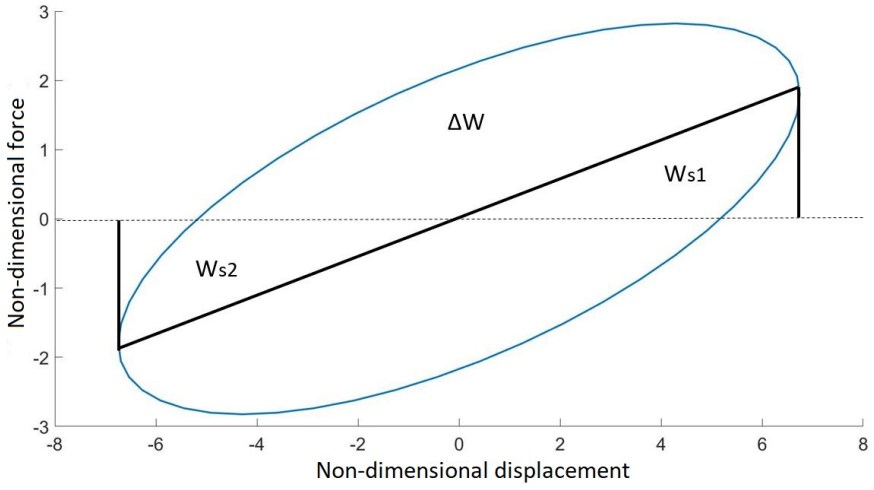

Figure 2-15: Force-displacement loop for a certain frequency of excitation. As the frequency is increased, the loop changes. The areas underneath the two triangles, indicated with W_{s1} and W_{s2}, represent the storage energy. The area enclosed by the loop is the amount of energy dissipated.

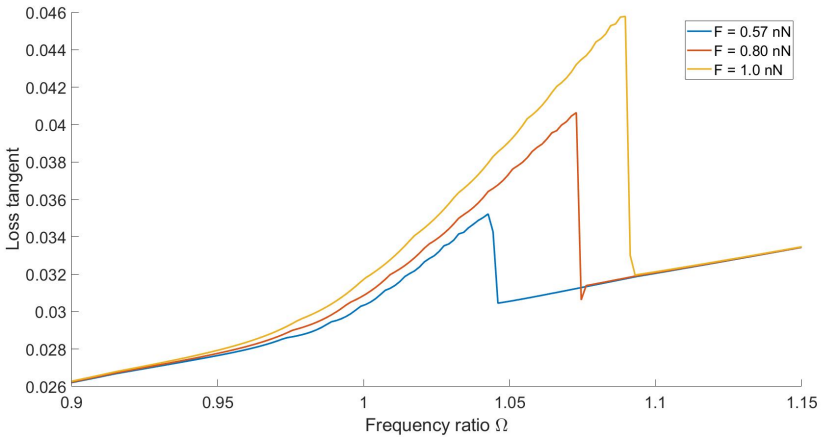

Figure 2-16: Loss tangent as obtained from the force displacement loops for three different drive forces. The highest loss tangent reaches up to 0.046 for the highest drive force when the system is at resonance frequency.

A fitting algorithm was developed that could automatically obtain the values of the coefficients of the equation of motion for each nonlinear response curve. The coefficients were correlated back to viscoelastic properties of the material, from which a loss tangent of 0.050 was obtained. Two other methods for obtaining the loss tangent were shown as well and resulted in $\tan\delta = 0.0743$ and $\tan\delta = 0.046$. These values are relatively high for a crystalline material, comparable to polymers. A possible explanation for such a high loss tangent could be that during the exfoliation process, polymer particles contaminated the graphene sample. For a comparison to other materials, see figure 2-17.

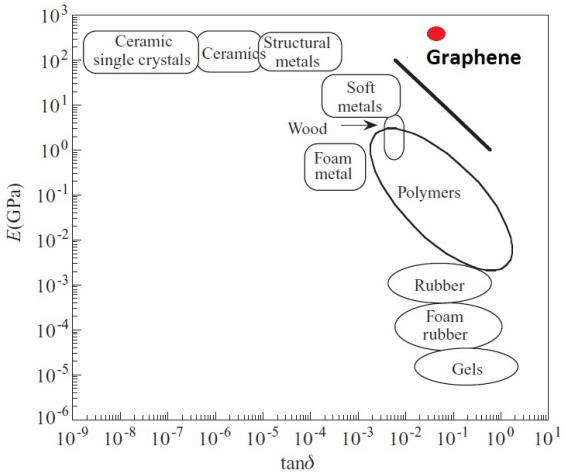

Figure 2-17: Stiffness-loss map. Graphene, indicated with the red dot, was measured to have a loss tangent comparable to that of polymers. Adapted from: [7].

Chapter 3

Paper: Nonlinear dissipation in graphene optomechanics

Nonlinear dissipation in graphene optomechanics

Justin A. Smid*
Department of Precision and Microsystems Engineering
Delft University of Technology
(Dated: February 7, 2019)

Graphene resonators shows signs of nonlinear dissipation at relatively small amplitudes. However, only very little is known about its origin. Here we investigate the influence of the optical field on nonlinear dissipation in a single-layer graphene resonator that is coupled to an optical cavity to detect its motion. The resonator is actuated by a separate laser through the photothermal force. We observe that nonlinear dissipation is negative when the laser powers are low, but turns positive as the laser powers increase. This effect is attributed to the optical field. We find that the nonlinear dissipation is sensitive to the equilibrium position of the membrane, and could explain the negative nonlinear dissipation.

Due to their high sensitivity, mechanical resonators made from graphene sheets are widely researched for their potential applications. Examples include pressure sensors [1, 2], gas sensors [3] and mass sensors [4, 5]. Their atomically thin nature makes these resonators highly susceptible to nonlinear effects at relatively small driving forces [6]. Most notable of these effects is the onset of the Duffing nonlinearity, which describes a nonlinear restoring force. Nonlinear dissipative behavior has also been observed in graphene resonators when driven into the nonlinear regime [7]. To further improve device response and sensitivity, it is essential to understand the dissipative processes. A variety of physical mechanisms can contribute to linear dissipation in nanomechanical resonators [8–13]. For graphene resonators specifically, Ohmic dissipation due to trapped charges in the graphene sheet or substrate can add to the dissipation process [14], as well as sidewall adhesion [15] and interlayer slippage [16, 17]. On the other hand, only a few theories have been proposed to correctly describe nonlinear dissipation. It has been hypothesized that a combination of a standard dissipation channels, such as clamping losses, and geometrical nonlinearities could result in nonlinear dissipation [7]. Other possible explanations are the coupling between flexural modes and in-plane phonons [18], and nonlinear mode coupling [19, 20]. Negative nonlinear damping was observed in a multilayer graphene resonator at low temperature [21]. However, the origin of nonlinear dissipation remains largely unknown.

In this paper, we show that nonlinear dissipation in a graphene resonator could arise from optical effects. The circular resonator is part of an interferometric setup, where it acts as a moving mirror in a Fabry-Pérot cavity in order to actuate and detect its motion [22–25]. The amplitude-frequency response is fitted using a normalized van der Pol-Duffing equation. The nonlinear damping parameter is extracted and correlated back to theoretical models which we built, accounting for the effect of the optical field. We find that for low laser powers, negative nonlinear damping is observable, which turns positive as the laser power is increased. We think that the optical field lies at the root of observing the negative nonlinear damping.

In principle, when a graphene resonator is coupled to an optical cavity, the linear response is modified. The light field then induces an optomechanical damping effect too. Depending on the wavelength of the light, the cavity geometry and the position of the membrane, the optomechanically induced damping can be positive or negative and increases or decreases with the laser power, respectively. In fact, it is even possible to induce self-oscillations in the system if the optomechanical damping is negative and the laser power is high enough [26]. However, optomechanically induced nonlinear damping has not yet been explored.

In our experiments, the circular graphene resonator consists of a single layer of chemical vapor deposited graphene that is suspended over a cavity, which was created by etching in a 300 nm thick layer of silicon dioxide (SiO_2). The resulting membrane has a radius of $a = 1.5\mu$m. More details on the sample fabrication can be found in Ref. [25]. The graphene membrane and the silicon substrate form a Fabry-Perot cavity. Detection of the membrane motion is done using a 633 nm wavelength red Helium-Neon laser. The membrane acts as a moving mirror, and causes interference of the waves that are reflected off of the membrane and the substrate. A photodiode (PD) is used to detect the intensity of the reflected light. A 405 nm wavelength blue diode laser of which the intensity is modulated is used for actuation. The membrane is periodically heated, and provided that the membrane is not perfectly straight, thermal expansion forces deflect the membrane in the out-of-plane direction [27]. A vector network analyzer (VNA) is also used to measure both the photodiode signal and the modulation signal of the blue diode laser. The measurement setup is shown schematically in Fig. 1a. All measurements were done at low pressures of no more than 0.02 μbar and at room temperature.

The motion amplitude of the resonator was calibrated by a nonlinear optical transduction technique [27]. The

* J.A.Smid@student.tudelft.nl

experimental result is shown in Fig. 1b for different DC powers of the blue laser while the red laser is kept constant. At the lowest blue laser power, the response is linear, while at the three other powers, the response is nonlinear. Similar curves were obtained for other values of the red laser power (see Supporting Information I). When nonlinear dissipation is present within the system, the normalized van der Pol-Duffing equation is oftentimes used to describe the nonlinear response [28]:

$$\ddot{x} + Q^{-1}\dot{x} + x + \eta x^3 + \xi x^2 \dot{x} = G\cos(\Omega t). \qquad (1)$$

Here, Q is the Q-factor, η is the Duffing parameter, G is the force amplitude and Ω is the ratio between the excitation frequency ω and the fundamental frequency ω_n. The term $\xi x^2 \dot{x}$ is used as a phenomenological ansatz to describe amplitude-dependent nonlinear damping in nanomechanical resonators [7, 25, 28].

To quantify nonlinear behavior of the graphene resonator, the following strategy is employed. First, a Lorentzian is fitted to the linear response (Fig. 2a). From this, the Q-factor and ω_n are obtained. The nonlinear response curves are then fitted by using Eq. (1), while the Q-factor is kept constant since nonlinear damping is assumed to dominate linear damping in this regime. The normalized force G is first determined by looking at vertical offset from the horizontal axis (Fig. 2b). The Duffing parameter η determines the degree of hardening in the frequency response and is found second (Fig. 2c). Nonlinear damping parameter ξ only affects the position of the limit point that is associated with the jump in amplitude, and can be found last (Fig. 2d). The results for Q, ω_n, η and ξ obtained from fitting are listed in Supporting Information II.

The fitting results show that linear dissipation decreases (Q increases) with increasing red laser power. On the other hand, nonlinear dissipation increases with red laser power, as shown in Fig. 3a. Moreover, negative nonlinear damping can be observed at low powers for all actuation levels. The obtained values are not absolute however, and a slight variation in Q or F could lead to different values for ξ. Therefore, histograms were made, presented in 3b, by varying both Q and G up to $\pm 10\%$ and observing the value for ξ that could still fit the response. Similar sensitivity analyses were done for all laser powers where negative nonlinear damping was found. The result is shown in Fig. 3c, where the error bars indicate one standard deviation. Although the error bars are relatively large for $P_b = -20\,\mathrm{dBm}$ at low red laser powers, the analysis clearly shows that negative values of the nonlinear damping persist. Further indications are given by the responsivity plot in Fig. 3d. The increase in responsivity for the curves related to $P_b = -20\,\mathrm{dBm}$ and $P_b = -10\,\mathrm{dBm}$ with respect to the linear curve suggests the presence of negative nonlinear damping [28]. Although nonlinear damping can be negative, the net damping of the system has remained positive for all laser powers and is shown in Fig. 3e. To obtain

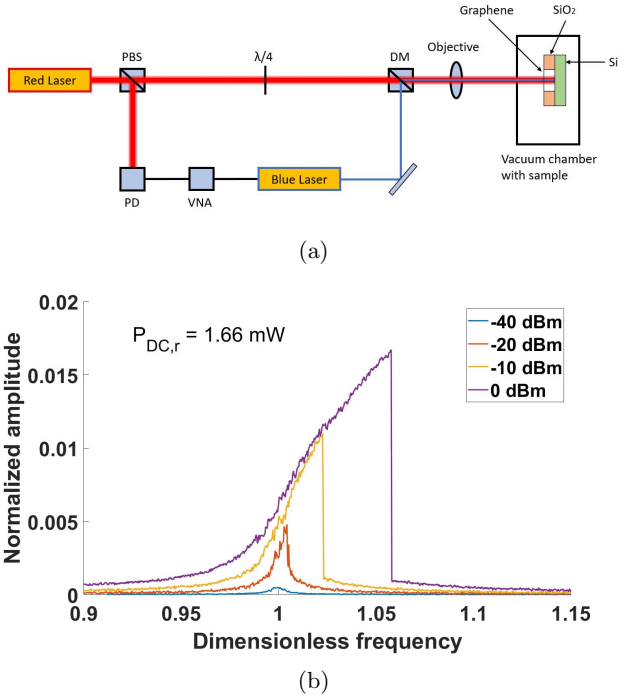

FIG. 1: (a) Experimental setup. The graphene resonator is part of a Fabry-Perot interferometer. (b) Response curves corresponding to four different DC actuation powers. The red laser power stays constant at $P_{DC,r} = 1.66\,\mathrm{mW}$.

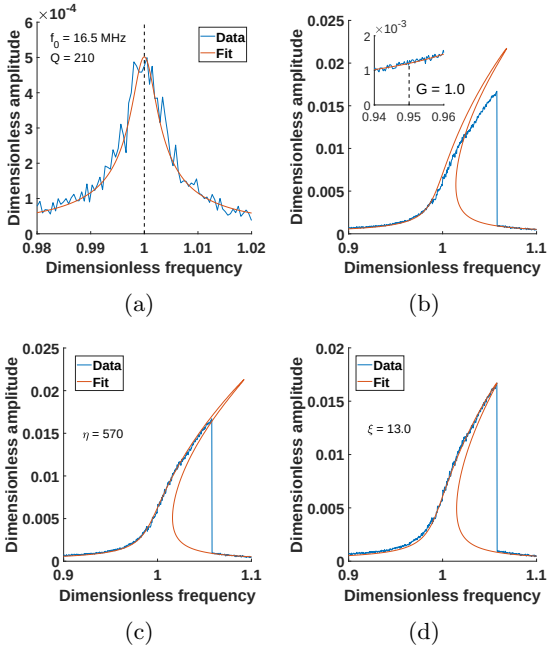

FIG. 2: Example of the fitting procedure. (a) A Lorentzian is used to fit the linear response. (b) Eq. (1) is used to fit the nonlinear response. G determines the offset from the horizontal axis. (c) The duffing parameter η is determined from the hardening effect. (d) Nonlinear damping ξ is determined by finding the correct position of the limit point.

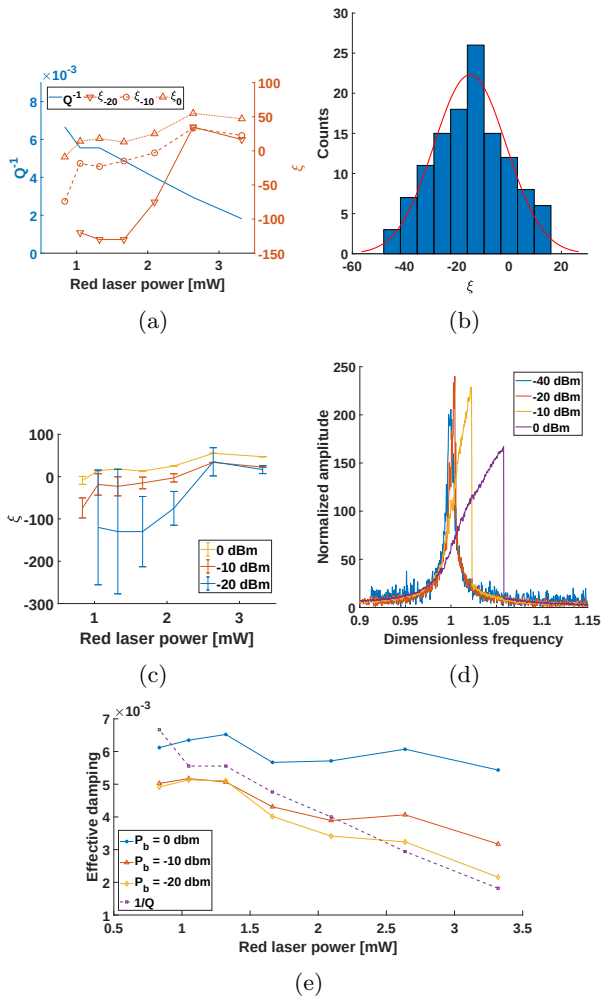

FIG. 3: (a) Results from the fitting procedure showing linear and nonlinear dissipation. Linear dissipation is a decreasing with increasing with red laser power, while nonlinear dissipation increases. (b) Histogram showing the normal distribution of values of ξ when a 10% variation in both Q and G is allowed. Here, $P_{DC,r} = 1.66\,\mathrm{mW}$ and $P_b = -10\,\mathrm{dBm}$. (c) Sensitivity of the nonlinear dissipation to a $\pm 10\%$ change in both Q^{-1} and force G. The error bars indicate one standard deviation. (d) Responsivity plot for $P_{DC,r} = 1.66\,\mathrm{mW}$. The increase in responsivity suggests negative nonlinear damping. (e) Effective damping stays positive for all laser powers.

the net damping, we used:

$$\chi_{\mathrm{net}} = Q^{-1} + \frac{1}{4}\xi X^2 \tag{2}$$

where X is the amplitude of motion.

To explain both the power dependence of the dissipation and the negative nonlinear damping, we looked at the influence of of the optical field on the nonlinear parameters of the system. The force acting on the membrane is due to photothermal action and is modeled as a time-delayed photon-induced force [29, 30]:

$$F(x(t),t) = F_{ph}(x_0) + \int_0^t \left(\frac{\partial F_{ph}}{\partial x}\frac{\partial x}{\partial t'} + \frac{\partial F_{ph}}{\partial t'}\right) h(t-t')dt', \tag{3}$$

where F_{ph} is the photon-induced force and $h(t)$ is a delay function. The delay is due to the fact that it takes a finite amount of time for the heat to conduct along the membrane and change the temperature. This time is characterized by the thermal time constant τ, which was determined in our experiment using the technique proposed in Ref. [25], and is equal to 28.3 ns. The photothermal force is directly related to the power that is absorbed by the graphene membrane through a proportionality constant B, which can be obtained experimentally by looking at the Q-factor for different red laser powers as shown in Supplementary Information V. For large-amplitude vibrations, the absorbed power is a function of the membrane position in the optical cavity. This can be calculated using [31]:

$$P_{\mathrm{abs}} = AP_i = (1 - R - T)P_i, \tag{4}$$

where A is the fraction of energy absorbed, R is the reflectivity, T is the transmittance and P_i is the incident power. Expressions for R and T were found by using the matrix method, as shown in Supporting Information III. For the graphene layer, refractive indices $\tilde{n}_{\lambda=633\,\mathrm{nm}} = 2.73 + 1.36i$ and $\tilde{n}_{\lambda=405\,\mathrm{nm}} = 2.71 + 1.13i$ were used. Following this method, the fraction of absorbed energy can be expressed as a function of membrane position in the cavity for both the red and blue laser. Simple harmonic functions can be used to fit both curves. The result is then Taylor expanded, retaining terms up to the third order so that it can accurately describe the position-dependent absorbed power up to amplitudes of 30 nm. (See Supplementary Information IV.) Eq. (4) is filled in into Eq. (3), which after normalizing is written on the right hand side of Eq. (1). By writing the equation in the frequency domain and grouping in terms of ω, the optomechanically induced effects become visible in the equation of motion. A detailed derivation is given in Supporting Information IV. The effective coefficients for the linear and nonlinear dissipation become:

$$Q_{\mathrm{eff}}^{-1} = Q_{\mathrm{in}}^{-1} + Q_{\mathrm{op,r}}^{-1} + Q_{\mathrm{op,b}}^{-1}, \tag{5}$$

$$\xi_{\mathrm{eff}} = \xi_{\mathrm{in}} + \xi_{\mathrm{op,r}} + \xi_{\mathrm{op,b}}, \tag{6}$$

with

$$Q_{\mathrm{op,r}}^{-1} = \frac{BP_{i,r}\tau\beta_r\gamma_r\cos(\gamma_r g + \phi_r)}{(1+\omega^2\tau^2)m\omega_n}, \tag{7}$$

$$Q_{\mathrm{op,b}}^{-1} = \frac{BP_{i,b}\tau\beta_b\gamma_b\cos(\gamma_b g + \phi_b)}{(1+\omega^2\tau^2)m\omega_n}, \tag{8}$$

$$\xi_{\mathrm{op,r}} = -\frac{BP_{i,r}\tau\beta_r\gamma_r^3\cos(\gamma_r g + \phi_r)a^2}{2(1+\omega^2\tau^2)m\omega_n}, \tag{9}$$

$$\xi_{\mathrm{op,b}} = -\frac{BP_{i,b}\tau\beta_b\gamma_b^3\cos(\gamma_b g + \phi_b)a^2}{2(1+\omega^2\tau^2)m\omega_n}, \tag{10}$$

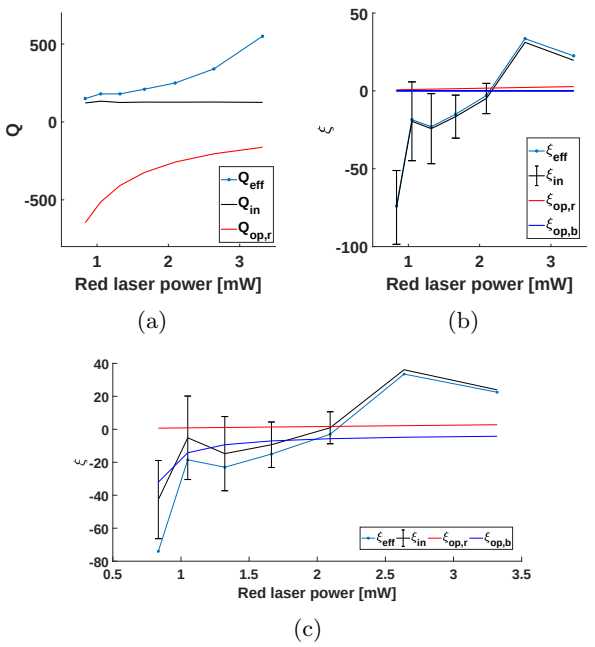

FIG. 4: (a) Q-factor against red laser power. The blue laser component is omitted since it was found to be negligible. The increase in Q is due to optomechanical damping. The intrinsic Q stays constant at 125. (b) Nonlinear dissipation against red laser power. The influence of the optical field is not found to be significant. For the case where $P_b = -10\,\mathrm{dBm}$. (c) Nonlinear dissipation against red laser power, where the equilibrium position of the membrane starts at 316 nm and increases linearly with red laser power.

where Q_{in}^{-1} and ξ_{in} refer to the intrinsic linear and nonlinear dissipation respectively. Subscript *op* refers to the optical contribution, subscripts r and b refer to the red and blue laser, β, γ, ϕ are the fit parameters from the absorption model, m is the resonator mass and g is the gap size of the cavity, which is approximately 300 nm.

Eqs. (7)-(10) were determined around resonance frequency where $\omega \approx \omega_n$. The results for the Q-factor are shown in Fig. 4a. At higher red laser powers, the increase in Q is entirely due to the optical field of the red laser. The effect of the blue laser on the Q-factor is trivial. The disentanglement of Q_{in}^{-1} from $Q_{\mathrm{op,r}}^{-1}$ and $Q_{\mathrm{op,b}}^{-1}$ helps us to nullify the decrease that was observed in Q_{eff}^{-1} in Fig. 3a, resulting in a constant Q of 125. The influence of the optical field on the nonlinear dissipation is far less significant. Fig. 4b shows this for the case where $P_b = -10\,\mathrm{dBm}$. Similar results were obtained for $P_b = -20\,\mathrm{dBm}$ and $P_b = 0\,\mathrm{dBm}$, showing only very little effect on nonlinear damping. We found that the equilibrium position of the graphene membrane can have a big influence on ξ_{in}. The constant illumination from both the red and blue laser can bulge the membrane, causing an offset and increasing the effective gap size. Trapped gas molecules and imperfections from the flat configuration are other reasons that could lead to a statically deformed configuration about the initial equilibrium position, thus further increasing the gap between the membrane and the silicon substrate. We hypothesize that due to an increase in equilibrium position with red laser power, the effect of the optical field on nonlinear damping can become significant. This is shown in Fig. 4c for the case where $P_b = -10\,\mathrm{dBm}$. The effective gap size is increased with 16 nm compared to the initial flat configuration of the membrane, and increases linearly with red laser power. More experimental work is needed to confirm this effect.

In conclusion, we investigated dissipation in single-layer graphene membranes. From fitting the frequency response curves, negative nonlinear damping was found and a sensitivity analysis was done to confirm its presence. As a possible source of the power dependence of the linear and nonlinear dissipation, the influence of the optical field on both parameters was examined. Although it clearly affects the linear dissipation, the influence on its nonlinear counterpart was not significant. However, the change in equilibrium position of the membrane due to laser illumination as well as geometric imperfections can lie at the root of such negative nonlinear damping behavior at low laser powers.

[1] J. Aguilera-Servin, T. Miao, and M. Bockrath, Applied Physics Letters **106** (2015), 10.1063/1.4908176.

[2] R. J. Dolleman, D. Davidovikj, S. J. Cartamil-bueno, H. S. J. V. D. Zant, and P. G. Steeneken, Nano Letters **16**, 568571 (2016).

[3] R. J. Dolleman, S. J. Cartamil-bueno, H. S. J. V. D. Zant, and P. G. Steeneken, 2D Materials **4** (2017).

[4] J. Atalaya, J. M. Kinaret, and A. Isacsson, Europhysics Letters **91** (2010), 10.1209/0295-5075/91/48001.

[5] T. Natsuki, J.-X. Shi, and Q.-Q. Ni, Journal of Applied Physics **114** (2014), 10.1063/1.4820522.

[6] D. Davidovikj, F. Alijani, S. J. Cartamil-Bueno, H. S. J. van der Zant, M. Amabili, and P. G. Steeneken, Nature Communications **8**, 1253 (2017).

[7] A. Eichler, J. Moser, J. Chaste, M. Zdrojek, I. Wilson-Rae, and A. Bachtold, Nature Nanotechnology **6**, 339 (2011).

[8] Y. Tao, J. M. Boss, B. A. Moores, and C. L. Degen, Nature Communications **5**, 1 (2014), arXiv:1212.1347.

[9] I. Wilson-Rae, Physical Review B - Condensed Matter and Materials Physics **77**, 1 (2008), arXiv:0710.0200.

[10] P. Mohanty, D. A. Harrington, K. L. Ekinci, Y. T. Yang, M. J. Murphy, and M. L. Roukes, Physical Review B - Condensed Matter and Materials Physics **66**, 854161 (2002).

[11] K. Kunal and N. R. Aluru, Physical Review B - Condensed Matter and Materials Physics **84**, 1 (2011).

[12] R. Lifshitz and M. L. Roukes, Physical Review B **61**,

5600 (2000).
[13] M. Takamura, H. Okamoto, K. Furukawa, and H. Yamaguchi, Journal of Applied Physics **116** (2014).
[14] C. Seoánez, F. Guinea, and A. H. Castro Neto, Physical Review B - Condensed Matter and Materials Physics **76**, 1 (2007), arXiv:0704.2225.
[15] J. S. Bunch and M. L. Dunn, Solid State Communications **152**, 1359 (2012).
[16] S. Y. Kim and H. S. Park, Applied Physics Letters **94** (2009), 10.1063/1.3099932.
[17] X. Wei, Z. Meng, L. Ruiz, W. Xia, C. Lee, J. C. Hone, S. Keten, and H. D. Espinosa, ASC Nano **10**, 1820 (2016).
[18] A. Croy, D. Midtvedt, A. Isacsson, and J. M. Kinaret, Physical Review B - Condensed Matter and Materials Physics **86** (2012), 10.1103/PhysRevB.86.235435, arXiv:1204.0911.
[19] M. I. Dykman and H. B. Chan, Nature Communications **9** (2018), 10.1038/s41467-018-05246-w.
[20] J. Güttinger, A. Noury, P. Weber, A. M. Eriksson, C. Lagoin, J. Moser, C. Eichler, A. Wallraff, A. Isacsson, and A. Bachtold, Nature Nanotechnology **12**, 631 (2017).
[21] V. Singh, O. Shevchuk, Y. M. Blanter, and G. A. Steele, Physical Review Bysi **245407**, 1 (2016).
[22] J. S. Bunch, A. M. Van Der Zande, S. S. Verbridge, I. W. Frank, D. M. Tanenbaum, J. M. Parpia, H. G. Craighead, and P. L. McEuen, Science **315**, 490 (2007).
[23] V. Singh, S. J. Bosman, B. H. Schneider, Y. M. Blanter, A. Castellanos-Gomez, and G. A. Steele, Nature Nanotechnology **9**, 820 (2014), arXiv:1403.5165.
[24] D. Davidovikj, J. J. Slim, S. J. Cartamil-bueno, H. S. J. V. D. Zant, P. G. Steeneken, and W. J. Venstra, Nano Letters **16**, 2768 (2016), arXiv:arXiv:1602.00135v1.
[25] R. J. Dolleman, S. Houri, A. Chandrashekar, F. Alijani, H. S. J. van der Zant, and P. G. Steeneken, Scientific Reports **8** (2018), arXiv:1711.08798.
[26] R. A. Barton, I. R. Storch, V. P. Adiga, R. Sakakibara, B. R. Cipriany, B. Ilic, S. P. Wang, P. Ong, P. L. McEuen, J. M. Parpia, and H. G. Craighead, Nano Letters **12**, 4681 (2012).
[27] R. J. Dolleman, D. Davidovikj, H. S. J. V. D. Zant, and P. G. Steeneken, Applied Physics Letters **111**, 1 (2017), arXiv:arXiv:1711.06056v1.
[28] R. Lifshitz and M. C. Cross, Review of nonlinear dynamics and complexity (Wiley) , 1 (2008).
[29] I. Favero, C. Metzger, S. Camerer, D. König, H. Lorenz, J. P. Kotthaus, K. Karrai, I. Favero, C. Metzger, S. Camerer, D. König, H. Lorenz, J. P. Kotthaus, and K. Karrai, Applied Physics Letters **90** (2007), 10.1063/1.2711181.
[30] C. Metzger, I. Favero, A. Ortlieb, and K. Karrai, Physical Review B **78** (2008), 10.1103/PhysRevB.78.035309.
[31] O. Stenzel, *The Physics of Thin Film Optical Spectra* (Springer, 2005).

Supporting Information

I. DEVICE RESPONSE FOR DIFFERENT RED LASER POWERS

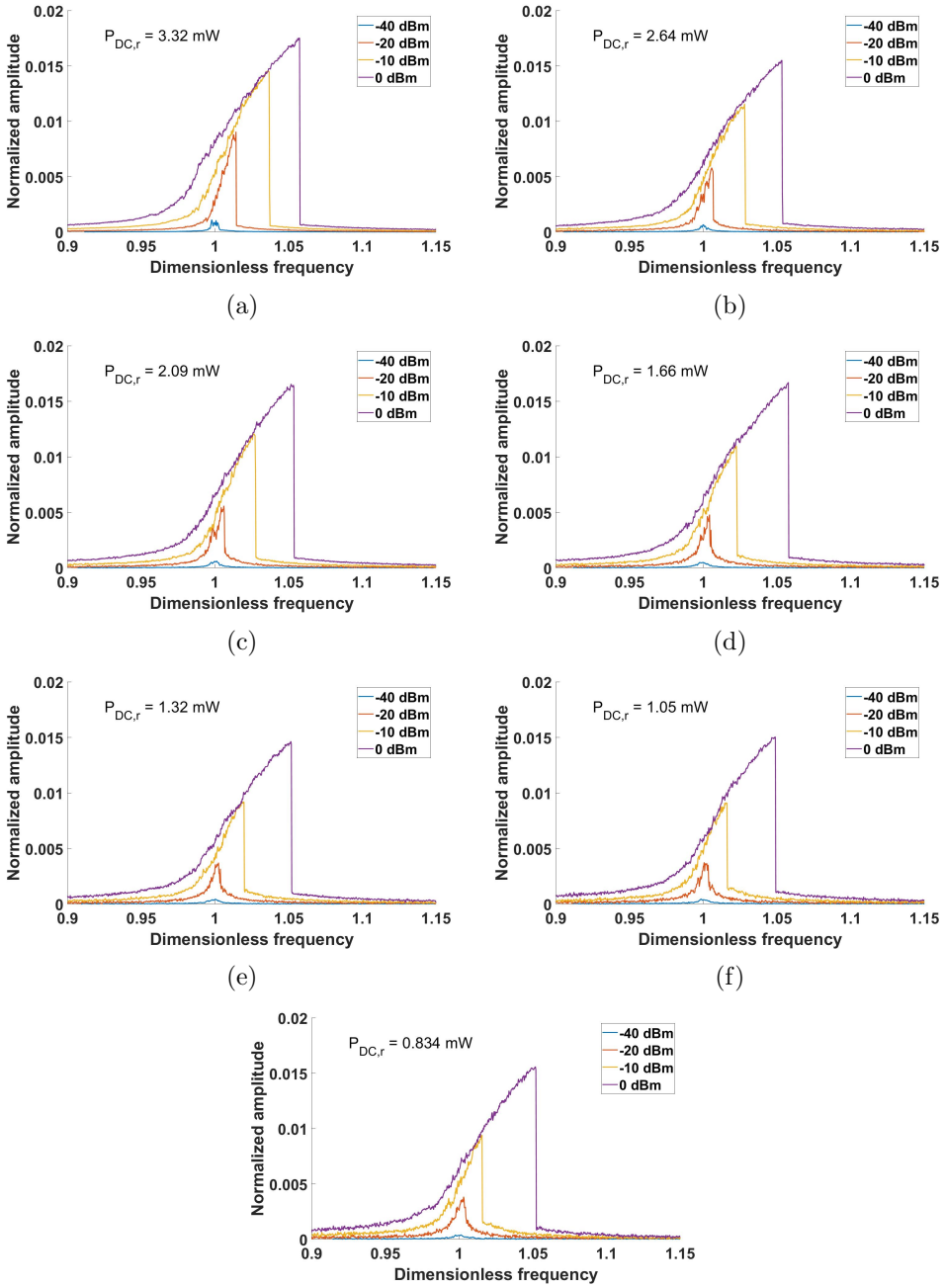

FIG. S1: Experimentally obtained frequency response curves. Each subfigure shows the response for four different blue laser powers $P_b = -40\,\mathrm{dBm}$, $P_b = -20\,\mathrm{dBm}$, $P_b = -10\,\mathrm{dBm}$ and $P_b = 0\,\mathrm{dBm}$. Red laser power varies from $3.32\,\mathrm{mW}$ down to $0.834\,\mathrm{mW}$.

II. LINEAR AND NONLINEAR FITS

A. Linear fits

The linear response curves were obtained for a blue laser actuation power of $P_b = -40$ dBm. The red laser powers were varied from 0.83 mW to 3.32 mW. The fits were obtained using a Lorentzian function. This results in a Q-factor and a fundamental frequency. The results are presented in Table S1. The fits are shown in the Fig. S2.

$P_{DC,r}$ [mW]	Q	f_0 [MHz]
3.32	550	16.46
2.64	340	16.58
2.09	250	16.54
1.66	205	16.44
1.32	180	16.50
1.05	180	16.46
0.83	150	16.41

TABLE S1: Results from fitting the linear response curves. $P_{DC,r}$ is the red laser power, Q is the Q-factor and f_0 is the fundamental frequency.

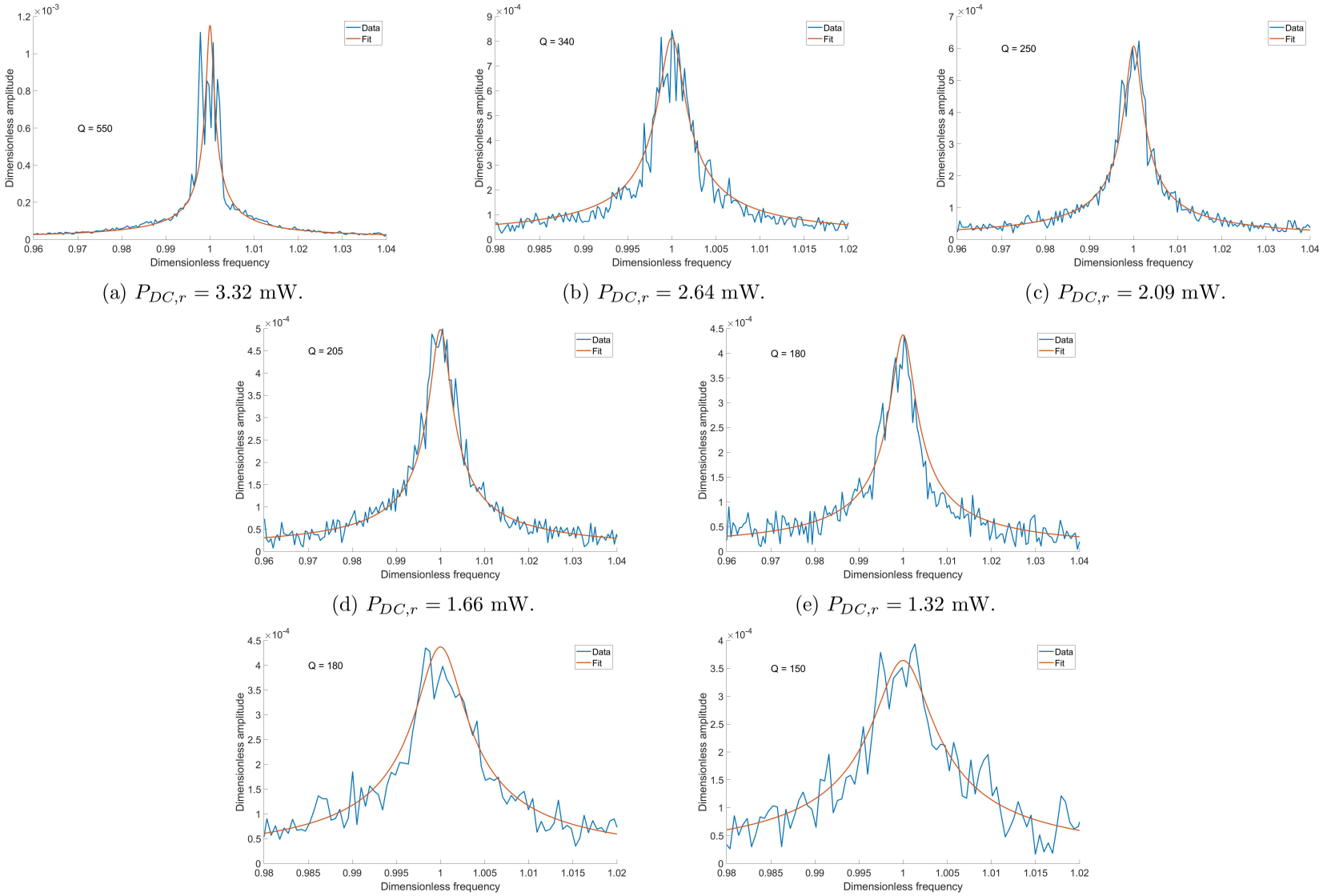

(a) $P_{DC,r} = 3.32$ mW. (b) $P_{DC,r} = 2.64$ mW. (c) $P_{DC,r} = 2.09$ mW.

(d) $P_{DC,r} = 1.66$ mW. (e) $P_{DC,r} = 1.32$ mW.

(f) $P_{DC,r} = 1.05$ mW. (g) $P_{DC,r} = 0.83$ mW.

FIG. S2: Linear fits. To actuate the membrane, a modulated blue laser was used with power $P_b = -40$ dBm. Each curve corresponds to a different red laser power $P_{DC,r}$

.

B. Nonlinear fits

The nonlinear response curves were obtained at three different blue laser powers: $P_b = -20\,\text{dBm}$, $P_b = -10\,\text{dBm}$ and $P_b = 0\,\text{dBm}$. At each actuation power, the red laser power was varied from 0.83 mW to 3.32 mW. The Duffing equation with an amplitude-dependent damping term added to it described the nonlinear response:

$$m\ddot{\tilde{x}} + \Gamma\dot{\tilde{x}} + k\tilde{x} + \alpha\tilde{x}^3 + \nu\tilde{x}^2\dot{\tilde{x}} = F\cos(\omega\tilde{t}), \tag{S-1}$$

Scaling time with $t = \omega_n\tilde{t}$ and amplitude with $x = \tilde{x}/a$, Eq. S-1 is rewritten as

$$\ddot{x} + Q^{-1}\dot{x} + x + \eta x^3 + \xi x^2\dot{x} = G\cos(\Omega t), \tag{S-2}$$

$$Q^{-1} = \frac{\Gamma}{m\omega_n} \tag{S-3}$$

$$\eta = \frac{\alpha a^2}{m\omega_n^2} \tag{S-4}$$

$$\xi = \frac{\nu a^2}{m\omega_n} \tag{S-5}$$

$$\lambda = \frac{F}{m\omega_n^2 a} \tag{S-6}$$

$$\Omega = \frac{\omega}{\omega_n} \tag{S-7}$$

Eq. S-2 was used to fit the nonlinear response curves. From the fits, values for η and ξ were obtained. The results are presented in Table S2. The fits are shown in the Figs. S3, S4 and S4 for a DC blue laser power of $P_b = -20$ dBm, $P_b = -10$ dBm and $P_b = 0$ dBm respectively.

$P_{DC,r}$ [mW]	$P_b = -20\,\text{dBm}$		$P_b = -10\,\text{dBm}$		$P_b = 0\,\text{dBm}$	
	η	ξ	η	ξ	η	ξ
3.32	420.0	16.5	490.0	25.5	610.0	47.0
2.64	510.0	35.0	570.0	33.5	660.0	52.0
2.09	515.0	-75.0	510.0	-3.0	550.0	25.0
1.66	530.0	-130.0	520.0	-15.0	570.0	13.0
1.32	510.0	-130.0	620.0	-23.0	660.0	18.0
1.05	420.0	-120.0	550.0	-18.5	620.0	14.0
0.83	520.0	-475.0	470.0	-74.0	600.0	-9.0

TABLE S2: Results from fitting the nonlinear response curves. $P_{DC,r}$ is the red laser power, P_b is the blue laser power, η is the nonlinear stiffness parameter and ξ is the nonlinear dissipation parameter.

The fits were obtained using the bifurcation and continuation software package AUTO [1]. This software package uses the pseudo-arclength method to trace all solution branches of the differential equation.

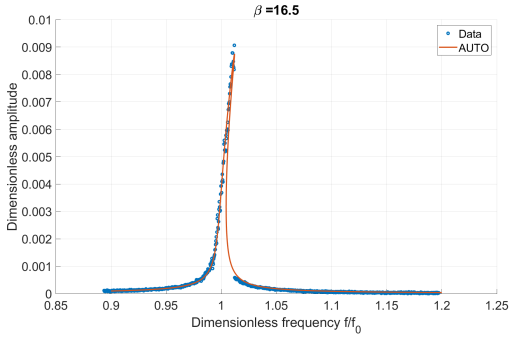

(a) $P_{DC,r} = 3.32$ mW.

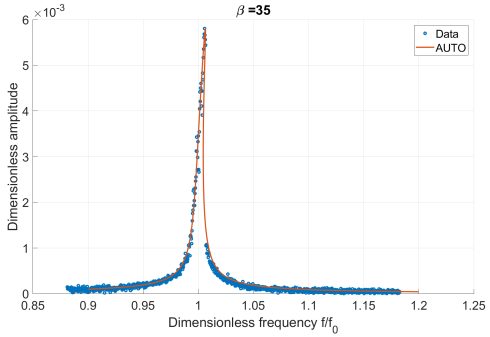

(b) $P_{DC,r} = 2.64$ mW.

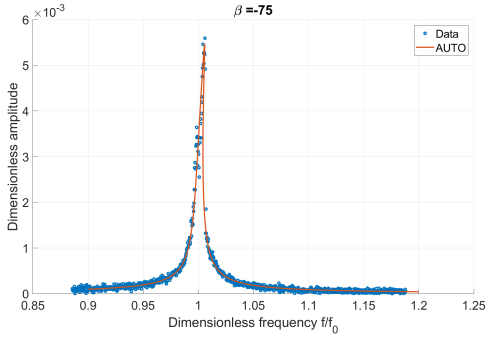

(c) $P_{DC,r} = 2.09$ mW.

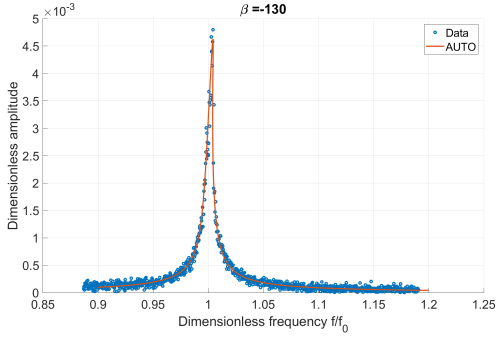

(d) $P_{DC,r} = 1.66$ mW.

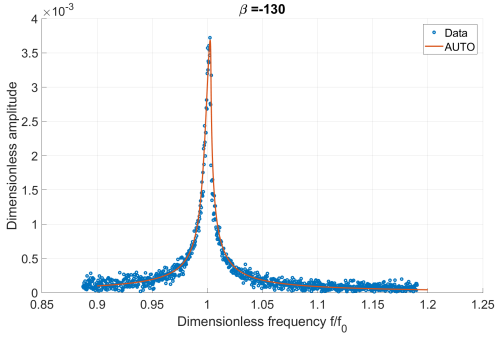

(e) $P_{DC,r} = 1.32$ mW.

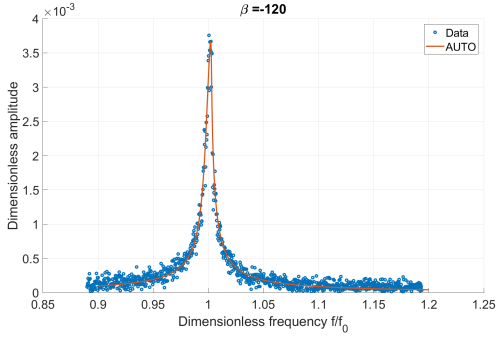

(f) $P_{DC,r} = 1.05$ mW.

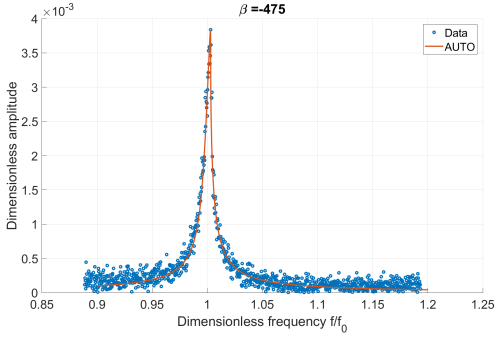

(g) $P_{DC,r} = 0.83$ mW.

FIG. S3: Linear fits. To actuate the membrane, a modulated blue laser was used with power $P_b = -20$ dBm. Each curve corresponds to a different red laser power $P_{DC,r}$

.

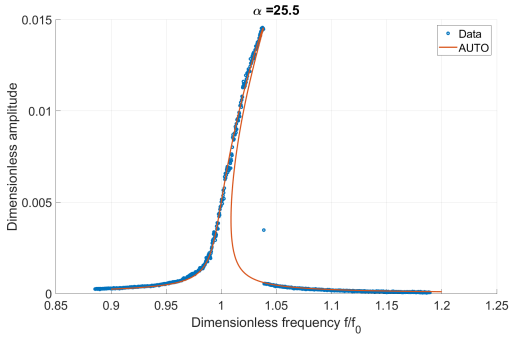

(a) $P_{DC,r} = 3.32$ mW.

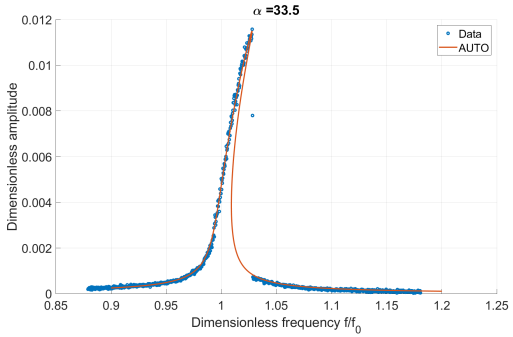

(b) $P_{DC,r} = 2.64$ mW.

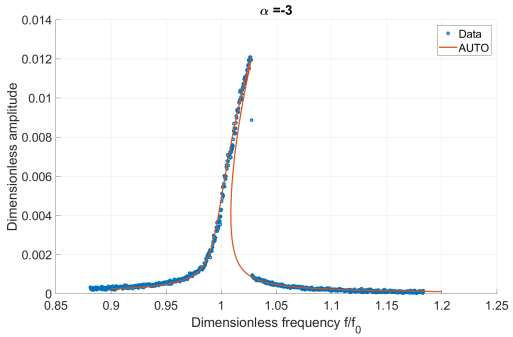

(c) $P_{DC,r} = 2.09$ mW.

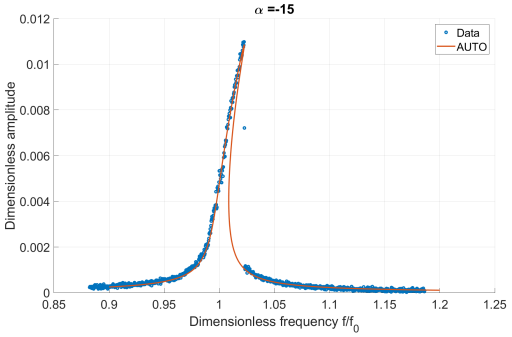

(d) $P_{DC,r} = 1.66$ mW.

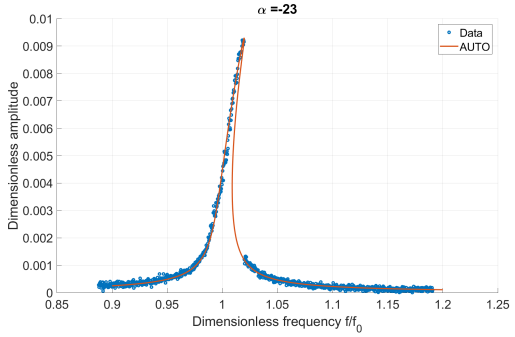

(e) $P_{DC,r} = 1.32$ mW.

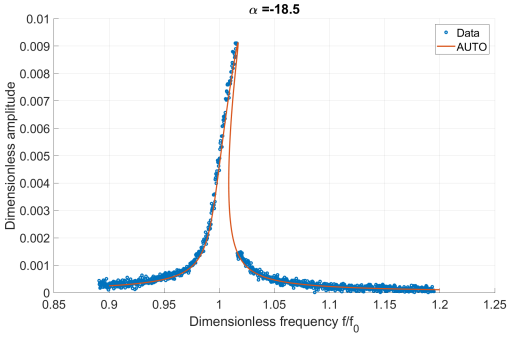

(f) $P_{DC,r} = 1.05$ mW.

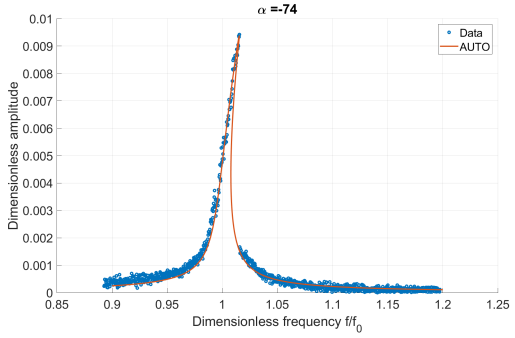

(g) $P_{DC,r} = 0.83$ mW.

FIG. S4: Linear fits. To actuate the membrane, a modulated blue laser was used with power $P_b = -10$ dBm. Each curve corresponds to a different red laser power $P_{DC,r}$

.

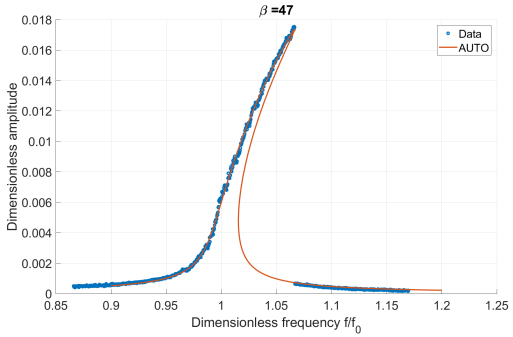

(a) $P_{DC,r} = 3.32$ mW.

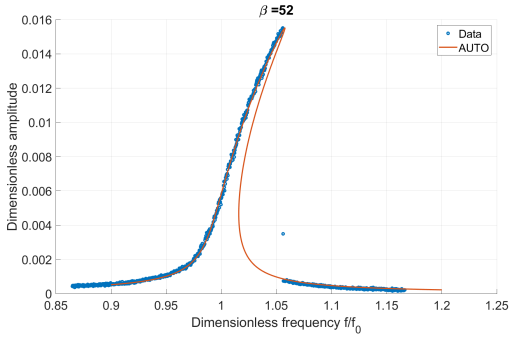

(b) $P_{DC,r} = 2.64$ mW.

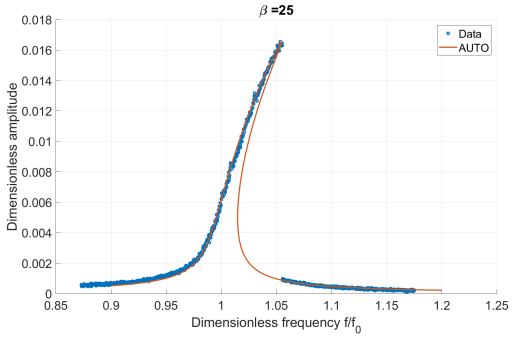

(c) $P_{DC,r} = 2.09$ mW.

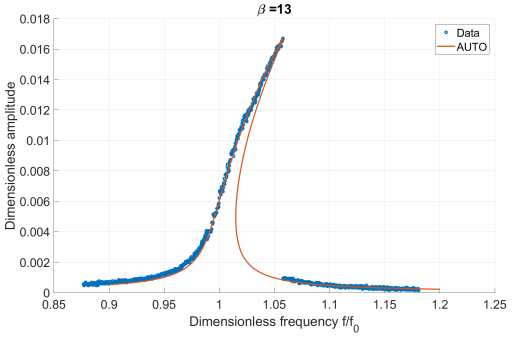

(d) $P_{DC,r} = 1.66$ mW.

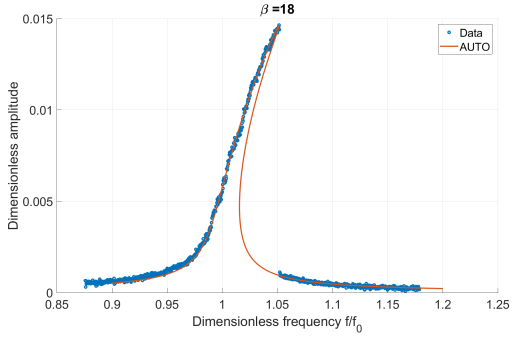

(e) $P_{DC,r} = 1.32$ mW.

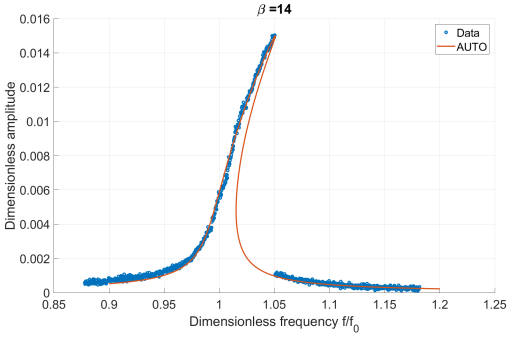

(f) $P_{DC,r} = 1.05$ mW.

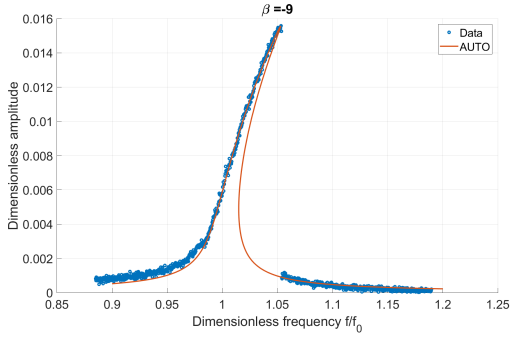

(g) $P_{DC,r} = 0.83$ mW.

FIG. S5: Linear fits. To actuate the membrane, a modulated blue laser was used with power $P_b = 0$ dBm. Each curve corresponds to a different red laser power $P_{DC,r}$

.

III. OPTICAL MODEL

One way to obtain an expression for the position dependent absorbed power is to use the matrix method in thin film spectroscopy [2]. The mathematical derivation follows here, and will be applied to graphene optomechanics. Throughout the text, s-polarization of the monochromatic light is used.

Consider the multilayer system in Fig. S6, where the incident medium is a vacuum, followed by a layer of graphene, another vacuum, and a silicon substrate. The refractive indices of the media are all different, depending on the z-coordinate of the system: $n = n(z)$ and $\varepsilon = \varepsilon(z)$, where ε is the dielectric function. The first step is to find expressions for the field amplitudes of the electromagnetic wave. The electromagnetic wave is expressed as:

$$\boldsymbol{E} = \boldsymbol{E}_0 e^{-i\omega t}, \qquad \boldsymbol{H} = \boldsymbol{H}_0 e^{-i\omega t} \tag{S-8}$$

In case of s-polarization, the electric and magnetic fields have the following components:

$$\boldsymbol{E} = \begin{pmatrix} 0 \\ E_y \\ 0 \end{pmatrix}, \qquad \boldsymbol{H} = \begin{pmatrix} H_x \\ 0 \\ H_z \end{pmatrix} \tag{S-9}$$

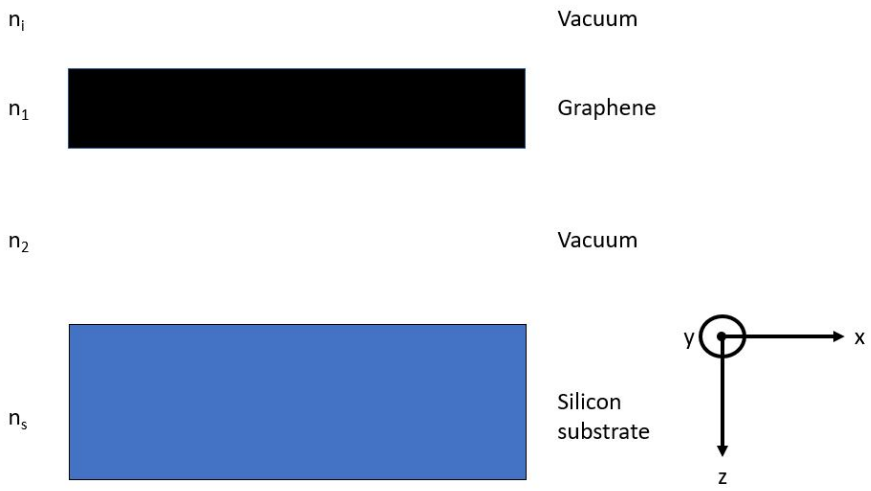

FIG. S6: Multilayer system of a graphene, vacuum and silicon layer. The refractive index of each layer is indicated by n.

From Maxwell's equations:

$$\nabla \times \boldsymbol{E} = -\frac{\partial \boldsymbol{B}}{\partial t}, \qquad \nabla \times \boldsymbol{H} = \frac{\partial \boldsymbol{D}}{\partial t} \tag{S-10}$$

with $\boldsymbol{B} = \mu_0 \boldsymbol{H}$ and $\boldsymbol{D} = \epsilon\epsilon_0 \boldsymbol{E} + \boldsymbol{P}$, where μ_0 is the permeability of free space ϵ_0 is the permittivity of free space and $\boldsymbol{P}$ is the polarization. This leads to the following system of equations:

$$i\omega\mu_0 H_x = -\frac{\partial}{\partial z} E_y \tag{S-11}$$

$$i\omega\mu_0 H_y = 0 \tag{S-12}$$

$$i\omega\mu_0 H_z = \frac{\partial}{\partial x} E_y \tag{S-13}$$

$$\frac{\partial}{\partial z} H_x - \frac{\partial}{\partial x} H_z = -i\omega\epsilon\epsilon_0 E_y \tag{S-14}$$

$$\frac{\partial}{\partial y} H_z = 0 \tag{S-15}$$

$$\frac{\partial}{\partial y} H_x = 0 \tag{S-16}$$

$$\tag{S-17}$$

Differentiating Eqs. (S-11) and (S-13) again with respect to their spatial coordinates and summing up gives the following wave equation:

$$\frac{\partial^2}{\partial x^2} E_y + \frac{\partial^2}{\partial z^2} E_y = -\frac{\omega^2}{c^2} \varepsilon(z) E_y \tag{S-18}$$

Applying separation of variables $E_y = X(x)U(z)$ yields:

$$\frac{1}{X}\frac{d^2X}{dx^2} = -\frac{1}{U}\frac{d^2U}{dz^2} - \frac{\omega^2}{c^2}\varepsilon(z) = C \tag{S-19}$$

C is a constant. For convenience, it will be rewritten as $C = -k_0^2\eta^2$, with $k_0 = \frac{\omega}{c} = \frac{2\pi}{\lambda_0}$. From Eq. S-19, $X = e^{ik_0\eta x}$. Using Maxwell's equations again, the expressions for the components of the electric and magnetic field become:

$$E_y = U(z)e^{ik_0\eta x} \tag{S-20}$$

$$H_x = -V(z)e^{ik_0\eta x} \tag{S-21}$$

$$H_z = -W(z)e^{ik_0\eta x} \tag{S-22}$$

This results in the following system of equations for the field amplitudes:

$$\frac{dU}{dz} = i\omega\mu_0 V(z) \tag{S-23}$$

$$\frac{dV}{dz} = i\omega\varepsilon_0(\varepsilon - \eta^2)U(z) \tag{S-24}$$

$$\mu_0 W(z) + \frac{\eta}{c}U(z) = 0 \tag{S-25}$$

Introducing different functions for U and V:

$$u = U, \qquad v = \sqrt{\frac{\mu_0}{\varepsilon_0}}V \tag{S-26}$$

This results in:

$$\frac{du}{dz} = ik_0 v \tag{S-27}$$

$$\frac{dv}{dz} = ik_0(\varepsilon - \eta^2)u \tag{S-28}$$

Note that functions u and v have the same dimension. Now let $z = 0$ be the position of the interface between the vacuum and the graphene layer. Then, $u(0) = u_0$ and $v(0) = v_0$. Assuming the solution $u_1(z), v_1(z)$ (corresponding to the boundary conditions $u_1(0) = 1$ and $v_1(0) = 0$) and $u_2(z), v_2(z)$ (corresponding to the boundary conditions $u_2(0) = 0$ and $v_2(0) = 1$), it follows that [2]:

$$\begin{pmatrix} u_0 \\ v_0 \end{pmatrix} = \boldsymbol{M} \begin{pmatrix} u(z) \\ v(z) \end{pmatrix} = \begin{pmatrix} v_2(z) & -u_2(z) \\ v_1(z) & v_2(z) \end{pmatrix} \begin{pmatrix} u(z) \\ v(z) \end{pmatrix} \tag{S-29}$$

For the case where the incident electromagnetic wave hits the interface perpendicular, the solutions for u_1, v_1, u_2 and v_2 that are consistent with equations S-27 and S-28 are:

$$u_1 = \cos(k_0\hat{n}z) \tag{S-30}$$

$$v_1 = i\hat{n}\sin(k_0\hat{n}z) \tag{S-31}$$

$$u_2 = \frac{i}{\hat{n}}\sin(k_0\hat{n}z) \tag{S-32}$$

$$v_2 = \cos(k_0\hat{n}z) \tag{S-33}$$

Therefore, the $\boldsymbol{M}$-matrix, or characteristic matrix, of a single film is:

$$\boldsymbol{M} = \begin{pmatrix} \cos(2\pi\hat{n}z/\lambda_0) & -\frac{i}{\hat{n}}\sin(2\pi\hat{n}z/\lambda_0) \\ -i\hat{n}\cos(2\pi\hat{n}z/\lambda_0) & \cos(2\pi\hat{n}z/\lambda_0) \end{pmatrix} \tag{S-34}$$

For a film stack, where each individual film i has a thickness $d_i = z_{i+1} - z_i$, we can write:

$$\begin{pmatrix} u_0 \\ v_0 \end{pmatrix} = \boldsymbol{M}_1(d_1)\boldsymbol{M}_2(d_2)...\boldsymbol{M}_N(d_N) \begin{pmatrix} u(z_N) \\ v(z_N) \end{pmatrix} \tag{S-35}$$

So the characteristic matrix of a film stack with N film layers is:

$$\boldsymbol{M} = \begin{pmatrix} m_{11} & m_{12} \\ m_{21} & m_{22} \end{pmatrix} = \prod_{i=1}^{N} \boldsymbol{M}_i(d_i) \tag{S-36}$$

The four elements of the $\boldsymbol{M}$-matrix are related to the reflectance and transmittance coefficients in the following way:

$$r = \frac{(m_{11} + m_{12}n_s)n_0 - (m_{21} + m_{22}n_s)}{(m_{11} + m_{12}n_s)n_0 + (m_{21} + m_{22}n_s)} \tag{S-37}$$

$$t = \frac{2n_0}{(m_{11} + m_{12}n_s)n_0 + (m_{21} + m_{22}n_s)} \tag{S-38}$$

where n_s and n_0 are the refractive indices of the substrate (silicon) and incident medium respectively. The intensity coefficients can be calculated now as well:

$$R = |r|^2 \tag{S-39}$$

$$T = \frac{\mathbb{R}(n_s)}{\mathbb{R}(n_0)}|t|^2 \tag{S-40}$$

The absorption would then be equal to:

$$A = 1 - R - T \tag{S-41}$$

By varying the thickness of the second film (the vacuum between the graphene and substrate), a position-dependent energy absorption is obtained. For monochromatic light with $\lambda = 633\,\text{nm}$ and

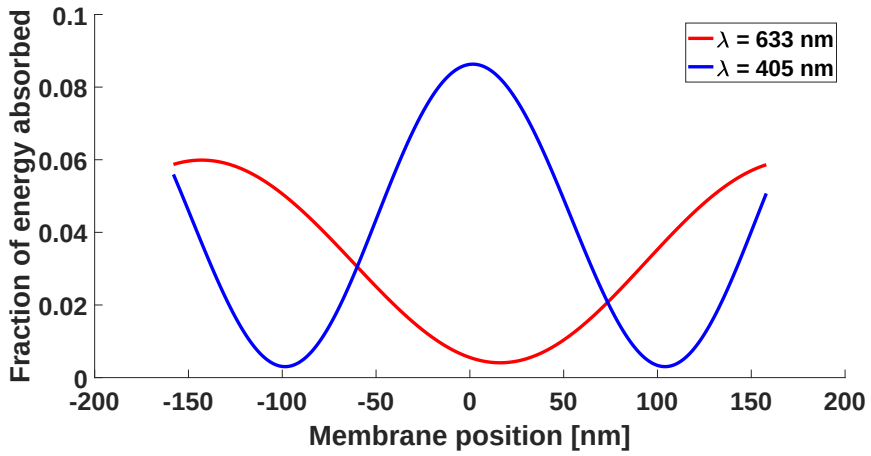

FIG. S7: Position dependent absorption.

$\lambda = 404\,\text{nm}$, the result is shown in figure S7. Finally, the absorbed power is simply:

$$P_{abs} = AP_i \tag{S-42}$$

A simple harmonic function is fitted to these curves. For the red and blue laser light:

$$P_{abs,r}(x) = P_{i,r}\left[\alpha_r + \beta_r \sin(\gamma_r(x+g) + \phi_r)\right] \tag{S-43}$$

$$P_{abs,b}(x) = P_{i,b}\left[\alpha_b + \beta_b \sin(\gamma_b(x+g) + \phi_b)\right] \tag{S-44}$$

Note that the intensity of the blue laser is actually modulated. Using the appropriate trigonometric relations, the equations become:

$$P_{abs,r}(x) = P_{i,r}\left[\alpha_r + \beta_r \left(\sin(\gamma_r g + \phi_r)\cos(\gamma_r x) + \cos(\gamma_r g + \phi_r)\sin(\gamma_r x)\right)\right] \tag{S-45}$$

$$P_{abs,b}(x) = P_{i,b}\left[\alpha_b + \beta_b \left(\sin(\gamma_b g + \phi_b)\cos(\gamma_b x) + \cos(\gamma_b g + \phi_b)\sin(\gamma_b x)\right)\right] \tag{S-46}$$

IV. OPTOTHERMAL FORCE

A. Equation of Motion

In this section, the influence of the optical field on the coefficients of the equation of motion of the optothermally excited graphene membrane is investigated. It is known that for these kind of systems, the optical field influences the effective linear damping and stiffness [3]. Here, the analysis is extended to include the influence on nonlinear terms as well. The derivation given here closely follows Ref. [4].

In general, a membrane vibrating in the nonlinear regime can be described by the Duffing equation. A Duffing term αx^3, which could already be seen in Eq. (S-1), describes a nonlinear restoring force that is responsible for the hardening behavior observed in these systems. To account for nonlinear dissipation, an amplitude-dependent dissipation term $\nu x^2 \dot{x}$ is added to the equation. Therefore, the equation of motion is:

$$m\ddot{x} + \Gamma\dot{x} + kx + \alpha x^3 + \nu x^2\dot{x} = F \tag{S-47}$$

where m is the mass, Γ is the linear damping coefficient, k is the linear stiffness coefficient, and F is a force acting on the membrane. The left hand side of Eq. S-47 represents the mechanical part of the system. Any effects from the optical field come from F and will be on the right hand side. In this case, F has two contributions:

$$F = F_{th}(t) + F_{ph}(x(t)) \tag{S-48}$$

where $F_{th}(t)$ is an effective thermal force due to Brownian motion and $F_{ph}(x(t))$ is a position dependent photon-induced force such as radiation pressure or a photothermal force. In the remainder, $F_{th}(t)$ is assumed to contribute much less than $F_{ph}(x(t))$ and will be neglected. In general, photon-induced forces show a delay with respect to a change in the position of the membrane. From here on, radiation pressure is assumed to be negligible compared to the photothermal force, which has shown to be true for similar systems [5].

Furthermore, it is assumed that the photothermal force responds to a discrete change in membrane position $x_n - x_{n-1}$ with a single time delay τ. This is depicted in Fig. S8. For N position

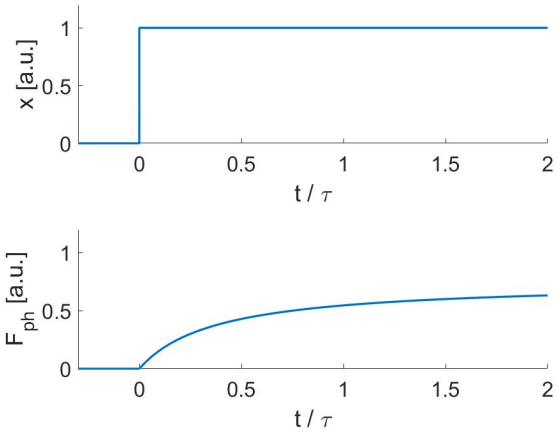

FIG. S8: Modeling of the photon-induced force. The force can not follow the change in position of the membrane instantly, but is delayed by a finite time.

steps, F can be modeled as a summation of all force increments:

$$F(x_N(t)) = F_{ph}(x_0) + \sum_{n=1}^{N} h(t-t_n)\left[F_{ph}(x_n) - F_{ph}(x_{n-1})\right] \tag{S-49}$$

where $h(t)$ is a function that describes the time delay. In the limit where $x_n - x_{n-1} \to 0$, this can be rewritten as a continuous integral in time:

$$F(x(t)) = F_{ph}(x_0) + \int_0^t \frac{dF_{ph}(x(t'))}{dt'} h(t-t')dt' \tag{S-50}$$

$$= F_{ph}(x_0) + \int_0^t \left(\frac{\partial F_{ph}}{\partial x}\frac{\partial x}{\partial t'}\right) h(t-t')dt' \tag{S-51}$$

Eq. S-51 holds if the photothermal force has no explicit time dependence, i.e. when the there is constant illumination. For weakly modulated illumination, the photon-induced force is written as:

$$F(x(t),t) = (1+\epsilon(t))F_{ph}(x(t)) \tag{S-52}$$

Consequently, the continuous time integral describing the photothermal force in this case becomes:

$$F(x(t),t) = F_{ph}(x_0) + \int_0^t \frac{dF_{ph}(x(t'),t')}{dt'} h(t-t')dt' \tag{S-53}$$

$$= F_{ph}(x_0) + \int_0^t \left(\frac{\partial F_{ph}}{\partial x}\frac{\partial x}{\partial t'} + \frac{\partial F_{ph}}{\partial t'}\right) h(t-t')dt' \tag{S-54}$$

The term $F_{ph}(x_0)$ has no time dependence, and will eventually only lead to a static deflection.

From here on, this term will be dropped. For the system under consideration, a red laser with constant illumination was used for readout of the motion, and an intensity modulated blue laser was used for actuation. Therefore, the total photon-induced force is:

$$F(x,t) = \int_0^t \left(\frac{\partial F_{ph,r}}{\partial x}\frac{\partial x}{\partial t'} + \frac{\partial F_{ph,b}}{\partial x}\frac{\partial x}{\partial t'} + \frac{\partial F_{ph,b}}{\partial t'} \right) h(t-t')dt' \tag{S-55}$$

$$= \int_0^t \left(\frac{\partial F_{ph,r}}{\partial x}\frac{\partial x}{\partial t'} \right) h(t-t')dt' + \int_0^t \left(\frac{\partial F_{ph,b}}{\partial x}\frac{\partial x}{\partial t'} \right) h(t-t')dt' + \int_0^t \left(\frac{\partial F_{ph,b}}{\partial t'} \right) h(t-t')dt' \tag{S-56}$$

where the subscripts $_r$ and $_b$ refer to the red and blue laser, respectively.

It is assumed that the photothermal force is proportional to the power absorbed by the graphene layer:

$$F_{ph} = BP_{ph} \tag{S-57}$$

where B is the proportionality constant and P_{ph} is the (position-dependent) absorbed power. The proportionality constant depends on the thermal expansion, thermal conductivity and the geometry of the resonator, and can be determined experimentally. This will be done in the next section.

The expressions for $P_{ph,r}$ and $P_{ph,b}$ that were obtained earlier in equations S-45 and S-46 can now be used. These expressions are approximated by Taylor expansions. The maximum amplitude of the graphene nanodrum in the experiments was 25 nm. To accurately describe the position dependent absorption, it is sufficient to include terms up to the third order. See Fig. S9. This results in:

$$P_{ph,r} \approx P_{i,r}\left[\alpha_r + \beta_r\left(\sin(\gamma_r g + \phi_r)(1 - \frac{\gamma_r^2 x^2}{2}) + \cos(\gamma_r g + \phi_r)(\gamma_r x - \frac{\gamma_r^3 x^3}{6})\right)\right] \tag{S-58}$$

$$P_{ph,b} \approx P_{i,b}\left[\alpha_b + \beta_b\left(\sin(\gamma_b g + \phi_b)(1 - \frac{\gamma_b^2 x^2}{2}) + \cos(\gamma_b g + \phi_b)(\gamma_b x - \frac{\gamma_b^3 x^3}{6})\right)\right] \tag{S-59}$$

where P_i is the incident power, g is the cavity gap size and α, β, γ and ϕ are the optical fit parameters. Taking the derivative with respect to x gives:

$$\frac{\partial P_{ph,r}}{\partial x} = P_{i,r}\beta_r\left(\sin(\gamma_r g + \phi_r)(-\gamma_r^2 x) + \cos(\gamma_r g + \phi_r)(\gamma_r - \frac{\gamma_r^3 x^2}{2})\right) \tag{S-60}$$

$$\frac{\partial P_{ph,b}}{\partial x} = P_{i,b}\beta_b\left(\sin(\gamma_b g + \phi_b)(-\gamma_b^2 x) + \cos(\gamma_b g + \phi_b)(\gamma_b - \frac{\gamma_b^3 x^2}{2})\right) \tag{S-61}$$

Eqs. S-57 to S-61 can now be filled in into Eq. S-56. The result is converted to the frequency

domain by using the convolution property of the Laplace transform, which says that:

$$\mathcal{L}\left\{\int_0^t f(t')g(t-t')dt'\right\} = f_\omega g_\omega \tag{S-62}$$

where we used $s = i\omega$, and the subscript $_\omega$ refers to the frequency domain. Applying this property to Eq. S-56 results in:

$$\begin{aligned} -m\omega^2 x_\omega^2 + i\omega\Gamma x_\omega + i\omega\nu x_\omega^3 + kx_\omega + \alpha x_\omega^3 = \\ B\left[i\omega x_\omega \left(\frac{\partial P_r}{\partial x}\right)_\omega + i\omega P_{b,\omega} + i\omega x_\omega \left(\frac{\partial P_b}{\partial x}\right)_\omega\right] h_\omega \end{aligned} \tag{S-63}$$

The time delay function is still unknown. By assuming that, after the graphene membrane changes to a new equilibrium position, the response of the heat flow due to the absorbed laser power is exponential in nature, $h(t)$ and its transform h_ω are:

$$h(t) = 1 - e^{-t/\tau} \tag{S-64}$$

$$h_\omega = \frac{1}{i\omega(1+i\omega\tau)} = \frac{1-i\omega\tau}{i\omega(1+\omega^2\tau^2)} \tag{S-65}$$

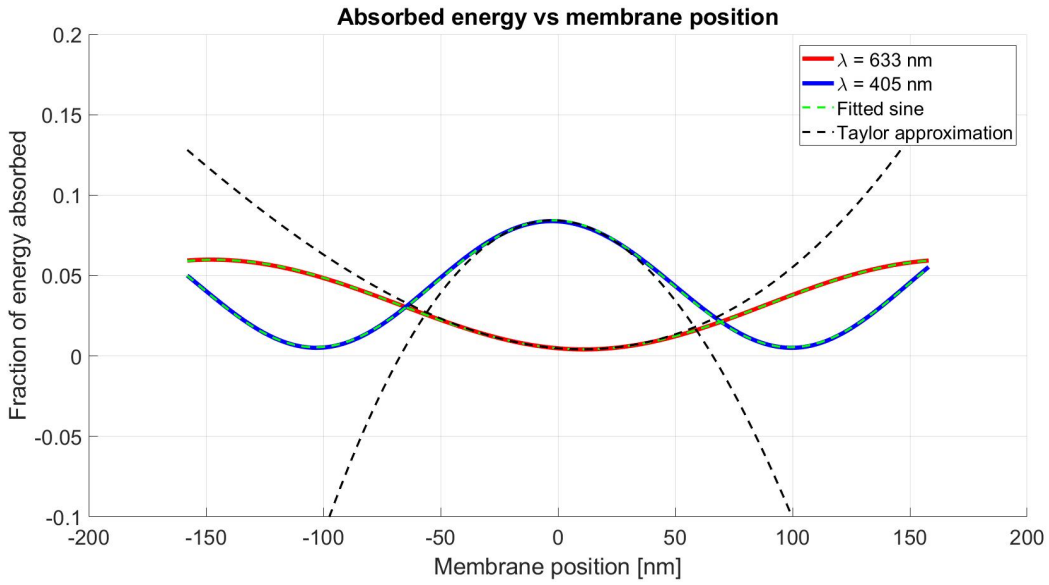

FIG. S9: Fraction of absorbed power versus membrane position. The functions are approximated with Taylor series. Terms up to the third order are retained.

where τ is the thermal time constant. Using this expression for the delay function leads to:

$$\begin{aligned} -m\omega^2 x_\omega^2 + i\omega\Gamma x_\omega + i\omega\nu x_\omega^3 + k x_\omega + \alpha x_\omega^3 = \\ B\left[x_\omega\left(\frac{\partial P_r}{\partial x}\right)_\omega + P_{b,\omega} + x_\omega\left(\frac{\partial P_b}{\partial x}\right)_\omega\right]\frac{1-i\omega\tau}{1+\omega^2\tau^2} \end{aligned} \tag{S-66}$$

By grouping Eq. S-66 in terms of ω, the equation of motion including optomechanically induced terms is obtained. The modulated part of the blue laser, $\epsilon(t)F_{ph,b}(x(t))$, only has a small effect on the coefficients of the equation of motion compared to the other terms. By neglecting the terms coming from the modulated part, the following final expression is obtained:

$$-m\omega^2 x_\omega^2 + i\omega\Gamma_{\text{eff}} x_\omega + i\omega\eta_{\text{eff}} x_\omega^2 + i\omega\nu_{\text{eff}} x_\omega^3 + k_{\text{eff}} x_\omega + \mu_{\text{eff}} x_\omega^2 + \alpha_{\text{eff}} x_\omega^3 = f \tag{S-67}$$

with:

$$\Gamma_{\text{eff}} = \Gamma + \frac{BP_{i,r}\tau\beta_r\gamma_r\cos(\gamma_r g+\phi_r)}{1+\omega^2\tau^2} + \frac{BP_{i,b}\tau\beta_b\gamma_b\cos(\gamma_b g+\phi_b)}{1+\omega^2\tau^2} \tag{S-68}$$

$$\eta_{\text{eff}} = -\frac{BP_{i,r}\tau\beta_r\gamma_r^2\sin(\gamma_r g+\phi_r)}{1+\omega^2\tau^2} - \frac{BP_{i,b}\tau\beta_b\gamma_b^2\sin(\gamma_b g+\phi_b)}{1+\omega^2\tau^2} \tag{S-69}$$

$$\nu_{\text{eff}} = \nu - \frac{BP_{i,r}\tau\beta_r\gamma_r^3\cos(\gamma_r g+\phi_r)}{2(1+\omega^2\tau^2)} - \frac{BP_{i,b}\tau\beta_b\gamma_b^3\cos(\gamma_b g+\phi_b)}{2(1+\omega^2\tau^2)} \tag{S-70}$$

$$k_{\text{eff}} = k - \frac{BP_{i,r}\beta_r\gamma_r\cos(\gamma_r g+\phi_r)}{1+\omega^2\tau^2} - \frac{BP_{i,b}\beta_b\gamma_b\cos(\gamma_b g+\phi_b)}{1+\omega^2\tau^2} \tag{S-71}$$

$$\mu_{\text{eff}} = \frac{BP_{i,r}\beta_r\gamma_r^2\sin(\gamma_r g+\phi_r)}{1+\omega^2\tau^2} + \frac{BP_{i,b}\beta_b\gamma_b^2\sin(\gamma_b g+\phi_b)}{1+\omega^2\tau^2} \tag{S-72}$$

$$\alpha_{\text{eff}} = \alpha + \frac{BP_{i,r}\beta_r\gamma_r^3\cos(\gamma_r g+\phi_r)}{2(1+\omega^2\tau^2)} + \frac{BP_{i,b}\beta_b\gamma_b^3\cos(\gamma_b g+\phi_b)}{2(1+\omega^2\tau^2)} \tag{S-73}$$

$$f = \frac{BP_{i,b}(1-i\omega\tau)\left(\alpha_b+\beta_b\sin(\gamma_b g+\phi_b)\right)}{1+\omega^2\tau^2} \tag{S-74}$$

B. Determining the proportionality constant B

The proportionality constant B relates the absorbed power to the photothermal force. As such, it is a function of the thermal expansion, thermal conductivity and geometry of the membrane. The value of B can be determined in the following way. From the linear response, the Q-factor can be extracted by fitting a Lorentzian to the linear curves. In this regime, the blue laser power is very low, and the contribution of the blue laser to the optomechanically induced damping is

negligible. The Q-factor is related to Γ_{eff} through:

$$\Gamma_{\text{eff}} = m\omega_n Q^{-1} \tag{S-75}$$

where ω_n is the natural frequency of the fundamental mode of the membrane. Fig. S10 shows the measured values for Γ_{eff} for different values of the red laser power. A linear line with gradient ∇l is fitted to the data. It then follows from Eq. S-68 that:

$$B = \frac{(1+\omega_n^2\tau^2)\nabla l}{\tau\beta_r\gamma_r\cos(\gamma_r g + \phi_r)} \tag{S-76}$$

where $\omega \approx \omega_n$ was used. For $g = 300\,\text{nm}$, it was found that $B \approx 7.0\times10^{-6}\ \text{Nm}^2\text{W}^{-1}$.

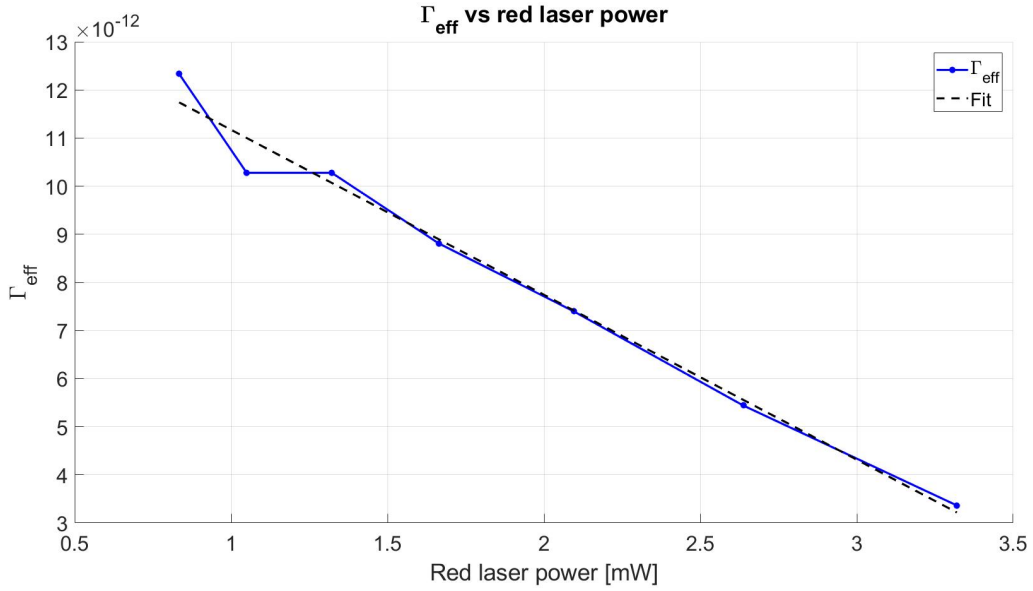

FIG. S10: The effective values of the linear dissipation rate Γ, which were obtained at low actuation, versus red laser powers. B is determined by fitting a straight line through these values.

[1] A. R. Champneys, Y. A. Kuznetsov, T. F. Fairgrieve, and X. Wang, "AUTO97: Contiunation and bifurcation software for ordinary differential equations," (1998).

[2] O. Stenzel, *The Physics of Thin Film Optical Spectra* (Springer, 2005).

[3] R. A. Barton, I. R. Storch, V. P. Adiga, R. Sakakibara, B. R. Cipriany, B. Ilic, S. P. Wang, P. Ong, P. L. McEuen, J. M. Parpia, and H. G. Craighead, Nano Letters **12**, 4681 (2012).

[4] C. Metzger, I. Favero, A. Ortlieb, and K. Karrai, Physical Review B **78** (2008), 10.1103/PhysRevB.78.035309.

[5] A. Chandrashekar, *Optothermally excited parametric resonance in monolayer graphene nanodrum resonators*, Ph.D. thesis, Delft University of Technology (2017).

Appendix A

Nonlinear parameter identification

In Chapter 2, a nonlinear parameter identification method based on the harmonic balance method was introduced. A detailed explanation on how this method is implemented in this thesis is given below. The method closely follows Ref. [79].

The membrane is modeled as a single degree-of-freedom system. The equation of motion is given by equation 2-42:

$$m_{\text{eff}}\ddot{\tilde{x}} + c_1\dot{\tilde{x}} + k_1\tilde{x} + k_3\tilde{x}^3 + c_3\tilde{x}^2\dot{\tilde{x}} = \xi F\cos(\omega\tilde{t}) \tag{A-1}$$

This equation can be rewritten by normalizing the motion amplitude with the membrane's thickness h, and scaling time $\tilde{t}$ with the excitation frequency ω:

$$x = \tilde{x}/h \tag{A-2}$$

$$t = \omega\tilde{t} \tag{A-3}$$

$$\frac{d}{d\tilde{t}} = \frac{d}{dt}\frac{dt}{d\tilde{t}} = \omega\frac{d}{dt} \tag{A-4}$$

Applying these relations results in the following expression:

$$m_{\text{eff}}\omega^2 h\ddot{x} + c_1\omega h\dot{x} + k_1 hx + k_3 h^3x^3 + c_3\omega h^3x^2\dot{x} = \xi F\cos(t) \tag{A-5}$$

Finally, by expressing the natural frequency as $\omega_n = \sqrt{k/m}$, introducing a dimensionless frequency $\Omega = \omega/\omega_n$ and dividing all terms in the equation with $m_{\text{eff}}\omega_n^2 h$, the equation of motion becomes:

$$\Omega^2\ddot{x} + Q^{-1}\Omega\dot{x} + x + \alpha x^3 + \nu\Omega x^2\dot{x} = \lambda\cos(t) \tag{A-6}$$

with:

$$Q^{-1} = \frac{c_1}{m_{\text{eff}}\omega_n} \tag{A-7}$$

$$\alpha = \frac{k_3 h^2}{m_{\text{eff}}\omega_n^2} \tag{A-8}$$

$$\nu = \frac{c_3 h^2}{m_{\text{eff}}\omega_n} \tag{A-9}$$

$$\lambda = \frac{\xi F}{m_{\text{eff}}\omega_n^2 h} \tag{A-10}$$

Note that at this point, there are 2 unknowns, which are the non-dimensional parameters α and ν. The goal is to to identify these parameters using the frequency response curves. In order to do so, the steady state solution of equation A-6 can be found by assuming the following solution for $x(t)$:

$$x = A\cos(t-\phi) = A\sin(\phi)\sin(t) + A\cos(\phi)\cos(t) = x_1\sin(t) + x_2\cos(t) \tag{A-11}$$

From this solution, expressions for $\dot{x}$, $\ddot{x}$, x^2 and $x^2\dot{x}$ are derived. These can be filled in into equation A-1. Using the appropriate trigonometric identities, and grouping the $\sin(t)$ and $\cos(t)$ terms, the following two equations are obtained:

$$x_1(1-\Omega^2) - Q^{-1}\Omega x_2 + \frac{3}{4}\alpha x_1 A^2 - \frac{1}{4}\nu\Omega x_2 A^2 = 0 \tag{A-12}$$

$$x_2(1-\Omega^2) + Q^{-1}\Omega x_1 + \frac{3}{4}\alpha x_2 A^2 + \frac{1}{4}\nu\Omega x_1 A^2 = \lambda \tag{A-13}$$

where $A = \sqrt{x_1^2 + x_2^2}$.

Note that equations A-12 and A-13 are obtained for any frequency step Ω_i. So if Ω consists of $\bar{M}$ frequency steps, the total number of equations obtained is $2\bar{M}$. Therefore, the system of equations can be written as:

$$\mathbf{A}\mathbf{x} = \mathbf{b} \tag{A-14}$$

where $\mathbf{A}$ is a $2\bar{M}\times 2$ matrix, $\mathbf{x}$ is a 2×1 vector that contains the parameters to be identified, and $\mathbf{b}$ is a $2\bar{M}\times 1$ vector with known terms. Explicitly, the linear system looks like:

$$\begin{pmatrix} \vdots & \vdots \\ 3/4\, x_1 A^2 & -1/4\,\Omega_i x_2 A^2 \\ 3/4\, x_2 A^2 & 1/4\,\Omega_i x_1 A^2 \\ \vdots & \vdots \end{pmatrix} \begin{pmatrix} \alpha \\ \\ \nu \end{pmatrix} = \begin{pmatrix} \vdots \\ -x_1(1-\Omega_i^2) + Q^{-1}\Omega_i x_2 \\ -x_2(1-\Omega_i^2) - Q^{-1}\Omega_i x_1 + \lambda \\ \vdots \end{pmatrix} \tag{A-15}$$

For any number of frequency steps where $\bar{M} > 1$, there are more equations than unknowns. The system of equations is then overdetermined. For this system, the least squares method will give the best approximate solution. For a certain solution $\mathbf{x}$, the least squares error is minimized when

$$\mathbf{x} = \left(\mathbf{A}^{\mathrm{T}}\mathbf{A}\right)^{-1}\left(\mathbf{A}^{\mathrm{T}}\mathbf{b}\right) \tag{A-16}$$

In practice, it was found that, although the obtained value for α seemed to be very reasonable, the value for ν could sometimes be clearly incorrect. A solution to this problem is to force

the nonlinear damping term ν to be such that the the maximum amplitude as obtained from the frequency response function is the same as the maximum amplitude as obtained from the data. This will be shown below.

First, the Frequency Response Function (FRF) is derived. From equation A-12, x_1 can be expressed in terms of x_2 as:

$$x_1 = \frac{Q^{-1}\Omega + \frac{1}{4}\nu\Omega A^2}{(1-\Omega^2) + \frac{3}{4}\alpha A^2} x_2 \tag{A-17}$$

Filling in into equation A-13 gives:

$$x_2 \left[\left((1-\Omega^2) + \frac{3}{4}\alpha A^2 \right)^2 + \left(Q^{-1}\Omega + \frac{1}{4}\nu\Omega A^2 \right)^2 \right] = \lambda \left[\left(1-\Omega^2\right) + \frac{3}{4}\alpha A^2 \right] \tag{A-18}$$

Likewise, equation A-13 can be rewritten and filled in into equation A-12 to obtain:

$$x_1 \left[\left((1-\Omega^2) + \frac{3}{4}\alpha A^2 \right)^2 + \left(Q^{-1}\Omega + \frac{1}{4}\nu\Omega A^2 \right)^2 \right] = \lambda \left[Q^{-1}\Omega + \frac{1}{4}\nu\Omega A^2 \right] \tag{A-19}$$

Squaring equations A-18 and A-19 and summing up leads to the FRF of the system:

$$A^2 \left[\left((1-\Omega^2) + \frac{3}{4}\alpha A^2 \right)^2 + \left(Q^{-1}\Omega + \frac{1}{4}\nu\Omega A^2 \right)^2 \right] = \lambda^2 \tag{A-20}$$

Equation A-20 is an analytical approximation of the FRF based on the harmonic balance method. It should be able to describe the frequency response curves from the data, given the correct parameters. The backbone curve can be created by taking the derivative of the FRF with respect to the dimensionless frequency Ω:

$$\begin{aligned} \frac{d}{d\Omega}(\text{eq. A-20}) = {} & 2A\frac{dA}{d\Omega}\left[\left((1-\Omega^2) + \frac{3}{4}\alpha A^2 \right)^2 + \left(Q^{-1}\Omega + \frac{1}{4}\nu\Omega A^2 \right)^2 \right] \\ & + 2A^2 \left((1-\Omega^2) + \frac{3}{4}\alpha A^2 \right) \left(-2\Omega + \frac{3}{2}\alpha A \frac{dA}{d\Omega} \right) \\ & + 2A^2 \left(Q^{-1}\Omega + \frac{1}{4}\nu\Omega A^2 \right) \left(Q^{-1} + \frac{1}{4}\nu A^2 + \frac{1}{2}\nu\Omega A \frac{dA}{d\Omega} \right) = 0 \end{aligned} \tag{A-21}$$

Note that the amplitude A is a function of Ω, and $\frac{dA}{d\Omega} = 0$ when the maximum amplitude $A_{\max}$ is reached. The corresponding frequency is named $\Omega_{\max}$. Using this, and dividing the whole equation by $-4A_{\max}^2\Omega_{\max}$, the equation reduces to:

$$-\frac{1}{32}\nu^2 A_{\max}^4 - \frac{1}{4}\nu Q^{-1} - \frac{1}{2}Q^{-2} + (1-\Omega_{\max}^2) + \frac{3}{4}\alpha A_{\max}^2 = 0 \tag{A-22}$$

From equation A-22, the following expressions can be written:

$$(1-\Omega_{\max}^2) + \frac{3}{4}\alpha A_{\max}^2 = \frac{1}{32}\nu^2 A_{\max}^4 + \frac{1}{4}\nu Q^{-1} A_{\max}^2 + \frac{1}{2}Q^{-2} \tag{A-23}$$

$$\Omega_{\max}^2 = 1 + \frac{3}{4}\alpha A_{\max}^2 - \frac{1}{32}\nu^2 A_{\max}^4 - \frac{1}{4}\nu Q^{-1} A_{\max}^2 - \frac{1}{2}Q^{-2} \tag{A-24}$$

Filling these expressions in into the FRF equation A-20, a relation between ν and the maximum amplitude $A_{\max}$, Q, α and λ is obtained:

$$A_{\max}^2\left(\frac{1}{32}\nu^2A_{\max}^4+\frac{1}{4}\nu Q^{-1}A_{\max}^2+\frac{1}{2}Q^{-2}\right)^2+ A_{\max}^2\left(1+\frac{3}{4}\alpha A_{\max}^2-\frac{1}{32}\nu^2A_{\max}^4-\frac{1}{4}\nu Q^{-1}A_{\max}^2-\frac{1}{2}Q^{-2}\right)\left(Q^{-1}+\frac{1}{4}\nu A_{\max}^2\right)^2=\lambda^2 \tag{A-25}$$

Equation A-25 is a 4th order polynomial for ν as a function of $A_{\max}$, Q, α and λ:

$$\beta_1\nu^4+\beta_2\nu^3+\beta_3\nu^2+\beta_4\nu+\beta_5=0 \tag{A-26}$$

with

$$\beta_1=-\frac{A_{\max}^8}{1024} \tag{A-27}$$

$$\beta_2=-\frac{A_{\max}^6Q^{-1}}{64} \tag{A-28}$$

$$\beta_3=\frac{3A_{\max}^6\alpha}{64}+\frac{A_{\max}^4}{16}-\frac{3A_{\max}^4Q^{-2}}{32} \tag{A-29}$$

$$\beta_4=\frac{3A_{\max}^4Q^{-1}\alpha}{8}+\frac{A_{\max}^2Q^{-1}}{2}-\frac{2A_{\max}^2Q^{-3}}{8} \tag{A-30}$$

$$\beta_5=Q^{-2}-\frac{Q^{-4}}{4}+\frac{3A_{\max}^2Q^{-2}\alpha}{4}-\frac{\lambda^2}{A_{\max}^2} \tag{A-31}$$

Knowing all these parameters, equation A-26 can be solved for ν. It was found that one of the roots always corresponded to a reasonable value for ν.

Appendix B

Nonlinear fits of the electrostatically actuated graphene membrane

B-1 Fits for each curve individually

The fits that were obtained for each curve are shown below. Here, α and ν are different for each curve.

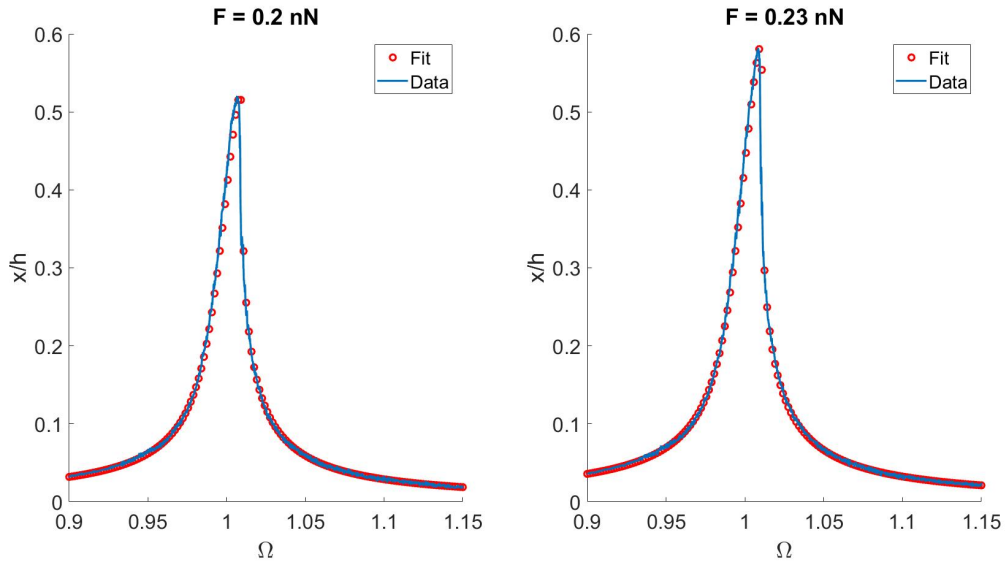

Figure B-1: Two nonlinear response curves and their fits. The drive forces belonging to these curves are $F = 0.20\,\mathrm{nN}$ and $F = 0.23\,\mathrm{nN}$.

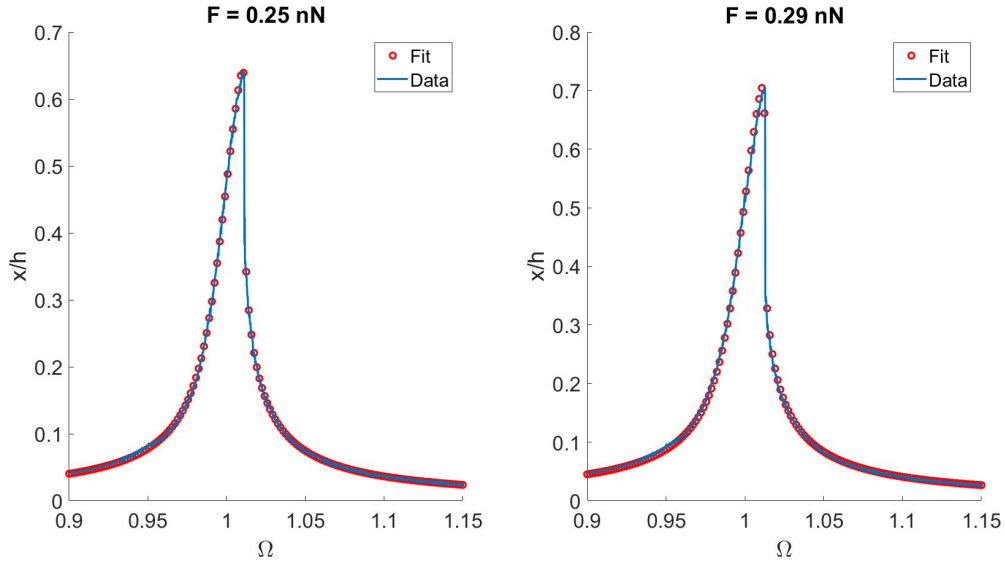

Figure B-2: Two nonlinear response curves and their fits. The drive forces belonging to these curves are $F = 0.25\,\mathrm{nN}$ and $F = 0.29\,\mathrm{nN}$.

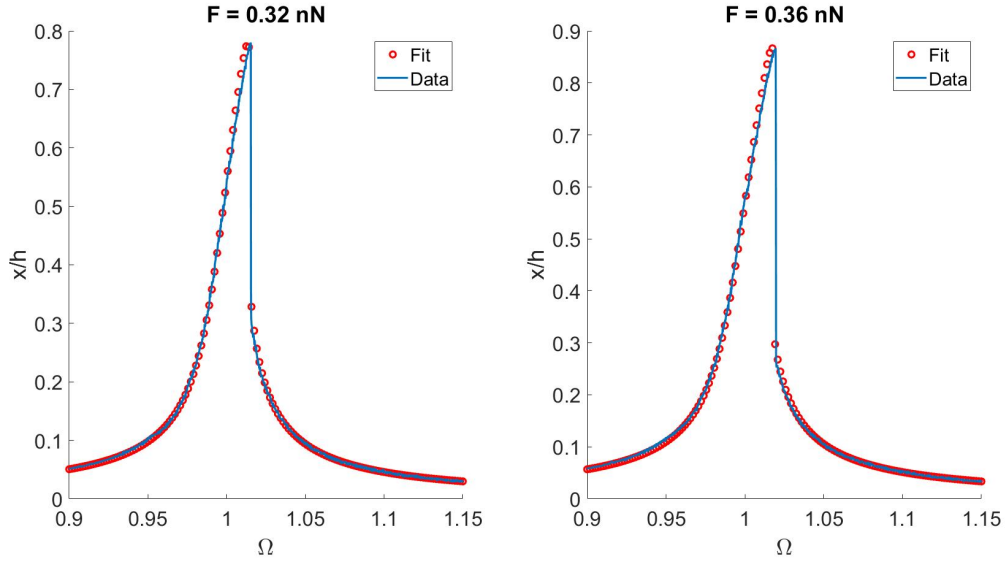

Figure B-3: Two nonlinear response curves and their fits. The drive forces belonging to these curves are $F = 0.32\,\mathrm{nN}$ and $F = 0.36\,\mathrm{nN}$.

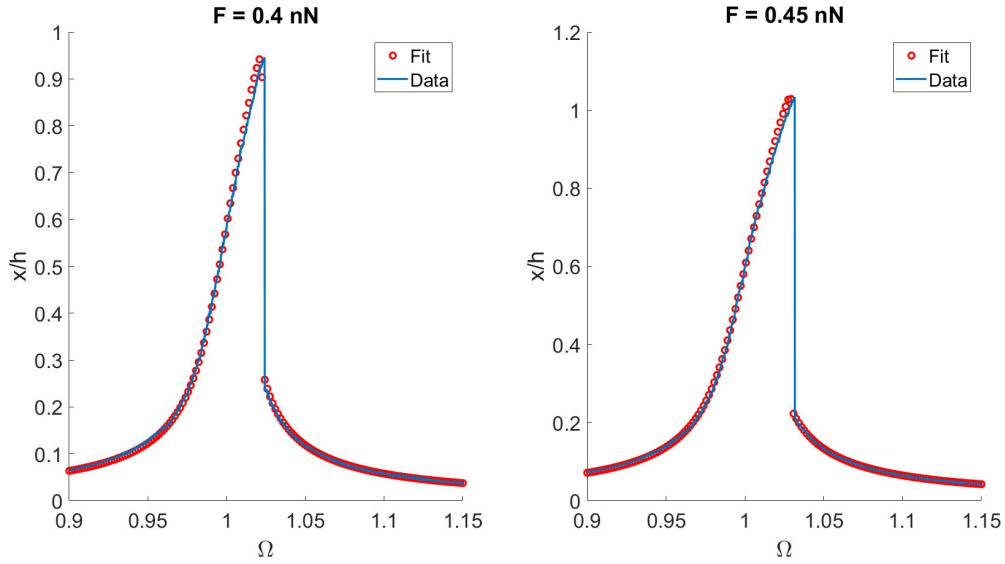

Figure B-4: Two nonlinear response curves and their fits. The drive forces belonging to these curves are $F = 0.40\,\mathrm{nN}$ and $F = 0.45\,\mathrm{nN}$.

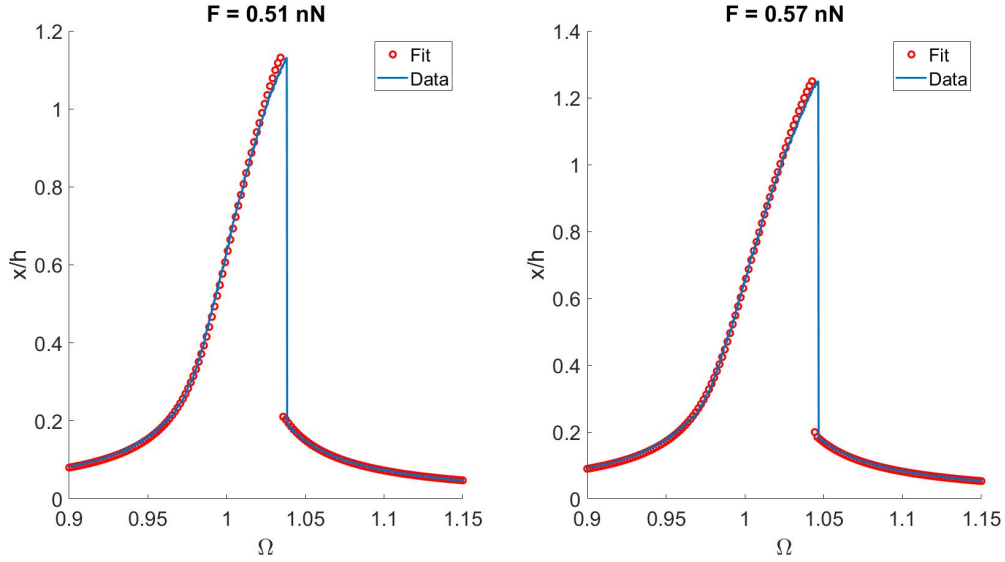

Figure B-5: Two nonlinear response curves and their fits. The drive forces belonging to these curves are $F = 0.51\,\mathrm{nN}$ and $F = 0.57\,\mathrm{nN}$.

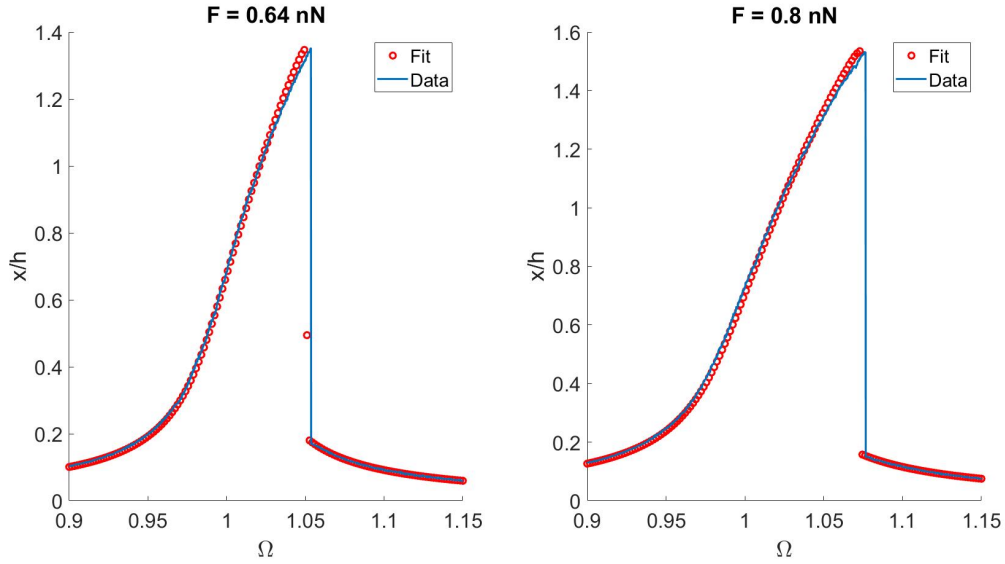

Figure B-6: Two nonlinear response curves and their fits. The drive forces belonging to these curves are $F = 0.64\,\mathrm{nN}$ and $F = 0.80\,\mathrm{nN}$.

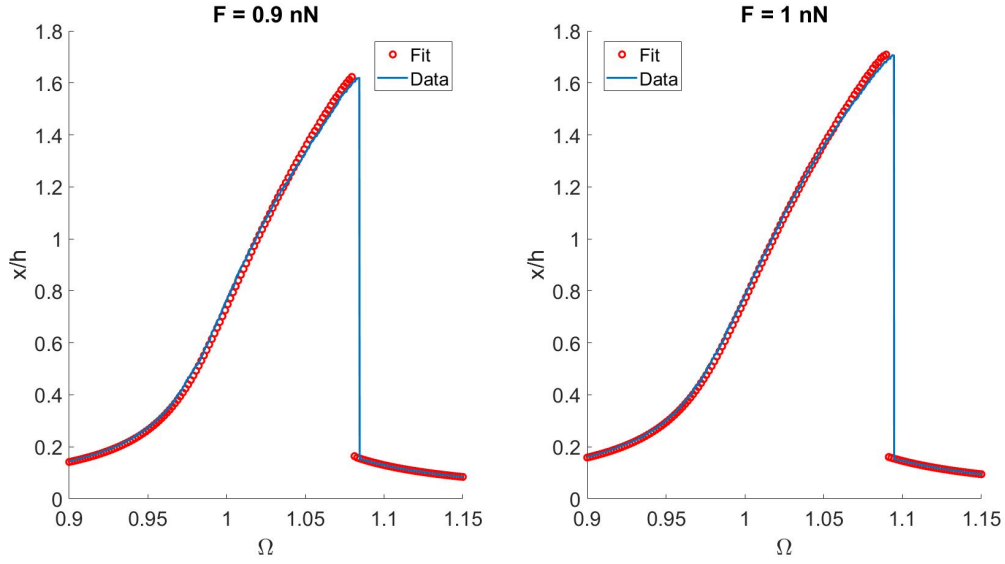

Figure B-7: Two nonlinear response curves and their fits. The drive forces belonging to these curves are $F = 0.90\,\mathrm{nN}$ and $F = 1.0\,\mathrm{nN}$.

B-2 Fits using averaged coefficients

The fits that were obtained for each curve are shown below. Here, an average value of α and ν was used to fit every curve with, corresponding to $E = 400.58\,\mathrm{GPa}$ and $\tau = 463.70\,\mathrm{ps}$.

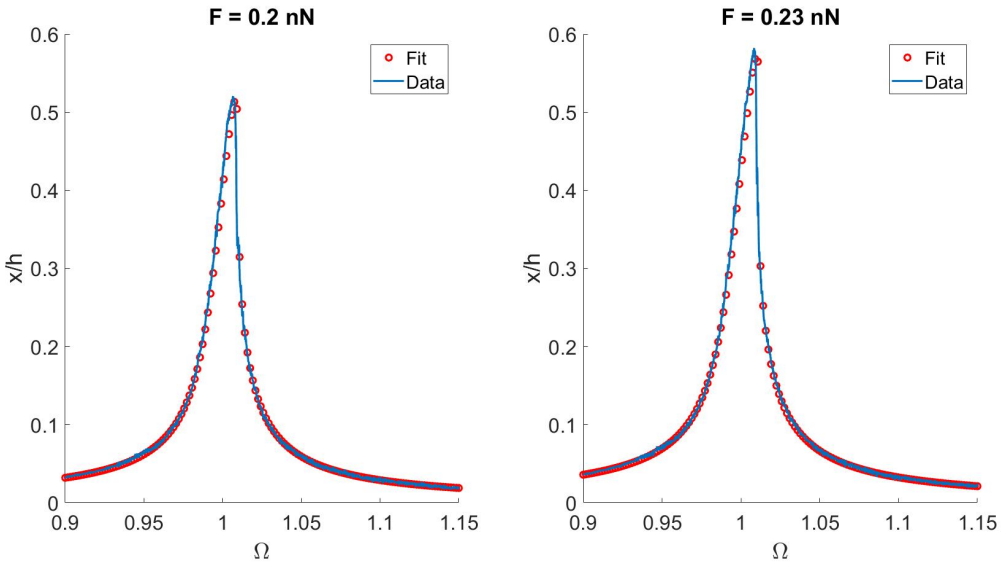

Figure B-8: Two nonlinear response curves and their fits. The drive forces belonging to these curves are $F = 0.20\,\mathrm{nN}$ and $F = 0.23\,\mathrm{nN}$.

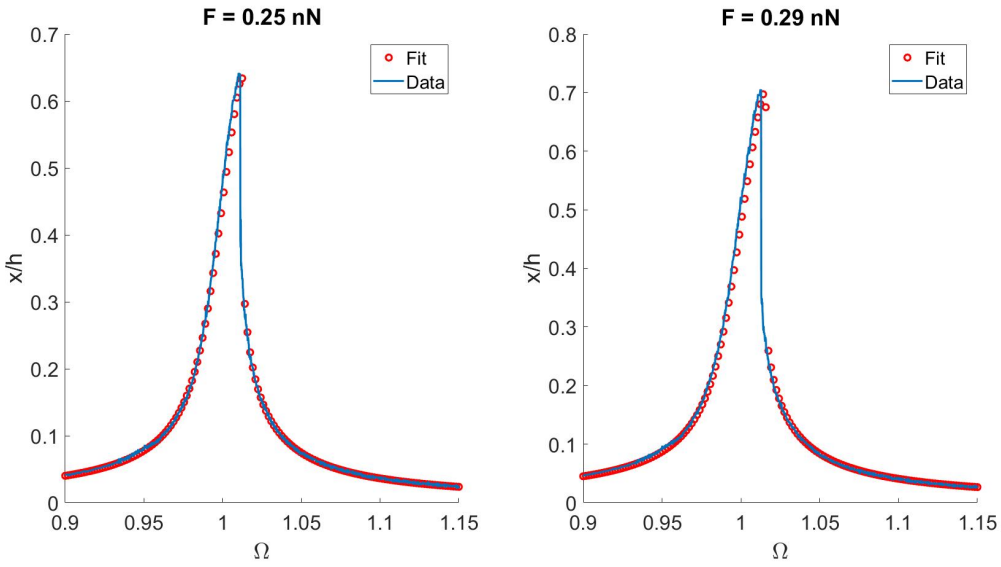

Figure B-9: Two nonlinear response curves and their fits. The drive forces belonging to these curves are $F = 0.25\,\mathrm{nN}$ and $F = 0.29\,\mathrm{nN}$.

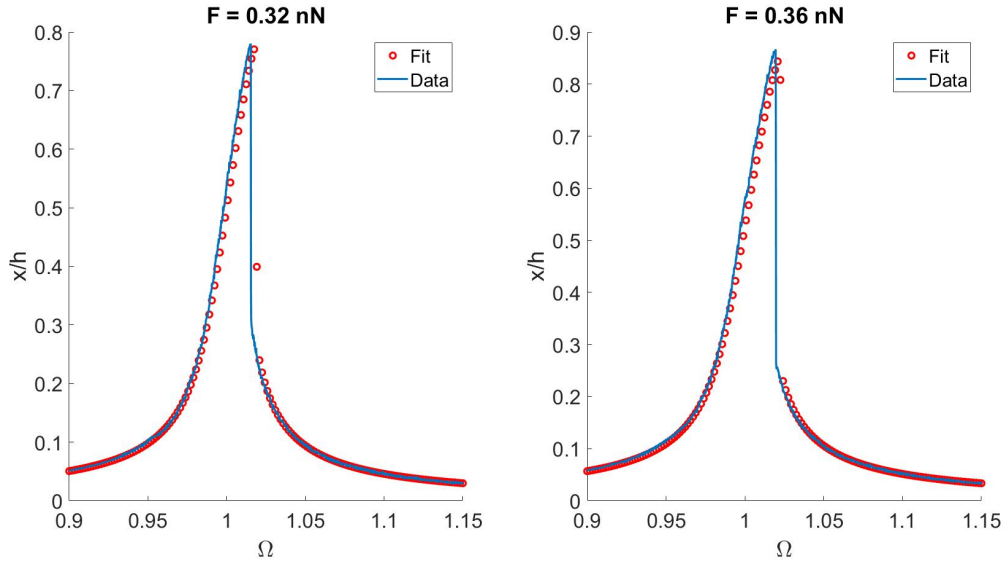

Figure B-10: Two nonlinear response curves and their fits. The drive forces belonging to these curves are $F = 0.32\,\mathrm{nN}$ and $F = 0.36\,\mathrm{nN}$.

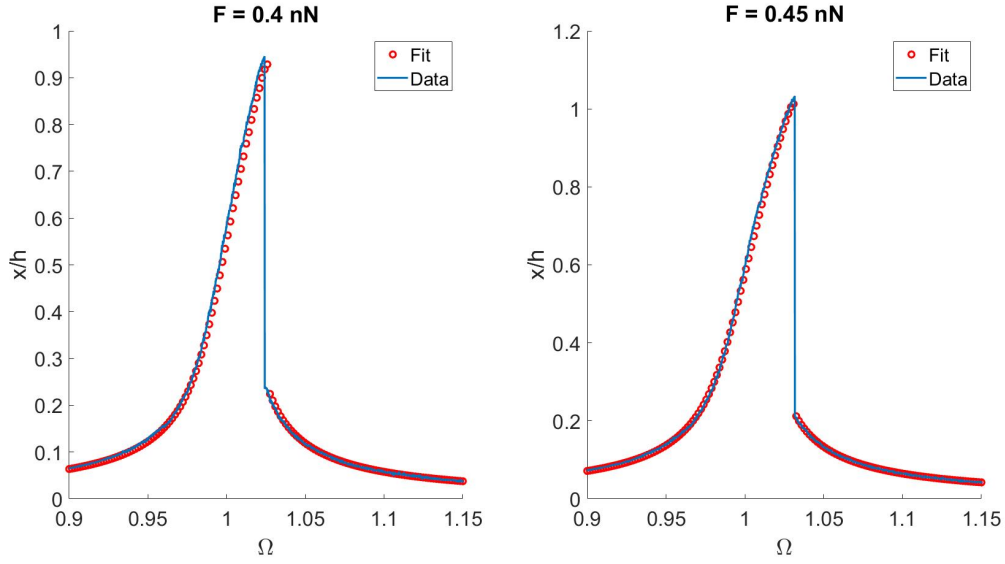

Figure B-11: Two nonlinear response curves and their fits. The drive forces belonging to these curves are $F = 0.40\,\mathrm{nN}$ and $F = 0.45\,\mathrm{nN}$.

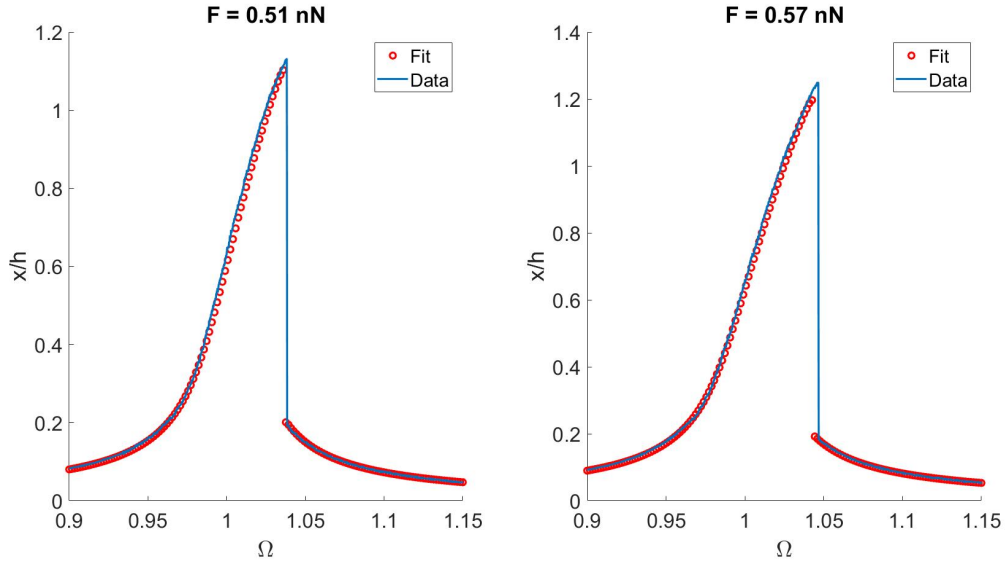

Figure B-12: Two nonlinear response curves and their fits. The drive forces belonging to these curves are $F = 0.51\,\mathrm{nN}$ and $F = 0.57\,\mathrm{nN}$.

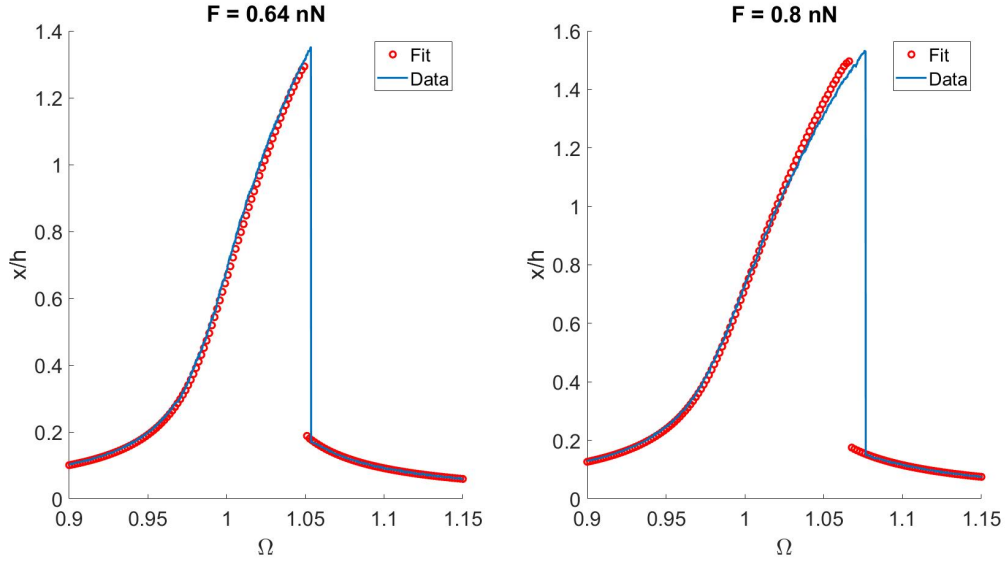

Figure B-13: Two nonlinear response curves and their fits. The drive forces belonging to these curves are $F = 0.64\,\mathrm{nN}$ and $F = 0.80\,\mathrm{nN}$.

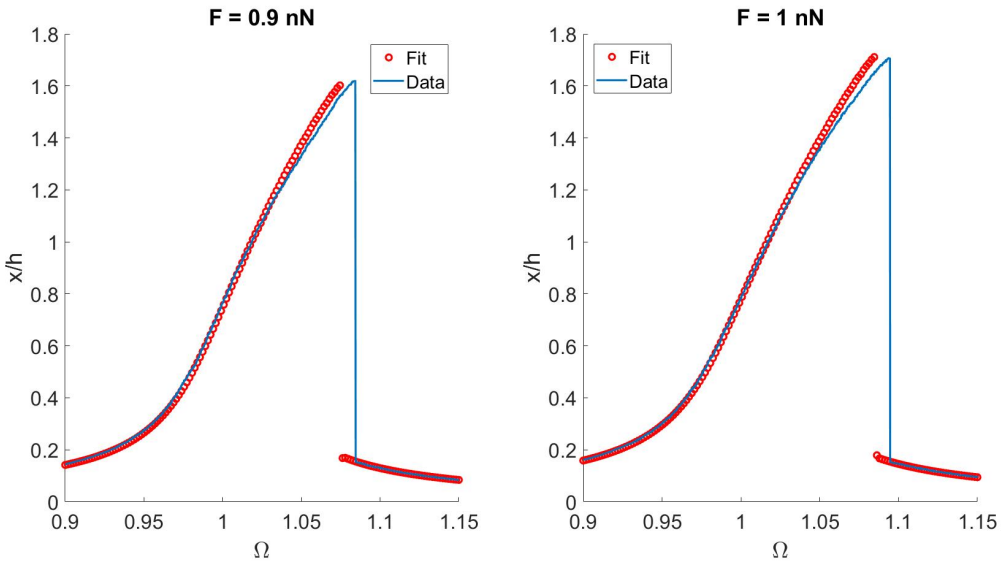

Figure B-14: Two nonlinear response curves and their fits. The drive forces belonging to these curves are $F = 0.90\,\mathrm{nN}$ and $F = 1.0\,\mathrm{nN}$.

Bibliography

[1] A. Bryan, A. Goranov, A. Amon, and S. Manalis, "Measuring single cell mass, volume and density with dual suspended microchannel resonators," *Lab Chip*, vol. 14, pp. 569–576, 2014.

[2] J. Lee, W. Shen, K. Payer, T. Burg, and S. Manalis, "Toward attogram mass measurements in solution with suspended nanochannel resonators," *Nano Letters*, vol. 10, no. 7, pp. 2537–2542, 2010.

[3] M. F. Bocko, R. Onofrio, and I. Padova, "On the measurement of a weak classical force coupled to a harmonic oscillator : experimental progress," *Reviews of Modern Physics*, vol. 68, no. 755, 1996.

[4] W. E. Newell, "Miniaturization of Tuning Forks," *Science*, vol. 161, no. 3848, pp. 1320–1326, 1968.

[5] S. S. Verbridge and H. G. Craighead, "A megahertz nanomechanical resonator with room temperature quality factor over a million," *Applied Physics Letters*, vol. 92, no. 013112, 2008.

[6] C. Zener, *Elasticity and Anelasticity of Metals*. Chicago: University of Chicago Press, 1948.

[7] R. Lakes, *Viscoelastic Materials*. New York: Camebridge University Press, 2009.

[8] D. A. Czaplewski, J. P. Sullivan, T. A. Friedmann, D. W. Carr, B. E. N. Keeler, J. R. Wendt, D. A. Czaplewski, J. P. Sullivan, T. A. Friedmann, D. W. Carr, and B. E. N. Keeler, "Mechanical dissipation in tetrahedral amorphous carbon," *Journal of Applied Physics*, vol. 97, no. 023517, 2005.

[9] A. Nowick and B. Berry, *Anelastic Relaxation in Crystalline Solids*. New York: Academic, 1972.

[10] I. Golovin, M. Blanter, H. Neuhäuser, and H.-R. Sinning, *Internal Friction in Metallic Materials*, vol. 90. Springer, 2007.

[11] S. Schmid, L. G. Villanueva, and M. L. Roukes, *Fundamentals of Nanomechanical Resonators*. Springer, 2016.

[12] K. Y. Yasumura, T. D. Stowe, E. M. Chow, T. Pfafman, T. W. Kenny, B. C. Stipe, and D. Rugar, "Quality factors in micron- and submicron-thick cantilevers," *Journal of Microelectromechanical Systems*, vol. 9, no. 1, pp. 117–125, 2000.

[13] J. Yang, T. Ono, and M. Esashi, "Energy dissipation in submicrometer thick single-crystal silicon cantilevers," *Journal of Microelectromechanical Systems*, vol. 11, no. 6, pp. 775–783, 2002.

[14] L. G. Villanueva and S. Schmid, "Evidence of surface loss as ubiquitous limiting damping mechanism in SiN micro- and nanomechanical resonators," *Physical Review Letters*, vol. 113, no. 22, 2014.

[15] Y. Tao, J. M. Boss, B. A. Moores, and C. L. Degen, "Single-crystal diamond nanomechanical resonators with quality factors exceeding one million," *Nature Communications*, vol. 5, pp. 1–8, 2014.

[16] C. Zener, "Internal friction in solids I. Theory of internal friction in reeds," *Physical Review*, vol. 52, pp. 230–235, 1937.

[17] C. Zener, "Internal friction in solids II. General theory of thermoelastic internal friction," *Physical Review*, vol. 53, pp. 90–99, 1938.

[18] T. Roszhart, "The effect of thermoelastic internal friction on the Q of micromachined silicon resonators," 1990.

[19] R. Abdolvand, H. Johari, G. K. Ho, A. Erbil, and F. Ayazi, "Quality Factor in Trench-Refilled Polysilicon Beam Resonators," *Journal of Microelectromechanical Systems*, vol. 15, no. 3, pp. 471–478, 2006.

[20] R. Lifshitz and M. L. Roukes, "Thermoelastic damping in micro- and nanomechanical systems," *Physical Review B*, vol. 61, no. 8, pp. 5600–5609, 2000.

[21] Y. Sun and M. Saka, "Thermoelastic damping in micro-scale circular plate resonators," *Journal of Sound and Vibration*, vol. 329, no. 3, pp. 328–337, 2010.

[22] S. Prabhakar and S. Vengallatore, "Theory of thermoelastic damping in micromechanical resonators with two-dimensional heat conduction," *Journal of Microelectromechanical Systems*, vol. 17, no. 2, pp. 494–502, 2008.

[23] A. A. Kiselev and G. J. Iafrate, "Phonon dynamics and phonon assisted losses in Euler-Bernoulli nanobeams," *Physical Review B - Condensed Matter and Materials Physics*, vol. 77, no. 20, pp. 1–9, 2008.

[24] K. Kunal and N. R. Aluru, "Akhiezer damping in nanostructures," *Physical Review B - Condensed Matter and Materials Physics*, vol. 84, no. 24, pp. 1–8, 2011.

[25] A. Akhiezer, "On the Absorption of Sound in Solids," *Journal of Physics*, vol. 1, no. 1, pp. 277–287, 1939.

[26] H. Bömmel and K. Dransfeld, "Excitation and attenuation of hypersonic waves in quartz," *Physical Review*, vol. 117, no. 5, pp. 1245–1252, 1960.

[27] T. Woodruff and H. Ehrenreich, "Absorption of sound in insulators," *Physical Review*, vol. 123, no. 5, pp. 1553–1559, 1961.

[28] V. Braginsky, V. Mitrofanov, and V. Panov, *Systems with Small Dissipation*. Chicago: University of Chicago Press, 1985.

[29] S. S. Iyer and R. N. Candler, "Mode- and Direction-Dependent Mechanical Energy Dissipation in Single-Crystal Resonators due to Anharmonic Phonon-Phonon Scattering," *Physical Review Applied*, vol. 5, no. 3, pp. 1–9, 2016.

[30] A. N. Cleland, *Foundations of nanomechanics: from solid-state theory to device applications*. New York: Springer, 2003.

[31] V. J. Gokhale and M. Rais-Zadeh, "Phonon-electron interactions in piezoelectric semiconductor bulk acoustic wave resonators," *Scientific Reports*, vol. 4, 2014.

[32] P. Esquinazi, *Tunneling Systems in Amorphous and Crystalline Solids*. Springer Verlag, 1998.

[33] P. Mohanty, D. A. Harrington, K. L. Ekinci, Y. T. Yang, M. J. Murphy, and M. L. Roukes, "Intrinsic dissipation in high-frequency micromechanical resonators," *Physical Review B - Condensed Matter and Materials Physics*, vol. 66, no. 8, pp. 854161–8541615, 2002.

[34] G. Zolfagharkhani, A. Gaidarzhy, S.-b. Shim, R. L. Badzey, and P. Mohanty, "Quantum friction in nanomechanical oscillators at millikelvin temperatures," *Physical Review B*, vol. 72, no. 224101, pp. 1–5, 2005.

[35] M. Bao, *Analysis and design principles of MEMS devices*. 2005.

[36] S. Schmid, B. Malm, and A. Boisen, "Quality factor improvement of silicon nitride micro string resonators," *Proceedings of the IEEE International Conference on Micro Electro Mechanical Systems (MEMS)*, pp. 481–484, 2011.

[37] O. Svitelskiy, V. Sauer, N. Liu, K. M. Cheng, E. Finley, M. R. Freeman, and W. K. Hiebert, "Pressurized fluid damping of nanoelectromechanical systems," *Physical Review Letters*, vol. 103, no. 24, pp. 1–4, 2009.

[38] A. K. Pandey, R. Pratap, and F. S. Chau, "Effect of pressure on fluid damping in MEMS torsional resonators with flow ranging from continuum to molecular regime," *Experimental Mechanics*, vol. 48, no. 1, pp. 91–106, 2008.

[39] J. E. Sader, "Frequency response of cantilever beams immersed in viscous fluids with applications to the AFM," *Journal of Applied Physics*, vol. 84, no. 1, pp. 64–76, 1998.

[40] C. P. Green and J. E. Sader, "Torsional frequency response of cantilever beams immersed in viscous fluids with applications to the atomic force microscope," *Journal of Applied Physics*, vol. 92, no. 10, pp. 6262–6274, 2002.

[41] C. Van Eysden and J. Sader, "Frequency response of cantilever beams immersed in viscous fluids with applications to the atomic force microscope: Arbitrary mode order," *Journal of Applied Physics*, vol. 101, no. 4, p. 044908, 2007.

[42] J. W. Chon, P. Mulvaney, and J. E. Sader, "Experimental validation of theoretical models for the frequency response of atomic force microscope cantilever beams immersed in fluids," *Journal of Applied Physics*, vol. 87, no. 8, pp. 3978–3988, 2000.

[43] M. Ghatkesar, T. Braun, V. Barwich, J. Ramseyer, C. Gerber, M. Hegner, and H. Lang, "Resonating modes of vibrating microcantilevers in liquid," *Applied Physics Letters*, vol. 92, no. 4, pp. 2006–2009, 2008.

[44] E. Uzunlar, B. Beykal, K. Ehrlich, D. Sanli, A. Jonáš, B. E. Alaca, A. Kiraz, H. Urey, and C. Erkey, "Frequency response of microcantilevers immersed in gaseous, liquid, and supercritical carbon dioxide," *Journal of Supercritical Fluids*, vol. 81, pp. 254–264, 2013.

[45] T. P. Burg, M. Godin, S. M. Knudsen, W. Shen, G. Carlson, J. S. Foster, K. Babcock, and S. R. Manalis, "Weighing of biomolecules, single cells and single nanoparticles in fluid," *Nature*, vol. 446, no. 7139, pp. 1066–1069, 2007.

[46] T. P. Burg, J. E. Sader, and S. R. Manalis, "Nonmonotonic energy dissipation in microfluidic resonators," *Physical Review Letters*, vol. 102, no. 22, 2009.

[47] J. E. Sader, T. P. Burg, and S. R. Manalis, *Energy dissipation in microfluidic beam resonators*, vol. 650. 2010.

[48] J. E. Sader, T. P. Burg, and S. R. Manalis, "Energy dissipation in microfluidic beam resonators," *Journal of Fluid Mechanics*, vol. 650, pp. 215–250, 2010.

[49] M. Bao, H. Yang, H. Yin, and Y. Sun, "Energy transfer model for squeeze-film air damping in low vacuum," *Journal of Micromechanics and Microengineering*, vol. 12, no. 3, pp. 341–346, 2002.

[50] P. Li and R. Hu, "On the air damping of flexible microbeam in free space at the free-molecule regime," *Microfluidics and Nanofluidics*, vol. 3, no. 6, pp. 715–721, 2007.

[51] M. Bao and H. Yang, "Squeeze film air damping in MEMS," *Sensors and Actuators, A: Physical*, vol. 136, no. 1, pp. 3–27, 2007.

[52] D. M. Photiadis and J. A. Judge, "Attachment losses of high Q oscillators," *Applied Physics Letters*, vol. 85, no. 3, pp. 482–484, 2004.

[53] J. A. Judge, D. M. Photiadis, J. F. Vignola, B. H. Houston, and J. Jarzynski, "Attachment loss of micromechanical and nanomechanical resonators in the limits of thick and thin support structures," *Journal of Applied Physics*, vol. 101, no. 1, 2007.

[54] T. Natsuki, J.-X. Shi, and Q.-Q. Ni, "Vibration analysis of nanomechanical mass sensor using double-layered graphene sheets resonators," *Journal of Applied Physics*, vol. 114, no. 094307, 2014.

[55] R. J. Dolleman, D. Davidovikj, S. J. Cartamil-bueno, H. S. J. V. D. Zant, and P. G. Steeneken, "Graphene Squeeze-Film Pressure Sensors," *Nano Letters*, vol. 16, no. 1, pp. 568–571, 2016.

[56] R. J. Dolleman, S. J. Cartamil-bueno, H. S. J. V. D. Zant, and P. G. Steeneken, "Graphene gas osmometers," *2D Materials*, vol. 4, no. 011002, 2017.

[57] J. S. Bunch, A. M. Van Der Zande, S. S. Verbridge, I. W. Frank, D. M. Tanenbaum, J. M. Parpia, H. G. Craighead, and P. L. McEuen, "Electromechanical resonators from graphene sheets," *Science*, vol. 315, no. 5811, pp. 490–493, 2007.

[58] B. Witkamp, M. Poot, and H. S. J. Van Der Zant, "Bending-mode vibration of a suspended nanotube resonator," *Nano Letters*, vol. 6, no. 12, pp. 2904–2908, 2006.

[59] D. Garcia-Sanchez, A. San Paulo, M. J. Esplandiu, F. Perez-Murano, L. Forró, A. Aguasca, and A. Bachtold, "Mechanical detection of carbon nanotube resonator vibrations," *Physical Review Letters*, vol. 99, no. 8, pp. 1–4, 2007.

[60] C. Seoánez, F. Guinea, and A. H. Castro Neto, "Dissipation in graphene and nanotube resonators," *Physical Review B - Condensed Matter and Materials Physics*, vol. 76, no. 12, pp. 1–8, 2007.

[61] C. Seoanez, *Dissipation in finite systems: Semiconductor NEMS, graphene NEMS, and metallic nanoparticles*. PhD thesis, Universidad Autónoma de Madrid, 2007.

[62] M. Will, M. Hamer, M. Müller, A. Noury, P. Weber, A. Bachtold, R. V. Gorbachev, C. Stampfer, and J. Güttinger, "High Quality Factor Graphene-Based Two-Dimensional Heterostructure Mechanical Resonator," *Nano Letters*, vol. 17, no. 10, pp. 5950–5955, 2017.

[63] A. M. Van Der Zande, R. A. Barton, J. S. Alden, C. S. Ruiz-Vargas, W. S. Whitney, P. H. Pham, J. Park, J. M. Parpia, H. G. Craighead, and P. L. McEuen, "Large-scale arrays of single-layer graphene resonators," *Nano Letters*, vol. 10, no. 12, pp. 4869–4873, 2010.

[64] S. Y. Kim and H. S. Park, "Multilayer friction and attachment effects on energy dissipation in graphene nanoresonators," *Applied Physics Letters*, vol. 94, no. 10, pp. 2007–2010, 2009.

[65] D. Davidovikj, F. Alijani, S. J. Cartamil-Bueno, H. S. J. van der Zant, M. Amabili, and P. G. Steeneken, "Nonlinear dynamic characterization of two-dimensional materials," *Nature Communications*, vol. 8, no. 1, p. 1253, 2017.

[66] S. Zaitsev, O. Shtempluck, E. Buks, and O. Gottlieb, "Nonlinear damping in a micromechanical oscillator," *Nonlinear Dynamics*, vol. 67, no. 1, pp. 859–883, 2012.

[67] R. Lifshitz and M. C. Cross, "Nonlinear Dynamics of Nanomechanical and Micromechanical Resonators," *Review of nonlinear dynamics and complexity (Wiley)*, pp. 1–45, 2008.

[68] M. Imboden, O. A. Williams, and P. Mohanty, "Observation of Nonlinear Dissipation in Piezoresistive Diamond Nanomechanical Resonators by Heterodyne Down-Mixing," *Nano Letters*, vol. 13, pp. 4014–4019, 2013.

[69] A. Eichler, J. Moser, J. Chaste, M. Zdrojek, I. Wilson-Rae, and A. Bachtold, "Nonlinear damping in mechanical resonators made from carbon nanotubes and graphene," *Nature Nanotechnology*, vol. 6, no. 6, pp. 339–342, 2011.

[70] A. Croy, D. Midtvedt, A. Isacsson, and J. M. Kinaret, "Nonlinear damping in graphene resonators," *Physical Review B - Condensed Matter and Materials Physics*, vol. 86, no. 23, 2012.

[71] V. Singh, O. Shevchuk, Y. M. Blanter, and G. A. Steele, "Negative nonlinear damping of a multilayer graphene mechanical resonator," *Physical Review Bysi*, vol. 245407, no. 93, pp. 1–5, 2016.

[72] M. I. Dykman and H. B. Chan, "Strong negative nonlinear friction from induced two-phonon processes in vibrational systems," *Nature Communications*, vol. 9, no. 3241, 2018.

[73] M. Amabili, *Nonlinear Vibrations and Stability of Shells and Plates*. Camebridge University Press, 2008.

[74] S. Timoshenko and S. Woinowsky-Krieger, "Theory of Plates and Shells," 1959.

[75] M. Amabili, "Nonlinear damping in large-amplitude vibrations: modelling and experiments," *Nonlinear Dynamics*, vol. 93, pp. 5–18, 2017.

[76] M. Amabili, "Nonlinear vibrations of viscoelastic rectangular plates," *Journal of Sound and Vibration*, vol. 362, pp. 142–156, 2016.

[77] P. Balasubramanian, G. Ferrari, M. Amabili, and Z. J. N. del Prado, "Experimental and theoretical study on large amplitude vibrations of clamped rubber plates," *International Journal of Non-Linear Mechanics*, vol. 94, no. August 2016, pp. 36–45, 2017.

[78] D. Davidovikj, J. J. Slim, S. J. Cartamil-bueno, H. S. J. V. D. Zant, P. G. Steeneken, and W. J. Venstra, "Visualizing the motion of graphene nanodrums," *Nano Letters*, vol. 16, pp. 2768–2773, 2016.

[79] J. Delannoy, *Parametric identification of geometric non-linearities within mechanical systems*. PhD thesis, McGill University, 2016.

[80] M. Amabili, F. Alijani, and J. Delannoy, "Damping for large-amplitude vibrations of plates and curves panels, part 1: Modeling and experiments," *International Journal of Non-Linear Mechanics*, vol. 85, pp. 23–40, 2016.

[81] M. Amabili, F. Alijani, and J. Delannoy, "Damping for large-amplitude vibrations of plates and curved panels, part 2: Identification and comparisons," *International Journal of Non-Linear Mechanics*, vol. 85, pp. 226–240, 2016.

[82] A. Castellanos-Gomez, V. Singh, H. S. J. V. D. Zant, and G. A. Steele, "Mechanics of freely-suspended ultrathin layered materials," *Annalen der Physik*, vol. 527, no. 1-2, pp. 27–44, 2015.

[83] R. J. Dolleman, S. Houri, A. Chandrashekar, F. Alijani, H. S. J. van der Zant, and P. G. Steeneken, "Opto-thermally excited multimode parametric resonance in graphene membranes," *Scientific Reports*, vol. 8, no. 9366, 2018.

[84] G. Ferrari and M. Amabili, "A Tool to Identify Damping during Large Amplitude Vibrations of Viscoelastic," *Proceedings of the ASME 2017 International Mechanical Engineering Congress and Exposition*, 2018.